UNIVERSITÀ
DEGLI STUDI
DI PADOVA

Sede Amministrativa: Università degli Studi di Padova

Dipartimento di SCIENZE CHIMICHE

CORSO DI DOTTORATO DI RICERCA in Scienze Molecolari

CICLO XXXI

PHOTOPHYSICAL PROCESSES AND MOLECULAR ORDERING IN ORGANIC MATERIALS FOR THIRD GENERATION PHOTOVOLTAICS STUDIED BY EPR SPECTROSCOPY

Coordinatore: Prof. Leonard Prins

Supervisore: Prof. Lorenzo Franco

Dottoranda: Paola Guarracino

ABSTRACT

The world energy consumption is increasing at an average rate of 2.1 % per year, spurred by the economic growth in most of Asian countries, Europe and Canada. The consequent depletion of fossil fuels reservoirs and the reinforced need of environmental sustainability are making the challenge of clean and renewable energy sources one of the most urgent challenges for humankind. Solar power is among the best candidates for the leading role in the energy revolution, being clean, infinite and well distributed over the planet. For this reason, photovoltaic technologies for electricity production are gaining increasing popularity. Although inorganic silicon solar cells dominate the market of photovoltaics, organic and hybrid materials attract considerable interest since their properties like flexibility, light-weight, transparency and low-cost could make the difference in the raising of solar electricity. So far, these materials could not yet outperform conventional silicon, stimulating intensive scientific research on both the development of new materials and the understanding of the photophysical mechanisms governing the photovoltaic behavior of organic/hybrid semiconductors.

In this thesis, a series of new organic and hybrid photoactive materials is studied using Electron Paramagnetic Resonance spectroscopy (EPR). This technique, combined with photoexcitation, allows to unambiguously characterize the photoinduced processes involving the formation of paramagnetic states like radicals and triplet states. As shown in the thesis, EPR can also give useful information about molecular ordering in the materials, which is known to be intimately connected with charge transport properties.

Conjugated polymers are known for their semiconducting properties and their blends with strong electron accepting fullerene derivatives are among the best performing organic photovoltaic systems. Donor-acceptor alternating copolymers have been introduced to enhance the light-harvesting properties of the blends. Compared to homopolymers, they usually display a lower crystallinity of the deposited films. Thus, XRD techniques are often not suitable to investigate their molecular ordering features. We apply EPR to the analysis of molecular orientational order in the films of two polymers representative of this class, showing that a consistent degree of preferential orientation occurs with two common deposition methods.

Fullerene-free materials for polymer solar cells have been recently introduced and overcome some of the drawbacks of fullerene acceptors like the limited absorption and the poor bandgap tunability. In this framework, we study two blends of electron-donor and acceptor polymers to probe their

properties with respect to the common fullerene/donor combination, showing that they avoid charge recombination to triplet states which is an active loss mechanism in fullerene-containing blends. Furthermore, the *all-polymer* films provide a high degree of orientational order and efficient interaction between the donor and acceptor phases that make them promising alternatives to polymer-fullerene blends.

A reduced graphene oxide-triphenylamine covalently-linked nanohybrid is studied as potential photosensitizer for TiO_2 in dye-sensitized solar cells, able to improve the conductivity and the stability of the system. EPR shows that efficient photoinduced electron transfer from the sensitizer to the semiconductor occurs, paving the way to this new class of photosensitizers.

Finally, we investigate the photoactivity of a supramolecular *soft*-material, forming a gel, composed of small self-assembling donor and acceptor molecules. In this case, EPR allows to verify the efficiency of charge transport across the supramolecular structures, suggesting appealing semiconducting properties of the material.

The results of this thesis show the relevance of EPR for unraveling functional and morphological properties of photovoltaic materials and provide a useful characterization of the photophysics of new systems that may be further explored to bring substantial progresses to the field of organic photovoltaics.

ABSTRACT

Il consumo mondiale di energia ha un tasso medio di crescita del 2.1 % all'anno, trainato dalla crescita economica di molti Paesi asiatici, dell'Europa e del Canada. Il conseguente depauperamento delle risorse di combustibili fossili e il più stringente bisogno di proteggere l'ambiente stanno facendo della sfida delle energie rinnovabili una delle più urgenti sfide che l'umanità deve affrontare. L'energia solare è tra i migliori candidati a svolgere il ruolo di punta nella rivoluzione energetica, essendo una fonte di energia pulita, infinita e ben distribuita nel pianeta. Per questo motivo le tecnologie fotovoltaiche per la produzione di energia elettrica stanno acquistando crescente popolarità. Sebbene le celle solari a base di Silicio dominino il mercato del fotovoltaico, materiali organici e ibridi sono fonte di crescente interesse grazie alle loro peculiari proprietà, come la flessibilità, la leggerezza e la trasparenza, il basso costo, che ci si aspetta possano fare la differenza nell'affermazione del fotovoltaico. Fino ad ora questi materiali non hanno superato il rendimento dei materiali convenzionali a base di Silicio, stimolando la ricerca scientifica verso lo sviluppo di nuovi materiali e lo studio dei meccanismi fotofisici che governano il comportamento fotovoltaico dei semiconduttori organici e ibridi.

In questa tesi, una serie di nuovi materiali fotoattivi, organici e ibridi, è stata studiata utilizzando la spettroscopia di Risonanza Paramagnetica Elettronica (EPR). Tale tecnica, combinata con la fotoeccitazione, permette di caratterizzare i processi fotoindotti che portano alla formazione di stati paramagnetici come radicali e stati di tripletto. Come mostrato nella tesi, la tecnica EPR può essere anche utilizzata per ottenere informazioni circa l'ordine molecolare nei materiali, che è noto essere strettamente collegato alle loro proprietà di trasporto di carica.

I polimeri coniugati sono noti per le loro proprietà di semiconduttori e le loro miscele con derivati fullereneci - forti electron-accettori - sono tra i sistemi fotovoltaici organici più efficienti. Copolimeri alternanti composti da unità elettron-accettrici e donatrici sono stati introdotti per aumentare l'efficienza di assorbimento dello spettro solare. Rispetto ai classici omopolimeri, questi mostrano solitamente una minore cristallinità dei film depositati. Pertanto, tecniche diffrattometriche si rivelano spesso inadeguate per caratterizzarne l'ordine molecolare. In questa tesi l'EPR viene utilizzato per analizzare l'ordine orientazionale in due polimeri rappresentativi di questa classe, mostrando che un grado consistente di orientazione preferenziale è presente nei film ottenuti con due diverse tecniche di deposizione.

Materiali *fullerene-free* per le celle solari polimeriche sono stati recentemente introdotti per superare alcuni degli svantaggi degli accettori fullerenici, come il limitato assorbimento della luce solare e la difficoltà nel regolare il bandgap e le proprietà elettroniche. In questo conteso, abbiamo studiato due blend costituiti da polimeri elettron-accettori e donatori al fine di investigarne le proprietà e di compararle a quelle dei convenzionali blend di polimeri donatori con derivati fullerenici, dimostrando che essi eliminano la ricombinazione di cariche a formare stati di tripletto, meccanismo noto come fonte di perdita di efficienza nei materiali contenti fullereni. Inoltre, i film polimerici mostrano un elevato grado di ordine orientazionale e un'efficiente interazione tra le fasi di donatore e di accettore che li rendono promettenti alternative ai blend di polimero e fullerene.

Un nanoibrido composto da grafene ossido ridotto e molecole di trifenilammina legati covalentemente, è stato studiato come potenziale colorante per la titania in celle solari sensibilizzate a colorante, capace di migliorare la conducibilità e la stabilità del sistema. L'EPR ha mostrato che un efficiente trasferimento elettronico fotoindotto avviene tra l'ibrido e il semiconduttore, aprendo la strada all'applicazione di una nuova classe di coloranti.

Infine, la fotoattività di un materiale supramolecolare, un gel composto da piccole molecole di donatore e accettore che autoassemblano, è stata studiata. In questo caso l'EPR ha permesso di verificare un efficiente trasporto di carica attraverso le strutture supramolecolari, suggerendo interessanti proprietà semiconduttive del materiale.

I risultati di questa tesi dimostrano la rilevanza dell'EPR per l'indagine su aspetti funzionali e morfologici di materiali fotovoltaici e forniscono una caratterizzazione della fotofisica di nuovi sistemi che potrebbero essere ulteriormente esplorati per apportare progressi sostanziali nel campo del fotovoltaico organico e ibrido.

Table of Contents

CHAPTER 1. INTRODUCTION

1.1 Outline of the Thesis

This thesis deals with the application of Electron Paramagnetic Resonance (EPR) spectroscopic techniques to the investigation of photophysical processes and morphological features in various photoactive materials for Hybrid and Organic Photovoltaics (HOPV).

Understanding photoinduced processes in these materials is crucial for the improvement of cells performances, and so it goes hand-in-hand with the development of new materials. Morphological characteristics at the molecular level were found to have a pivotal impact on charge-transport stimulating researchers to study the factors allowing to control them.

In this context, EPR stands out as a powerful spectroscopic tool since it is selective for paramagnetic species like radicals and triplet states that are formed upon photoexcitation of the materials, which can be used to shed light on the photovoltaic processes as well as on molecular ordering.

The scope of this thesis is to exploit these potentialities of EPR spectroscopy to investigate a variety of materials and molecular systems, developed in collaboration with other research groups from the University of Padova and other Institutions.

The thesis is organized in six Chapters.

In Chapter 1 a concise introduction to state-of-the-art hybrid and organic photovoltaics will be given, with particular emphasis on polymeric photovoltaic materials and dye-sensitized solar cells.

Chapter 2 will describe the principles of EPR spectroscopy and how it is applied to the study of paramagnetic states generated in photovoltaic materials. Furthermore, in this chapter a description of the main EPR techniques employed in the thesis is provided.

Chapter 3 and Chapter 4 are dedicated to the study of photovoltaic conjugated polymers. In Chapter 3 the principles of molecular-order investigation through EPR will be illustrated and applied to the study of the films of two representative conjugated polymers to gain information on their molecular ordering depending on the film-deposition technique. In Chapter 4 two recently developed *all-polymer* blends will be thoroughly characterized in terms of both their photophysics and their molecular ordering inside the photoactive films.

Chapter 5 will report on a new hybrid photosensitizer for TiO_2, composed of small triphenylamine molecules grafted on a graphenic substrate, to be employed in dye-sensitized solar cells. The Chapter explores the photophysics of the system either alone or adsorbed on the TiO_2 semiconductor.

Chapter 6 will introduce a donor-acceptor charge-transfer self-assembled gel for potential application in photovoltaic devices. EPR was used here to probe the photoactivity of the system and the charge-transport properties related to the supramolecular self-assembling of donor and acceptor molecules.

1.2 Organic and Hybrid Photovoltaics

Solar energy reaching Earth's surface was estimated to be close to 90 PW[1], an enormous amount, largely exceeding the total mankind energy consumption (17 TW). These data make solar power extremely appealing to fulfil the world's energy demand and to replace currently unsustainable energy sources, that will be completely exhausted in the next future (50 years were estimated for oil and natural gas, and about 100 years for coal)[2]. On the contrary, solar energy is fully renewable, considering that the life of sun will continue for the next 4 billions of years.

Nowadays about 2% of the world's electricity demand is covered by photovoltaics (PV)[3], with a large predominance of the so-called *first-generation* PV technology, developed in the early 1950s and based on either single-crystal or polycrystalline doped Silicon wafers. This technology still holds the record in Power Conversion Efficiency (PCE), exceeding 20 % PCE in commercial modules[4], and long-term stability. However, the high production costs related to the onerous processing of materials involving crystallization, purification and doping, lead to the development of *second-generation* or *thin-film* technologies starting from the 1970s, based on materials like amorphous Silicon, GaAs, CdTe, CIGS (Copper Indium Gallium Selenide), that reduced the production costs by decreasing the amount of material, but still have not matched 1st-generation PCEs and also suffer by toxicity issues.

In this context, *third-generation* PV approaches were introduced since the 1990s, with the aim of exploiting the concept of thin-film technologies but with a new class of materials, with large availability and low toxicity, namely organic and hybrid organic-inorganic materials[5]. Besides the low cost of raw materials, peculiar characteristics of Hybrid-Organic photovoltaic systems (HOPV) are the light-weight and flexibility of the modules, that pave the way to new applications such as 'wearable' photovoltaics, windows, buildings facades[6]. More importantly, these materials allow for low-cost solution-based processing like *roll-to-roll* printing techniques, that represent cost-effective large-scale fabrication methods[7,8]. Despite these promising features, HOPV materials suffer from fundamental drawbacks like limited PCEs and poor stability compared to 1st-generation PV. For these reasons, HOPV is still at a research level and considerable research efforts are focused on the investigation of the loss-mechanisms and the factors affecting device performances.

The field of Hybrid-Organic Photovoltaics encompasses a variety of materials and device architectures that were developed in the past three decades.

Purely organic photoactive materials are employed in the so-called *Small-Molecule solar cells*[9,10], based on the interaction between donor and acceptor aromatic molecules, that have recently reached performances close to 9% power conversion efficiency (PCE). These solar cells are strictly related, both in terms of chemical composition and working principles, to another kind of purely-organic photovoltaic cells, namely *Polymer solar cells*, in which the donor material is typically a conjugated polymer used in blends with fullerene derivatives as electron acceptors. Polymer solar cells are more popular compared to small-molecule counterparts since they have shown higher PCEs, at present approaching 14%[11].

Besides small-molecule and polymer PV, a new idea for OPV recently began to be explored, stemming from the concept of *supramolecular* electronics[12] and aiming at the exploitation of the self-assembling of small-molecular donors and acceptors in supramolecular structures to drive charge generation and transport[13]. Up to now, only few examples of cells made of organic supramolecular materials exist in literature, however, the ease of preparation of these materials is encouraging the study of their photophysical properties, with a view to possible future applications in the field of photovoltaics.

Hybrid photovoltaic materials include those employed in *dye-sensitized solar cells* (DSSCs) and *perovskite* solar cells. The photoactive material in DSSCs is composed of a nanoporous TiO_2 layer on which small organic chromophores are adsorbed, enabling the sensitization of the inorganic semiconductor towards visible-light harvesting and the photogeneration of charges thanks to electron-injection from the excited state dyes to the conduction band of the solid. A variety of photosensitizers has been employed in DSSCs and lately a porphyrin-based chromophore outperformed previously used dyes, leading to 13% PCE[14].

Perovskite solar cells are based on hybrid organic-inorganic perovskites, the main representative being methylammonium lead iodide. These materials had an abrupt growth in performance, beginning with a modest 4% PCE in 2009 and exceeding 20% in 2017[15]. At present, they amply surpassed the other HOPV technologies, however they are still affected by stability issues[16].

The materials investigated in this thesis were developed for the application in polymer and dye-sensitized solar cells and will be described in the respective Chapters (Chapter 3 and 4 deal with polymeric materials while Chapter 5 deals with a new photosensitizer for DSSCs). Furthermore, we examined a supramolecular *soft-material* for possible photovoltaic applications (Chapter 6). The aim of the thesis is to shed light on the photophysical processes occurring in the analyzed systems, and on molecular ordering occurring in the polymeric films, which can be determinant for their performance.

After a brief description of the most important figure of merits of photovoltaic devices (section 1.3), the rest of this Chapter will be dedicated to a more detailed introduction to polymer photovoltaics (section 1.4) and DSSCs (section 1.5).

1.3 Solar cells electrical characteristics and figure of merits

Photovoltaic cells are photodiodes, that generate an electric current upon illumination.

In the dark, the cell does not produce any current unless a large forward bias is applied to the electrodes, and the current-voltage (J-V) relationship is described by:

$$J_{dark} = J_0\left(e^{qV/kT} - 1\right) \qquad \text{Eq. 1.1}$$

where q is the elementary charge, V is the applied bias voltage, k is the Boltzmann constant, T is temperature and J_0 is the so-called *saturation* current density, a very small current produced in reverse bias conditions.

Under illumination, a photogenerated current flows in the opposite direction compared to the injected current and the cell can generate electric power. The overall current density through the device is maximum when no voltage is applied i.e. under short-circuit conditions, in which the current (J_{SC}) corresponds to the photogenerated current. The current-voltage curve of a solar cell under illumination can be described to a first approximation by Eq. 1.2:

$$J_{light} = J_0\left(e^{qV/kT} - 1\right) - J_{SC} \qquad \text{Eq. 1.2}$$

For a sufficiently large applied forward bias, the photocurrent is cancelled by the injected current and the current density through the device is zero (open-circuit conditions). The voltage that must be applied to reach such a condition is called open-circuit voltage (V_{OC}).

The short-circuit current and the open-circuit voltage of a solar cell determine the ideal maximum power of the cell ($P_{ideal} = J_{SC} \cdot V_{OC}$) and therefore they should be maximized to improve the cell performance. The *fill-factor* is a measure of the ability of the cell to approach the ideal electric power and it is defined by Eq. 1.3:

$$FF = \frac{J_{MP} \cdot V_{MP}}{J_{SC} \cdot V_{OC}} \qquad \text{Eq. 1.3}$$

where J_{MP} and V_{MP} are the current and voltage corresponding to the maximum power that the solar cell can generate (see Figure 1.1).

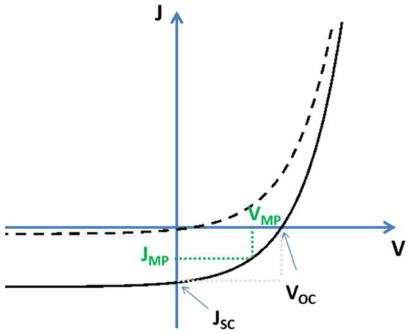

Figure 1.1 Current-Voltage curves for a solar cell in dark (dashed line) and under illumination (plain line).

The most important figure of merit of a photovoltaic cell is its *power conversion efficiency* (PCE), defined as the ratio between the maximum electrical power generated by the cell ($P_{max} = J_{MP} \cdot V_{MP}$) and the incident optical power (P_{inc}):

$$PCE\ (\%) = \frac{P_{max}}{P_{inc}} \cdot 100 = FF \cdot \frac{J_{SC} \cdot V_{OC}}{P_{inc}} \qquad \text{Eq. 1.4}$$

To quantify the efficiency of light conversion at different wavelengths of the solar spectrum the *external* and *internal quantum efficiencies* (*EQE* and *IQE* respectively) are used. EQE is defined as the ratio between the number of collected charges at the electrodes and the number of incident photons at a given wavelength, thus it depends not only on the efficiency of charge generation and separation inside the cell but also on the absorption coefficient of the photoactive material. The latter dependency is removed in the IQE figure of merit, since it represents the ratio between the number of collected charges and the number of absorbed photons.

1.4 Polymer solar cells

The electrical conductivity of conjugated polymers was discovered by Heeger and coworkers in 1977, who studied this property on polyacetylene and were awarded the Nobel Prize in chemistry in 2000[17]. Since then, polymer photovoltaics was soon envisaged as one of the possible applications of the discovery, and the scientific interest in the field was boosted in 1995 by the invention of the first *Bulk-Heterojunction Solar Cell* (BHJSC), where the semiconducting polymer MEH-PPV (poly-metoxy-ethylhexyloxy *p*-phenylenevinylene) was blended with fullerene (C_{60}), leading to a 2.9% PCE[18]. The key features of this first BHJSC, that boosted the photovoltaic performance of polymeric materials, were essentially two: the presence of a strong electron-acceptor like fullerene, and the macroscopic morphology of the photoactive layer.

Interfacing the polymer with an electron-acceptor is a successful strategy since it allows to overcome the Coulombic attraction in the electron-hole pair generated from exciton dissociation in the photoexcited polymer, thanks to the energy gain associated with the photoinduced electron-transfer to a high electron-affinity material.

The morphology of the *bulk-heterojunction* consists in a finely interpenetrating network of the donor and acceptor materials, that builds up internal donor-acceptor heterojunctions, which enable maximization of the interface and consequent enhancement of charge photogeneration upon photoinduced electron-transfer between the two components. Therefore, this architecture replaced the previous bilayer arrangement (see Figure 1.2) and became an essential characteristic of polymeric photoactive layers.

Figure 1.2 Schematic representation of the *bilayer* and *BHJ* architectures for polymer solar cells.

1.4.1 Photoactive layer materials

The benchmark polymer for BHJSCs is the regioregular poly(3-hexylthiophene) (P3HT). It has been used in photovoltaic devices since 2002, when Brabec and coworkers showed that it could provide a 2.8% PCE in a device where it was blended with the PCBM ([6,6]-phenyl-C_{61}-butyric acid methyl ester) fullerene derivative[19]. Since then, the P3HT/PCBM couple gained an enormous popularity in OPV research and it is still the most widely investigated system for BHJSCs[20]. Over the years, P3HT solar cells could reach efficiencies exceeding 5% by increasing the regioregularity of the polymer and by tuning the active layer morphology through post-treatments like thermal annealing[21,22].

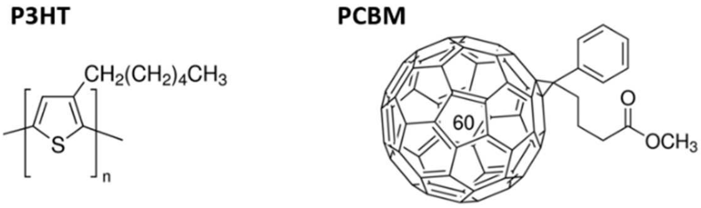

Figure 1.3 P3HT and PCBM structures

Despite the limited PCE that can be achieved by the use of P3HT/PCBM, it is still taken as the model material in BHJSCs studies, which helps to explore the device physics as well as structure-property relationships and device engineering strategies[23].

The bandgap of P3HT, being ~1.9 eV, limits its light-absorption below 650 nm, which of course reduces the performance of the material. Therefore, to extend the spectral range of sun irradiation exploitable by the photoactive layer, a new class of conductive polymers was introduced since the early 2000s[24], characterized by a reduced bandgap and therefore known as 'low-bandgap semiconducting polymers'. The strategy to achieve reduced bandgaps relies on the alternation of building blocks with electron-donating and electron-accepting character, thus forming donor-acceptor copolymers, often named as *push-pull* copolymers. A unique feature of these polymers is that their HOMO and LUMO orbitals are largely dominated by the HOMO and LUMO orbitals of the donor (D) and the acceptor (A) moieties, respectively. Hence, the energy levels of the polymers can be easily tuned by modifying the building blocks separately. Furthermore, the intramolecular charge transfer (push-pull effect) associated to the alternation of D and A units is expected to favor the photoinduced electron transfer from the polymer to the fullerene acceptor.

In Figure 1.4 some of the representative building blocks employed in low-bandgap polymers are shown.

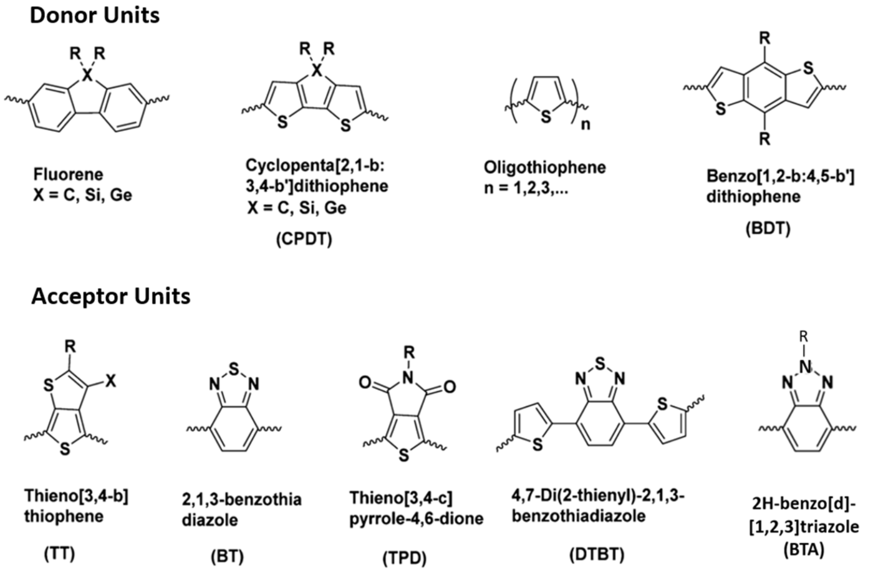

Figure 1.4 Donor and acceptor building blocks for low-bandgap copolymers.

At present, a large variety of copolymers has been synthesized using the building units reported in Figure 1.4 and many others. On this kind of polymeric materials, there are several comprehensive reviews with a systematic account of their performances[25,26]. It can be pointed out that the best-performing polymers achieved efficiencies close to 11% in blends with PCBM, while very recently a record PCE of 14% was reported for a 'ternary' BHJSC, in which a non-fullerene acceptor was added to the polymer/fullerene blend[11].

Fullerene derivatives have been the undisputed electron acceptors in polymer solar cells for two decades, combining the properties of fullerenes with the good solubility ensured by the attached functional groups. In particular, $PC_{61}BM$ (or simply PCBM) and $PC_{71}BM$ ([6,6]-phenyl-C_{71}-butyric acid methyl ester) dominated as they offered outstanding performances compared to other derivatives. Both of them display a broad absorption of visible light with an intense band in the near-UV region. Compared to $PC_{61}BM$, the $PC_{71}BM$ derivative was often found to give better solar cell performances, which was attributed to the higher extinction coefficient in the 400 nm – 600 nm region.
The unique feature of fullerenes is their fully-conjugated structure which determines the strong electron-accepting character and electron-transport capabilities, besides facilitating electron-delocalization at the D/A interface. However, in the past few years a new line of research gained increasing attention, focusing on the possibility to replace fullerenes with other molecular acceptors, capable of extending the optical absorption range of the acceptor component and enabling for easy and broad tunability of energy levels, which is a difficult task with fullerenes. Although the initially designed molecules could not outperform PCBM, very recently some small molecular acceptors based on fused heterocycles were developed that could exceed the PCEs of the best performing fullerene-based BHJSCs[27,28]. These results are expected to trigger an unprecedented interest in the field of non-fullerene acceptors in the next future, that will allow to establish if these new acceptors are going to become the new fullerenes.

1.4.2 Photophysics

In this section the main processes occurring in the active layer of a polymer/fullerene solar cell will be briefly summarized. The following description can actually be extended to organic donor-acceptor (D-A) blends in general.

Upon illumination of the material, both the donor and the acceptor domains can absorb photons generating excitons. In organic semiconductors, an exciton can be described as a molecular excitation or a strongly bound electron-hole pair. In a molecular description of the materials, it coincides with the molecule excited state and it has singlet character since direct excitation of a triplet state is spin-forbidden. In the ps-time domain after photon absorption, the so-called *hot excitons*, i.e. upper excited states, relax to the lowest excited state by internal conversion. These relaxed excitons can then undergo a variety of processes.

The desired process for generation of a photovoltaic effect is exciton dissociation i.e. photoinduced electron-transfer (ET). This can occur if the exciton reaches the interface between the D and A domains, where the driving force for electron transfer is given by the electron affinity of the acceptor material, that should exceed the exciton binding energy. Electron transfer can occur from both donor and acceptor-localized excitons. In a simplified molecular orbital description, a donor molecule in the excited state (described as a molecular state with half occupied HOMO and LUMO) can transfer an electron from its LUMO to the LUMO of the acceptor. On the other hand, excited state acceptor molecules can accept an electron in their half-occupied HOMO from the HOMO of the donor, provided that this one is higher in energy. Electron transfer involving excited acceptor molecules is also referred to as *hole transfer* since a hole is transferred between the HOMOs of the excited acceptor and that of the ground-state donor.

Excitons can reach the D/A interface if the distance they must diffuse across is below their diffusion length, defined as the distance over which the exciton can diffuse before decaying. The typical exciton diffusion length in organic semiconductors is about 10 nm, which explains the necessity of a finely mixed network of donor and acceptor phases as provided by the bulk-heterojunction architecture. Unfortunately, part of the excitons generated upon light-absorption decay before reaching the interface. The decay processes encompass non-radiative decay and fluorescence emission, but also include Intersystem Crossing to the lower-laying excited triplet state, driven by spin-orbit coupling. The fate of the triplet state depends on its energy. Indeed, if it is close to the D/A interface and if the energy matching with the D or A counterpart is still favorable, it can undergo electron transfer, otherwise it decays either radiatively (phosphorescence) or non-radiatively to the singlet ground state. The exciton decay mechanisms are summarized in the Jablonski diagram reported in Figure 1.5.

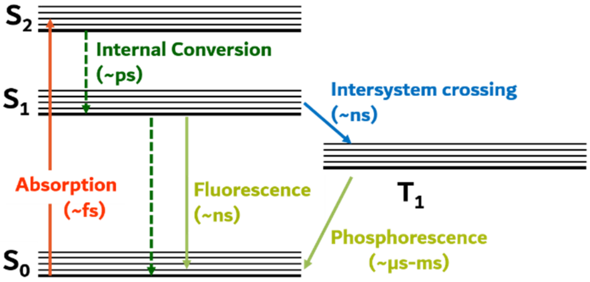

Figure 1.5 Jablonski diagram showing the fate of the excitation in domains where exciton dissociation does not occur.

When an exciton undergoes electron transfer, a so-called *charge-transfer state* (CT) is formed, in which the electron and the hole form a Coulombically-bound pair (an electron-hole pair or radical-pair if a molecular description is adopted, with a radical anion formed on the acceptor, $A^{\cdot -}$, and a radical cation on the donor, $D^{\cdot +}$). A CT state can also be referred to as a *Spin-Correlated Radical Pair* (SCRP), since the small distance between the two unpaired spins in the radical pair enables weak coupling by means of the dipolar and exchange interactions[29]. The spin-state of the SCRP reflects the spin-multiplicity of the precursor exciton. Therefore, they are usually generated as singlet SCRP. These radical pairs can successfully dissociate and turn into non-interacting radicals, also referred to as *charge-separated states* (CS), or they can recombine through back-electron transfer, which restores the neutral ground state of the donor and acceptor molecules (*geminate* recombination). Singlet-state SCRPs can also convert to the triplet state[30] from which recombination to the ground-state is spin-forbidden and therefore slower. However, triplet-state radical pairs can recombine and form the triplet state of the neutral molecules, provided that an energy gain exists, namely that the triplet state is more stable compared to the CT state. Charge-recombination forming triplet states is therefore a loss-mechanism in photovoltaic materials, since the energy-matching requirements for this process imply that the resulting triplet exciton is not able to spontaneously dissociate.

The free charges generated upon dissociation of CT states can diffuse through the material *via* a hopping mechanism and eventually reach the electrodes of the device, or they can recombine upon random encounter between opposite charges (*non-geminate* recombination). To reduce the impact of recombination and facilitate the charge collection at the electrodes, thin films of photoactive material are employed (~100 nm), as they were shown to provide the best trade-off between light-absorption and charge-recombination.

A summary of the photophysical processes is depicted in Figure 1.6.

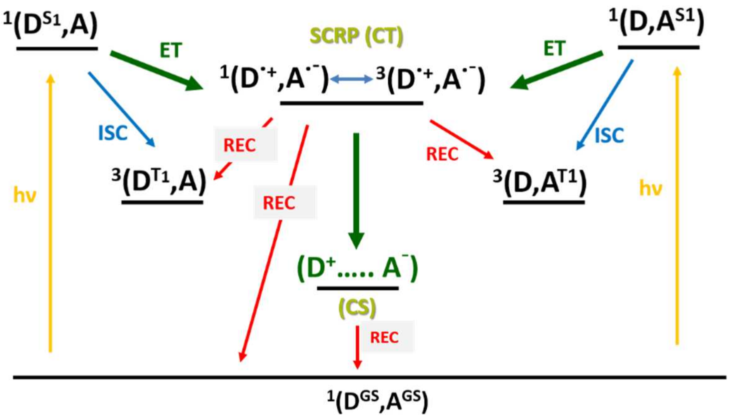

Figure 1.6 Energy diagram illustrating the photoinduced processes in a D-A blend where exciton dissociation takes place. GS: ground state, S1: first excited singlet state; T1: first excited triplet state; ET: electron transfer. ISC: Intersystem Crossing. REC: recombination. The superscripts *1* and *3* indicate the spin-multiplicity of the state.

Electron Paramagnetic Resonance is a powerful tool for the investigation of photophysics in organic D-A materials as it provides specific spectroscopic signatures for each one of the paramagnetic states that were described above. Therefore, it allows to easily distinguish between CT and CS states and between triplet states formed by Intersystem crossing (ISC) or charge-recombination, as will be made clear in the next Chapter.

1.5 Dye-sensitized solar cells

The concept of dye-sensitization of inorganic semiconductors to produce a photovoltaic effect was known since the 1980s[31]. However, the first breakthrough dye-sensitized solar cell was developed in 1991 by Grätzel and coworkers[32] who could improve the performance by nearly an order of magnitude, reaching a 7.9% PCE, by maximization of the TiO_2 semiconductor surface, thanks to the use of a nanoporous TiO_2 powder. Since then, DSSCs (also commonly named *Grätzel cells*) soon attracted considerable scientific interest. They introduced the new concept of separating light-absorption from charge transport, which allows to optimize each process separately. Furthermore, DSSCs demonstrated high performances under diffuse light, which made them good candidates for indoor applications. On the economic side, the use of an abundant and inexpensive material like TiO_2 made them even more attractive.

Schemes of both the structure and the working principles of a DSSC are reported in Figure 1.7 and are illustrated in the following.

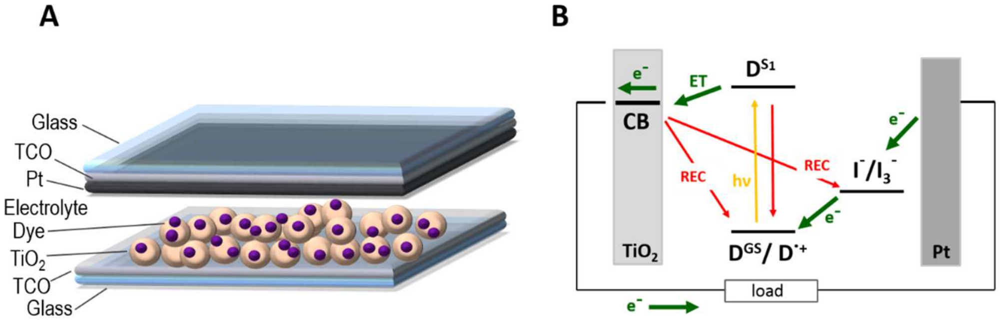

Figure 1.7 Representation of the architecture of a DSSC (A) and its working principles (B).

The photoactive layer is composed of a nanoporous TiO_2 layer (with particles diameter between 10 and 30 nm) and a monolayer of small dye molecules, adsorbed on the inorganic semiconductor. The TiO_2 nanopowder is deposited on a glass or PET substrate covered with a transparent conductive oxide (TCO), generally fluorine-doped tin oxide (FTO), and then sintered to establish electronic conduction. This FTO-TiO_2-dye electrode represents the photoanode of the cell, while the counter-electrode is composed of a thin Pt layer deposited on a conducting glass or PET substrate (covered with FTO). The space between the two electrodes is filled with a solution of a redox mediator, which historically is the I_3^-/I^- couple.

The photovoltaic effect in the DSSC cell is initiated by light-absorption by the dye molecules, which results in the injection of electrons into the conduction band (CB) of the oxide, if the appropriate energy requirements are satisfied, i.e. if the dye excited state has higher energy compared to the semiconductor CB. The semiconductor provides electron transport towards the FTO electrode, while the redox mediator ensures the regeneration of the dye neutral ground state, which is essential for repeated cell-functioning cycles. The oxidized mediator molecules are then reduced at the counter-electrode. Besides these desired pathways, the loss mechanisms must be indicated, the first one being the dye excited state decay through fluorescence and non-radiative mechanisms, which compete with electron transfer to the semiconductor. After electron-injection, back-electron transfer can occur between the injected electrons and the oxidized dye or mediator molecules. Furthermore, the oxidized mediator molecules can extract electrons from the FTO electrode if they come in contact. For this reason, a compact layer of TiO_2 is usually deposited on the FTO and underlays the mesoporous TiO_2 layer, in order to block the mediator molecules. To limit also the contact between the redox mediator and TiO_2, and therefore reduce electron transfer from the semiconductor, sterically hindered dyes are usually employed. Finally, efficiency of dye-regeneration is one of the reasons underpinning the necessity of a mono-molecular layer of adsorbed dye molecules, since molecular aggregates hamper the regeneration of the first-layer molecules, leading to very poor cell performances.

1.5.1 Photoactive layer materials

Since the breakthrough of dye-sensitized solar cells in 1991, great research efforts were devoted to the optimization of DSSCs components, with a particular interest for the sensitizer and the redox mediator.

The first successful sensitizers were the Ru(II)-polypyridyl complexes developed in Grätzel group, known as N3, N719 and N749, also called 'black dye' (Figure 1.8) that could achieve up to 11% PCEs. The success of these dyes was partly due to the broad optical absorption, approaching the near-IR (NIR) range. However, their high costs due to the use of a noble metal like Ru and the relatively low absorption coefficients prompted the scientific community to study alternative dyes.

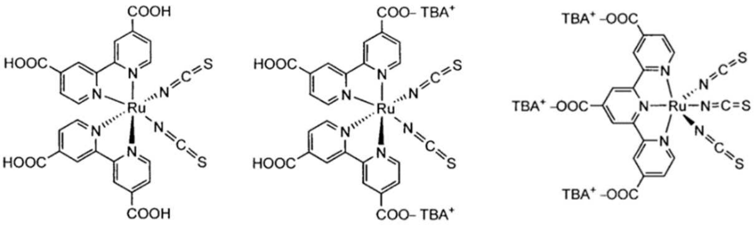

N3 PCE = 11.03 %

N719 PCE = 11.18 %

Black dye PCE = 11.1 %

Figure 1.8 Structures of the benchmark ruthenium-based dyes.

Porphyrins and phthalocyanines were identified as promising candidates, with the advantage of providing intense absorption bands in the NIR region and a high photochemical stability. Recently, a porphyrin-based dye functionalized with donor and acceptor groups, according to a donor-π-acceptor architecture (see below), provided over 13% PCE, outperforming Ru complexes[14].

Metal-free dyes were introduced in the early 2000s. Their appealing features include high molar extinction coefficients, easily tunable electronic properties and lower costs compared to the Ru-based dyes. Various kinds of organic dyes were investigated including coumarins, indolines and oligothiophenes[31,33]. However, these never gave outstanding results in photovoltaic devices. The major improvements in the field of organic sensitizers were introduced by triarylamine-based dyes (TPAs), that could provide excellent performances, attributed to their strong electron-donating character and good hole-transport. TPA-based dyes recently reached efficiency values comparable to the benchmark Ru-complexes[34]. The general architecture for organic dyes consists in the so-called D-π-A architecture (Figure 1.9), which was shown to increase conjugation and broaden the optical absorption of the dyes.

Furthermore, since the HOMO and the LUMO are mainly localized on the D and A moieties respectively, it implies a partial intramolecular charge transfer associated to the optical transition, which is beneficial for photoinduced electron transfer to TiO_2.

The best-performing anchoring group is carboxylic acid, which is in general incorporated in the A moiety of the D-π-A structure by the use of the cyanoacrylate group (an electron acceptor).

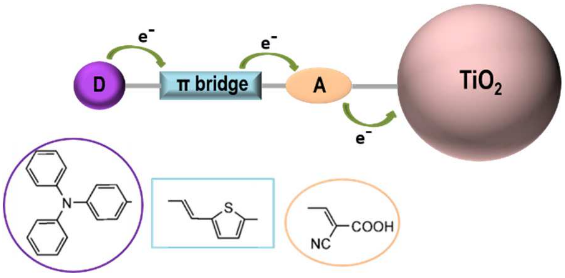

Figure 1.9 Scheme of the D-π-A architecture for organic dyes, with examples of donor, π bridge and acceptor moieties.

The common redox couple in DSSCs is I_3^-/I^-, which yields the best efficiencies thanks to the suitable redox potential, the slow recombination rate between electrons in TiO_2 and I_3^- and the rapid dye-regeneration[35]. However, its corrosive properties encouraged the investigation of new redox mediators. An alternative to I_3^-/I^- is the Co^{3+}/Co^{2+} couple, in the form of Co(II/III)-tris(bipyridine) compounds, although it was found to have a much slower diffusion constant through the TiO_2 pores.

Solid hole conductors (or hole-transport materials, HTM) were also investigated in order to replace liquid electrolytes, enabling the development of solid-state DSSCs (*ss*-DSSCs) which offer the advantage of avoiding electrolyte leakage. The best-performing organic hole-conductor is the triarylamine-based *spiro-MeOTAD* (2,2',7,7'-tetrakis(*N,N*-di-*p*-methoxyphenyl-amine)9,9'-spirobifluorene). At present, HTMs could not yet outperform liquid electrolytes, the main limitations to their performances being the enhanced recombination and reduced TiO_2-pores filling.

1.5.2 Photophysics

The main photoinduced processes occurring in the active layer of DSSCs were introduced during the description of the working principles of the cell (Figure 1.7B) and will be considered here in more detail.

The fate of the excitation on the donor dye molecules is determined by the processes already described for the excited state molecules in donor-acceptor blends in section 1.4.2 (Figure 1.5). These deactivating processes compete with photoinduced electron transfer to the TiO_2 semiconductor CB. As in donor-acceptor blends, the role of the triplet state of the dye, formed upon ISC from the excited singlet state, depends on the energy matching with the acceptor (TiO_2 CB in this case). Indeed, electron injection from triplet state dye molecules is possible if the triplet state lays higher in energy compared to the CB states of the oxide, and it was observed in the case of Ru-based and phthalocyanine dyes[36,37]. If this energetic condition is fulfilled, conversion to the triplet state offers the advantage of a longer excited state lifetime compared to the singlet state, due to the spin-forbidden transition to the ground state.

The overall electron-injection efficiency depends on the balance between the kinetics of injection, excited-state decay and also back-electron transfer from the semiconductor. In efficient DSSCs electron injection was shown to occur in the fs/ps timescale, while recombination takes milliseconds[36]. Charge transport in nanoporous TiO_2 is believed to occur via a hopping mechanism across the numerous nanocrystals that form the semiconductor. The most widely accepted model is the multiple trapping model[38], according to which electrons are mostly trapped into localized states below the conduction band, from which transport occurs by thermal activation.

1.6 References

(1) Armaroli, N.; Balzani, V. Solar Electricity and Solar Fuels: Status and Perspectives in the Context of the Energy Transition. *Chem. - A Eur. J.* **2015**, *22*, 32–57.

(2) Petroleum, B. *British Petroleum, BP Statistical Review of World Energy 2017, Http://www.bp.com*.

(3) *REN21-Renewable Energy Policy Network for the 21st Century, Renewables Global Status Report 2018, http://www.ren21.net*.

(4) Green, M. a.; Hishikawa, Y.; Dunlop, E. D.; Levi, D. H.; Hohl-Ebinger, J.; Ho-Baillie, A. W. Y. Solar Cell Efficiency Tables (version 52). *Prog. Photovoltaics Res. Appl.* **2018**, *26*, 427–436.

(5) Brabec, C.; Dyakonov, V.; Scherf, U. *Organic Photovoltaics: Materials, Device Physics and Manufaturing Technology*; Brabec, C., Dyakonov, V., Scherf, U., Eds.; Wiley, VCH, 2008.

(6) Cornaro, C.; Di Carlo, A. Organic Photovoltaics for Energy Efficiency in Buildings. In *Nano and Biotech Based Materials for Energy Building Efficiency*; Pacheco Torgal, F., Buratti, C., Kalaiselvam, S., Granqvist, C. G., Ivanov, V., Eds.; Springer, 2016; pp 1–496.

(7) Krebs, F. C.; Søndergaard, R. R.; Markus, H. Roll-to-Roll Fabrication of Large Area Functional Organic Materials. *J. Polym. Sci. Part B Polym. Phys.* **2013**, *51*, 16–34.

(8) Krebs, F. C. Fabrication and Processing of Polymer Solar Cells: A Review of Printing and Coating Techniques. *Sol. Energy Mater. Sol. Cells* **2009**, *93*, 394–412.

(9) Zhang, Q.; Kan, B.; Liu, F.; Long, G.; Wan, X.; Chen, X.; Zuo, Y.; Ni, W.; Zhang, H.; Li, M.; et al. Small-Molecule Solar Cells with Efficiency over 9%. *Nat. Photonics* **2014**, *9*, 35–41.

(10) Moench, T.; Koerner, C.; Murawski, C.; Murawski, J.; Nikolis, V. C.; Vandewal, K.; Leo, K. Small Molecule Solar Cells. In *Molecular Devices for Solar energy Conversion and Storage*; Tian, H., Boschloo, G., Hagfeldt, A., Eds.; Springer: Singapore, 2018; pp 1–43.

(11) Xiao, Z.; Jia, X.; Ding, L. Ternary Organic Solar Cells Offer 14% Power Conversion Efficiency. *Sci. Bull.* **2017**, *62* (23), 1562–1564.

(12) Schenning, A. P. H. J.; Meijer, E. W. Supramolecular Electronics□; Nanowires from Self-Assembled P -Conjugated Systems. *Chem. Commun.* **2005**, *0*, 3245–3258.

(13) Babu, S. S.; Prasanthkumar, S.; Ajayaghosh, A. Self-Assembled Gelators for Organic Electronics. *Angew. Chemie Int. Ed.* **2012**, *51*, 1766–1776.

(14) Mathew, S.; Yella, A.; Gao, P.; Humphry-Baker, R.; Curchod, B. F. E.; Ashari-Astani, N.; Tavernelli, I.; Rothlisberger, U.; Nazeeruddin, M. K.; Grätzel, M. Dye-Sensitized Solar Cells with 13% Efficiency Achieved through the Molecular Engineering of Porphyrin Sensitizers. *Nat. Chem.* **2014**, *6*, 242–247.

(15) Arora, N.; Dar, M. I.; Hinderhofer, A.; Pellet, N.; Schreiber, F.; Zakeeruddin, S. M.; Grätzel, M. Perovskite Solar Cells with CuSCN Hole Extraction Layers Yield Stabilized Efficiencies Greater than 20%. *Science* **2017**, *358*, 768–771.

(16) Correa-Baena, J.-P.; Abate, A.; Saliba, M.; Tress, W.; Jesper Jacobsson, T.; Grätzel, M.; Hagfeldt, A. The Rapid Evolution of Highly Efficient Perovskite Solar Cells. *Energy Environ. Sci.* **2017**, *10* (3), 710–727.

(17) Hideki, S.; Louis, J.; Macdiarmid, A. G.; Chwan, K. C.; Heeger, A. J. Synthesis of Electrically Conducting Organic Polymers: Halogen Derivatives of Polyacetylene. *J.C.S. Chem. Comm.* **1977**, 578–580.

(18) Yu, G.; Gao, J.; Hummelen, J. C.; Wudl, F.; Heeger, A. J. Polymer Photovoltaic Cells□: Enhanced Efficiencies via a Network of Internal Donor-Acceptor Heterojunctions. *Science* **1995**, *270*, 1789–1791.

(19) Schilinsky, P.; Waldauf, C.; Brabec, C. J. Recombination and Loss Analysis in Polythiophene Based Bulk Heterojunction Photodetectors. *Appl. Phys. Lett.* **2002**, *81*, 3885–3887.

(20) Dang, M. T.; Hirsch, L.; Wantz, G. P3HT:PCBM , Best Seller in Polymer Photovoltaic Research. *Adv. Mater.* **2011**, *23*, 3597–3602.

(21) Kim, Y.; Cook, S.; Tuladhar, S. M.; Choulis, S. a.; Nelson, J.; Durrant, J. R.; Bradley, D. D. C.; Giles, M.; McCulloch, I.; Ha, C.-S.; et al. A Strong Regioregularity Effect in Self-Organizing Conjugated Polymer Films and High-Efficiency Polythiophene:fullerene Solar Cells. *Nat. Mater.* **2006**, *5*, 197–203.

(22) Zhao, G. J.; He, Y. J.; Li, Y. 6.5% Efficiency of Polymer Solar Cells Based on poly(3-Hexylthiophene) and Indene-C60 Bisadduct by Device Optimization. *Adv. Mater.* **2010**, *22*, 4355–4358.

(23) Dang, M. T.; Hirsch, L.; Wantz, G.; Wuest, J. D. Controlling the Morphology and Performance of Bulk Heterojunctions in Solar Cells. Lessons Learned from the Benchmark poly(3-hexylthiophene):[6,6]-Phenyl- C61-Butyric Acid Methyl Ester System. *Chem. Rev.* **2013**, *113*, 3734–3765.

(24) Winder, C.; Sariciftci, N. S. Low Bandgap Polymers for Photon Harvesting in Bulk Heterojunction Solar Cells. *J. Mater. Chem.* **2004**, *14*, 1077.

(25) Lu, L.; Zheng, T.; Wu, Q.; Schneider, A. M.; Zhao, D.; Yu, L. Recent Advances in Bulk Heterojunction Polymer Solar Cells. *Chem. Rev.* **2015**, *115*, 12666–12731.

(26) Liu, C.; Wang, K.; Heeger, A. J. Low Bandgap Semiconducting Polymers for Polymeric Photovoltaics. *Chem. Soc. Rev.* **2016**, *45*, 4825–4846.

(27) Hou, J.; Inganäs, O.; Friend, R. H.; Gao, F. Organic Solar Cells Based on Non-Fullerene Acceptors. *Nat. Mater.* **2018**, *17*, 119–128.

(28) Chen, W.; Zhang, Q. Recent Progress in Non-Fullerene Small Molecule Acceptors in Organic Solar Cells (OSCs). *J. Mater. Chem. C* **2017**, *5*, 1275–1302.

(29) Behrends, J.; Sperlich, A.; Schnegg, A.; Biskup, T.; Teutloff, C.; Lips, K.; Dyakonov, V.; Bittl, R. Direct Detection of Photoinduced Charge Transfer Complexes in Polymer Fullerene Blends. *Phys. Rev. B* **2012**, *85*, 125206.

(30) Niklas, J.; Beaupré, S.; Leclerc, M.; Xu, T.; Yu, L.; Sperlich, A.; Dyakonov, V.; Poluektov, O. G. Photoinduced Dynamics of Charge Separation: From Photosynthesis to Polymer–Fullerene Bulk Heterojunctions. *J. Phys. Chem. B* **2015**, *119*, 7407–7416.

(31) Hagfeldt, A.; Boschloo, G.; Sun, L.; Kloo, L.; Pettersson, H. Dye-Sensitized Solar Cells. *Chem. Rev.* **2010**, *110*, 6595–6663.

(32) O'Regan, B.; Gratzel, M. A Low-Cost, High-Efficiency Solar Cell Based on Dye-Sesitized Colloidal TiO_2 Films. *Nature* **1991**, *353*, 737–739.

(33) Mishra, A.; Fischer, M. K. R.; Bäuerle, P. Metal-Free Organic Dyes for Dye-Sensitized Solar Cells : From Structure : Property Relationships to Design Rules Angewandte. *Angew. Chemie Int. Ed.* **2009**, *48*, 2474–2499.

(34) Wang, J.; Liu, K.; Ma, L.; Zhan, X. Triarylamine: Versatile Platform for Organic, Dye-Sensitized, and Perovskite Solar Cells. *Chem. Rev.* **2016**, *116*, 14675–14725.

(35) Boschloo, G.; Hagfeldt, A.; Spectus, C. O. N. Characteristics of the Iodide/Triiodide Redox Mediator in Dye-Sensitized Solar Cells. *Acc. Chem. Res.* **2009**, *42*, 1819–1826.

(36) Koops, S. E.; Barnes, P. R. F.; O'Regan, B. C.; Durrant, J. R. Kinetic Competition in a Coumarin Dye-Sensitized Solar Cell: Injection and Recombination Limitations upon Device Performance. *J. Phys. Chem. C* **2010**, *114*, 8054–8061.

(37) Kallioinen, J.; Benkö, G.; Sundström, V.; Korppi-Tommola, J. E. I.; Yartsev, A. P. Electron Transfer from the Singlet and Triplet Excited States of $Ru(dcbpy)_2$ $(NCS)_2$ into Nanocrystalline TiO_2 Thin Films. *J. Phys. Chem. B* **2002**, *106*, 4396–4404.

(38) Bisquert, J. Chemical Diffusion Coefficient of Electrons in Nanostructured Semiconductor Electrodes and Dye-Sensitized Solar Cells. *J. Phys. Chem. B* **2004**, *108*, 2323–2332.

CHAPTER 2. ELECTRON PARAMAGNETIC RESONANCE

Electron Paramagnetic Resonance spectroscopy (EPR), also known as Electron Spin Resonance (ESR), is based on the interaction between electron spins and an external magnetic field, provided by the spectrometer. It involves electronic transitions between different spin-states, allowing to study the interaction of the spin with the magnetic field and also mutual electron-electron and electron-nuclear spin interactions.

In this Chapter, the basic principles of EPR will be introduced and a brief description of the techniques used in the thesis will be given.

2.1 Magnetic interactions and the Spin Hamiltonian

The quantum-mechanical tool for the interpretation of EPR spectra is the *Spin Hamiltonian* ($\widehat{\mathbf{H}}_0$), dating back to the early days of magnetic resonance, in the 1950s. It is the energy operator accounting for the spin part of the electronic wavefunction, so that the EPR spectrum of the system can be interpreted in terms of allowed transitions between the eigenstates of this Hamiltonian. It contains only spin coordinates, expressed by the electron and nuclear spin vector operators $\widehat{\boldsymbol{S}}$ and $\widehat{\boldsymbol{I}}$, and phenomenological parameters accounting for the interactions of the spins with the applied magnetic field and with each other.

The total spin hamiltonian $\widehat{\mathbf{H}}_0$ can be expressed as a sum of the contributions stemming from the various magnetic interactions:

$$\widehat{\mathbf{H}}_0 = \widehat{\mathbf{H}}_{\mathrm{eZ}} + \widehat{\mathbf{H}}_{\mathrm{nZ}} + \widehat{\mathbf{H}}_{\mathrm{hy}} + \widehat{\mathbf{H}}_{\mathrm{nQ}} + \widehat{\mathbf{H}}_{\mathrm{ZFS}} \qquad \text{Eq. 2.1}$$

where the terms in the right member refer to the electron and nuclear Zeeman interactions, the hyperfine interaction, the nuclear quadrupolar interaction and the electron dipolar (or Zero-field splitting) interaction.

These interactions will be considered in detail in the following sections.

2.1.1 Electron Zeeman interaction

The magnetic dipole moment associated to the spin angular momentum of a free electron is defined as:

$$\hat{\boldsymbol{\mu}}_e = -\frac{g_e \mu_B}{\hbar} \hat{\boldsymbol{S}} \qquad \text{Eq. 2.2}$$

where g_e is the free electron g-factor (2.0023193), $\mu_B$is the Bohr magneton (9.274×10^{-24}J/T), $\hbar$ is the reduced Planck constant (1.0546×10^{-34}J·s) and $\hat{\boldsymbol{S}}$ is the spin angular momentum.

In presence of a static external magnetic field $\vec{B}_0$, the energy associated to the interaction between the electron magnetic moment and the field, known as Zeeman interaction, is given by:

$$\mathrm{E} = -\hat{\boldsymbol{\mu}}_e \cdot \vec{B}_0 \qquad \text{Eq. 2.3}$$

Therefore, the Zeeman Hamiltonian can be written as:

$$\hat{\mathbf{H}}_{\mathrm{eZ}} = -\hat{\boldsymbol{\mu}}_e \cdot \vec{B}_0 = \frac{g_e \mu_B}{\hbar} \hat{\boldsymbol{S}} \cdot \vec{B}_0 \qquad \text{Eq. 2.4}$$

Since the quantization axis of the angular momentum coincides with the direction of the applied magnetic field, Eq. 2.4 can be re-written as:

$$\hat{\mathbf{H}}_{\mathrm{eZ}} = -\hat{\boldsymbol{\mu}}_e \cdot \vec{B}_0 = \frac{g_e \mu_B}{\hbar} B_0 \hat{\boldsymbol{S}}_z \qquad \text{Eq. 2.5}$$

Hence, the Zeeman eigenstates coincide with the $\hat{\boldsymbol{S}}_z$ operator eigenfunctions and their eigenvalues are:

$$E = g_e \mu_B B_0 m_s \qquad \text{Eq. 2.6}$$

where m_s is the secondary spin quantum number ($m_s = -S, \dots, +S$). From Eq. 2.6 the energy separation between the two electron spin states α ($m_s = +1/2$) and β ($m_s = -1/2$) is given by:

$$\Delta E = g_e \mu_B B_0 \qquad \text{Eq. 2.7}$$

In case of atoms and molecules possessing electronic spin, the interaction between the ground state spin angular momentum and the orbital angular momentum of close excited states (spin-orbit coupling) introduces a deviation in the g-factor with respect to the g_e value. The g-factor is described as a second-rank tensor quantity $\bar{\bar{\boldsymbol{g}}}$ and the Zeeman Hamiltonian is therefore:

$$\hat{\mathbf{H}}_{\mathrm{eZ}} = \frac{\mu_B}{\hbar} \hat{\boldsymbol{S}} \cdot \bar{\bar{\boldsymbol{g}}} \cdot \vec{B}_0 \qquad \text{Eq. 2.8}$$

The g-tensor can be diagonalized, i.e. a proper reference system (the so-called *principal-axes* system) can be found, in which the tensor assumes a diagonal form. Therefore, the tensor is fully described by its three principal values (the tensor eigenvalues):

$$\bar{\bar{\boldsymbol{g}}} = \begin{pmatrix} g_{XX} & 0 & 0 \\ 0 & g_{YY} & 0 \\ 0 & 0 & g_{ZZ} \end{pmatrix} \qquad \text{Eq. 2.9}$$

The consequence of having a tensorial g-factor is that the energy of the spin states inside the magnetic field depends on the orientation of the molecule with respect to $\vec{B}_0$. Therefore, also the ΔE between the states, coinciding with the energy ($h\nu$) of the EPR transition, depends on molecular orientation. In disordered solid samples, where the molecular orientations are randomly distributed, the EPR spectrum is given by the superposition of lines arising from EPR transitions at each molecular orientation (*powder spectrum*). The spectrum also shows some turning points corresponding to those molecular orientations in which the principal $\overline{\overline{\boldsymbol{g}}}$ axes are parallel to the magnetic field (see Figure 2.1). In liquid solutions, the fast molecular tumbling averages out the anisotropy of the Zeeman interaction and the resulting EPR spectrum consists of a single line at $g_{iso} = \frac{1}{3}(g_{XX} + g_{YY} + g_{ZZ})$.

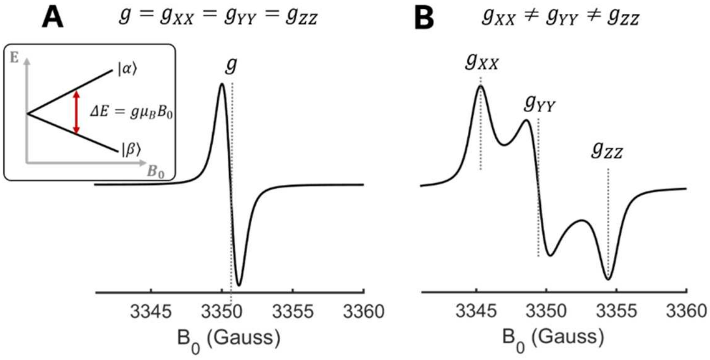

Figure 2.1 First-derivative spectrum of a S=1/2 species with isotropic (A) or rhombic (B) g-tensor.

2.1.2 Nuclear Zeeman interaction

The magnetic dipole moment associated to the nuclear spin angular momentum $\hat{\boldsymbol{I}}$ is defined as:

$$\hat{\boldsymbol{\mu}}_n = \frac{g_n \mu_n}{\hbar}\hat{\boldsymbol{I}} \qquad \text{Eq. 2.10}$$

in which g_n and μ_n are the nuclear g-factor and the nuclear Bohr magneton (5.05×10^{-27}J/T), respectively.

The nuclear Zeeman interaction between $\hat{\boldsymbol{\mu}}_n$ and the applied magnetic field can be described by the hamiltonian:

$$\hat{\mathbf{H}}_{\mathrm{nZ}} = -\frac{g_n \mu_n}{\hbar}\hat{\boldsymbol{I}} \cdot \vec{B}_0 = -\frac{g_n \mu_n}{\hbar} B_0 \hat{\boldsymbol{I}}_z \qquad \text{Eq. 2.11}$$

implying an energy separation between the nuclear spin states equal to:

$$\Delta E = h\nu_0 = g_n \mu_n B_0 \qquad \text{Eq. 2.12}$$

The g_n value is a specific property of the nucleus, therefore the nuclear Zeeman frequency (ν_0) can be used to identify the resonant nucleus. Since the nuclear Bohr magneton is three orders of magnitude lower than the electron Bohr magneton, the nuclear Zeeman interaction is much smaller compared to the electronic Zeeman.

2.1.3 Hyperfine interaction

The hyperfine interaction is the interaction between electron and nuclear spins. It is described by the spin Hamiltonian reported in Eq. 2.13, composed of two contributions, the so-called Fermi contact or isotropic interaction ($\widehat{\mathbf{H}}_{\mathrm{hy,F}}$), and the electron-nuclear dipolar interaction ($\widehat{\mathbf{H}}_{\mathrm{hy,dip}}$).

$$\widehat{\mathbf{H}}_{\mathrm{hy}} = \widehat{\mathbf{H}}_{\mathrm{hy,F}} + \widehat{\mathbf{H}}_{\mathrm{hy,dip}} = a_{iso}\widehat{\boldsymbol{S}}\cdot\widehat{\boldsymbol{I}} + \widehat{\boldsymbol{S}}\cdot\overline{\overline{\boldsymbol{A}}}_{dip}\cdot\widehat{\boldsymbol{I}} = \widehat{\boldsymbol{S}}\cdot\overline{\overline{\boldsymbol{A}}}\cdot\widehat{\boldsymbol{I}} \qquad \text{Eq. 2.13}$$

The isotropic hyperfine coupling constant a_{iso} is given by:

$$a_{iso} = \frac{2}{3}\frac{\mu_0}{\hbar} g_e \mu_B g_n \mu_n |\psi_0(0)|^2 \qquad \text{Eq. 2.14}$$

where $|\psi_0(0)|^2$ is the ground state electron spin density at the nucleus. Besides s-type orbitals, also p, d and f atomic orbitals can contribute to the Fermi contact interaction by means of electron-polarization mechanisms generating a nonzero spin density at the nucleus. Similarly, spin-polarization phenomena explain the isotropic hyperfine coupling of α protons in organic π radicals[1].

The origin of the dipolar component of the hyperfine interaction is the interaction between the electronic and nuclear magnetic dipole moments, which is described by the dipolar hamiltonian:

$$\widehat{\mathbf{H}}_{\mathrm{hy,dip}} = \frac{\mu_0}{4\pi\hbar} g_e \mu_B g_n \mu_n \left[\frac{3(\widehat{\boldsymbol{S}}\cdot\vec{r})(\vec{r}\cdot\widehat{\boldsymbol{I}})}{r^5} - \frac{\widehat{\boldsymbol{S}}\cdot\widehat{\boldsymbol{I}}}{r^3}\right] = \widehat{\boldsymbol{S}}\cdot\overline{\overline{\boldsymbol{A}}}_{dip}\cdot\widehat{\boldsymbol{I}} \qquad \text{Eq. 2.15}$$

where $\vec{\boldsymbol{r}}$ is the distance vector between the two spins and r indicates its modulus.

The hyperfine dipolar tensor $\overline{\overline{\boldsymbol{A}}}_{dip}$ resulting from Eq. 2.15 is traceless and symmetric, with principal values given by:

$$A_{dip,i} = \frac{\mu_0}{4\pi\hbar} g_e \mu_B g_n \mu_n \left\langle \psi_0 \middle| \frac{3{r_i}^2 - r^2}{r^5} \middle| \psi_0 \right\rangle \qquad \text{Eq. 2.16}$$

where the bra-ket notation indicates integration over the spatial coordinates of the wavefunction. Being traceless, this interaction is averaged out in low-viscosity solutions due to the rapid molecular tumbling. Therefore, in this case only the Fermi contact interaction is effective.

2.1.4 Nuclear quadrupolar interaction

Nuclei with spin $I > 1/2$ have a non-spherical charge distribution described by a nuclear electrical quadrupole moment Q. If the nucleus is surrounded by an asymmetric charge density generating an electric field gradient (EFG), then the interaction of the quadrupole moment with the EFG, known as *nuclear quadrupolar interaction* (NQI), is effective and can be described by the Hamiltonian:

$$\widehat{\mathbf{H}}_{\mathrm{nQ}} = \hat{\boldsymbol{I}} \cdot \bar{\bar{\boldsymbol{P}}} \cdot \hat{\boldsymbol{I}} \qquad \text{Eq. 2.17}$$

The nuclear quadrupolar tensor is traceless and its diagonal form can be written as:

$$\bar{\bar{\boldsymbol{P}}} = \frac{e^2 qQ}{4\mathrm{I}(2\mathrm{I}-1)\hbar} \begin{pmatrix} \eta - 1 & 0 & 0 \\ 0 & -\eta - 1 & 0 \\ 0 & 0 & 2 \end{pmatrix} \qquad \text{Eq. 2.18}$$

where e is the elementary charge, eq is the biggest component of the EFG tensor, and η is an asymmetry parameter describing the deviation of the field gradient from axial symmetry.

2.1.5 Zero-field splitting interaction

The so-called Zero-Field Splitting (ZFS) interaction between electron spins originates from two contributions: the spin-spin dipolar interaction and the spin-orbit interaction. In organic systems the spin-orbit interaction is usually small, therefore, only the contribution from the magnetic dipolar interaction between electronic spins will be considered in the following.

The magnetic dipole-dipole interaction between electron spins has the same origin of the hyperfine dipolar interaction between electron and nuclear spins illustrated in section 2.1.3, which can be described classically as the interaction between the magnetic dipole moments of the two spins.

Considering two electron spins S_1 and S_2, as in a triplet state ($S = 1$), and their related dipole moments $\boldsymbol{\mu}_1$ and $\boldsymbol{\mu}_2$, the hamiltonian associated to this interaction can be written as:

$$\widehat{\mathbf{H}}_{\mathrm{dip}} = \frac{\mu_0}{4\pi}\left[\frac{\hat{\boldsymbol{\mu}}_1 \cdot \hat{\boldsymbol{\mu}}_2}{r^3} - \frac{3(\hat{\boldsymbol{\mu}}_1 \cdot \vec{\boldsymbol{r}})(\hat{\boldsymbol{\mu}}_2 \cdot \vec{\boldsymbol{r}})}{r^5}\right] \qquad \text{Eq. 2.19}$$

Assuming an isotropic g-factor for both electrons, the dipolar Hamiltonian written in terms of spin operators is:

$$\widehat{\mathbf{H}}_{\mathrm{dip}} = \frac{\mu_0}{4\pi} g_1 g_2 {\mu_B}^2 \left[\frac{\widehat{\boldsymbol{S}}_1 \cdot \widehat{\boldsymbol{S}}_2}{r^3} - \frac{3(\widehat{\boldsymbol{S}}_1 \cdot \vec{\boldsymbol{r}})(\widehat{\boldsymbol{S}}_2 \cdot \vec{\boldsymbol{r}})}{r^5}\right] \qquad \text{Eq. 2.20}$$

in which $\vec{\boldsymbol{r}}$ is the distance vector between the two spins and r indicates its modulus.

Transformation of Eq. 2.20 with replacement of the single spin operators $\widehat{\boldsymbol{S}}_1$ and $\widehat{\boldsymbol{S}}_2$ with the total spin operator $\widehat{\boldsymbol{S}}$ ($\widehat{\boldsymbol{S}} = \widehat{\boldsymbol{S}}_1 + \widehat{\boldsymbol{S}}_2$), leads to the expression:

$$\widehat{\mathbf{H}}_{\mathrm{dip}} = \widehat{\boldsymbol{S}} \cdot \bar{\bar{\boldsymbol{D}}} \cdot \widehat{\boldsymbol{S}} \qquad \text{Eq. 2.21}$$

where $\bar{\bar{\boldsymbol{D}}}$ is the dipolar or zero-field splitting (ZFS) tensor defined as:

$$\overline{\overline{\boldsymbol{D}}} = \frac{\mu_0}{8\pi}\frac{g_1 g_2 {\mu_B}^2}{\langle r^5 \rangle}\begin{pmatrix} \langle r^2 - 3{r_x}^2 \rangle & \langle -3r_x r_y \rangle & \langle -3r_x r_z \rangle \\ \langle -3r_x r_y \rangle & \langle r^2 - 3{r_y}^2 \rangle & \langle -3r_y r_z \rangle \\ \langle -3r_x r_z \rangle & \langle -3r_y r_z \rangle & \langle r^2 - 3{r_z}^2 \rangle \end{pmatrix} \qquad \text{Eq. 2.22}$$

in which r_i are the components of the distance vector $\vec{\boldsymbol{r}}$ in the adopted reference system and the parentheses indicate integration over the spatial coordinates of the electronic wavefunction.

The dipolar tensor is symmetric and traceless, therefore it is fully described by two parameters, D and E, defined in terms of its principal values (D_X, D_Y, D_Z):

$$D = \frac{3}{2} D_Z \qquad \text{Eq. 2.23}$$

$$E = \frac{1}{2}(D_X - D_Y) \qquad \text{Eq. 2.24}$$

Conventionally, the principal values of $\overline{\overline{\boldsymbol{D}}}$ are designated according to the rule $|D_Z| > |D_X| \geq |D_Y|$ implying that $|D/3| \geq |E|$. According to this convention, the Z principal axis is defined as the direction of maximum dipolar interaction. From Eq. 2.22-24 the physical meaning of the D and E parameters can be understood. The D -value is related to the average distance r between the electrons, thus it can be used to estimate the electron delocalization of the triplet wavefunction, while the E parameter measures the deviation of the spin-distribution from axial symmetry.

Diagonalization of the dipolar Hamiltonian in Eq. 2.21 for a triplet state system yields the eigenstates T_X, T_Y and T_Z, defined as linear combinations of the $\widehat{\boldsymbol{S}}^2$ eigenstates for the triplet ($T_{+1} = |1{,}1\rangle$, $T_0 = |1{,}0\rangle$, $T_{-1} = |1,-1\rangle$):

$$\begin{aligned} T_Z &= T_0 \\ T_X &= \frac{1}{\sqrt{2}}(T_{-1} - T_1) \qquad \text{Eq. 2.25} \\ T_Y &= \frac{i}{\sqrt{2}}(T_{-1} + T_1) \end{aligned}$$

having eigenvalues:

$$\begin{aligned} E_Z &= -D_Z = -\frac{2}{3}D \\ E_X &= -D_X = \frac{1}{3}D - E \qquad \text{Eq. 2.26} \\ E_Y &= -D_Y = \frac{1}{3}D + E \end{aligned}$$

This shows that the dipolar interaction removes the degeneracy of the triplet sublevels by an amount depending on the D and E parameters according to Eq. 2.26. Such an energy splitting is the splitting between the triplet substates in absence of any magnetic field, therefore it is referred to as *Zero-field splitting*, which is also the alternative name given to the dipolar interaction and tensor.

2.2 Triplet-state EPR spectrum

During an EPR experiment on a triplet-state system, like the photoexcited triplet state of organic molecules, a static magnetic field $\vec{B}_0$ is applied, therefore, the Zeeman interaction between the spin and the field must be included in the spin Hamiltonian of the system. Considering an isotropic g-factor, the spin-hamiltonian can be written as:

$$\widehat{\mathbf{H}}_{\mathrm{tripl}} = \frac{g\mu_B}{\hbar}\widehat{\boldsymbol{S}} \cdot \vec{B}_0 + \widehat{\boldsymbol{S}} \cdot \overline{\overline{\boldsymbol{D}}} \cdot \widehat{\boldsymbol{S}} \qquad \text{Eq. 2.27}$$

Hyperfine interactions can be neglected as they are much smaller than the ZFS interaction and usually unresolved in triplet spectra, thus they were not included in Eq. 2.27.

The eigenstates of the hamiltonian in Eq. 2.27 depend both on the orientation of the molecule in the magnetic field, due to the anisotropy of the ZFS interaction, and on the strength of the applied magnetic field B_0. For the case of $\vec{B}_0$ parallel to the Z principal axis of the dipolar tensor, the eigenfunctions of the triplet state hamiltonian are[2,3]:

$$\begin{aligned} \varphi_Z &= T_0 = T_Z \\ \varphi_X &= sin\theta \cdot T_{-1} - cos\theta \cdot T_{+1} \\ \varphi_Y &= cos\theta \cdot T_{-1} + sin\theta \cdot T_{+1} \end{aligned} \qquad \text{Eq. 2.28}$$

with $tan2\theta = (D_X - D_Y)/2g\mu_B B_0$. In case of very small B_0, $\theta = \pi/4$ and the triplet eigenfunctions approach the zero-field ones (T_X, T_Y and T_Z defined by Eq. 2.25). On the other hand, in the high-field approximation, $\theta = n\pi$ (with integer n including 0) and the wavefunctions approach the $\widehat{\boldsymbol{S}}^2$ eigenstates (T_{+1}, T_0, T_{-1}).

The associated eigenvalues are:

$$\begin{aligned} E_Z &= -D_Z = -\frac{2}{3}D \\ E_X &= \frac{1}{3}D + \sqrt{g^2{\mu_B}^2 B_0^2 + E^2} \\ E_Y &= \frac{1}{3}D - \sqrt{g^2{\mu_B}^2 B_0^2 + E^2} \end{aligned} \qquad \text{Eq. 2.29}$$

showing that the energy of the state corresponding to the Z principal axis of the dipolar tensor is independent on B_0 and coincides with the zero-field energy, while the others depend on the field value.

In general, for $\vec{B}_0$ parallel to each one of the principal axes of the ZFS tensor, the corresponding state coincides with the zero-field state, i.e. the ZFS eigenstate, and preserves the zero-field energy, while the other states are a mix of the zero-field eigenstates with energies that depend on B_0. The energy levels dependence on the strength of $\vec{B}_0$ is shown in Figure 2.2A.

The $\Delta m_s = \pm 1$ selection rule allows for two transitions for each molecular orientation, involving the adjacent triplet sublevels ($T_{-1} \leftrightarrow T_0$ and $T_0 \leftrightarrow T_{+1}$, labeled respectively as the "–" and "+" transitions). Since the two transitions have different energies, the resonance condition for them is met by sweeping the strength of $\vec{B}_0$ (as the frequency of the electromagnetic radiation is fixed in the EPR setup), which gives rise to a spectrum distributed over a range of B_0.

This $\Delta m_s = \pm 1$ rule strictly holds only in the high field approximation, since the m_s is not a good quantum number for the system in case of comparable Zeeman and dipolar interactions. In this case also $\Delta m_s = 2$ transitions can be observed, but they require a smaller resonant magnetic field, so they don't contribute to the $\Delta m_s = \pm 1$ spectrum.

All molecular orientations contribute to the EPR spectrum, each one giving rise to two spin transitions. However, in powder systems, i.e. samples with randomly distributed molecular orientations, the spectrum shows turning points (peaks) corresponding to the $\Delta m_s = \pm 1$ transitions in the molecules oriented with the principal axes of the ZFS tensor parallel to $\vec{B}_0$, also called *canonical* orientations. In the description of the spectra these transitions are often referred to as the *X, Y or Z components* or *transitions*.

An example of spectrum is reported in Figure 2.2B, where a thermal equilibrium population of the triplet substates was assumed, resulting in absorptive transitions.

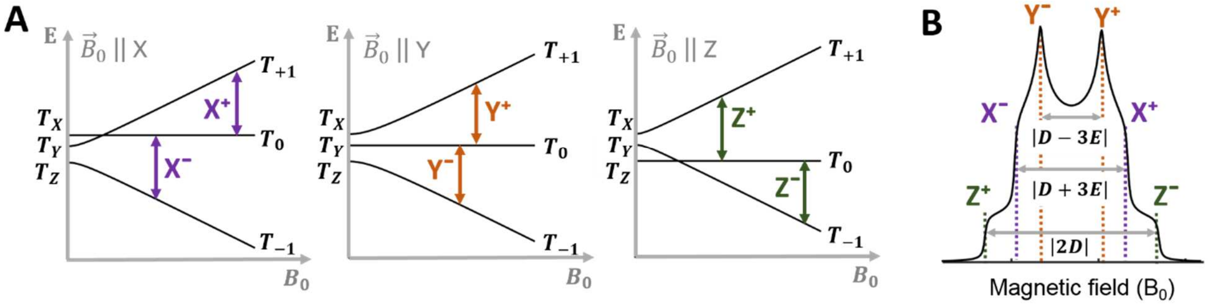

Figure 2.2 A: Energy levels of a triplet state (for positive D and negative E) as a function of the applied magnetic field, for each canonical orientation. The allowed EPR transitions are indicated. B: Resulting EPR spectrum assuming a Boltzmann distribution of populations.

Photoexcited triplet states are generated with an out-of-equilibrium population distribution, called *spin-polarization*. The following section introduces two common spin-polarization mechanisms of photoexcited triplet states, that are relevant to this thesis.

2.2.1 Spin-polarization mechanisms in photoexcited triplet states

The mechanism of formation of the photoexcited triplet state determines the population of the triplet sublevels and consequently the so-called *polarization pattern* of its EPR spectrum, that can be used to identify the process.

The common mechanisms generating excited triplet states in organic molecules are Intersystem-crossing (ISC) and charge recombination, that will be discussed in the following.

2.2.1.1 Intersystem Crossing

Intersystem crossing is the process enabling the transition between states of different spin-multiplicity. When a molecule is photoexcited, ISC may induce the transition from the excited singlet state to the triplet, as it often occurs in organic molecules and conjugated polymers as those studied in this thesis.

ISC is driven by the spin-orbit (SO) interaction between the spin and the orbital angular momenta, described by the hamiltonian $\widehat{\mathbf{H}}_{\mathrm{SO}} = -\lambda \widehat{\boldsymbol{L}} \cdot \widehat{\boldsymbol{S}}$, which mixes singlet and triplet states so that the $\Delta S = 0$ selection rule is no more valid. Since the spin-orbit coupling scales approximately with the fourth power of the atomic number[4], ISC is especially effective when heavy elements are involved. However, organic molecules can have consistent ISC rates due to the small energy difference between singlet and triplet vibronic states[5].

The ISC rate from the singlet state S_1 to the triplet zero-field substates T_X, T_Y and T_Z is related to the SO coupling matrix elements $\langle S_1 | \widehat{\mathbf{H}}_{\mathrm{SO}} | T_X \rangle$, $\langle S_1 | \widehat{\mathbf{H}}_{\mathrm{SO}} | T_Y \rangle$, $\langle S_1 | \widehat{\mathbf{H}}_{\mathrm{SO}} | T_Z \rangle$ which in general have different values. Therefore, ISC is a selective mechanism that produces a non-equilibrium population of the triplet sublevels. In presence of a magnetic field, the mixing of the zero-field states implies also the mixing of their ISC populations, which determines the spin-polarization of the high-field states. A typical polarization pattern of a ISC triplet is shown in Figure 2.3, where an enhanced ISC rate was assumed for the T_Z state and D was taken positive.

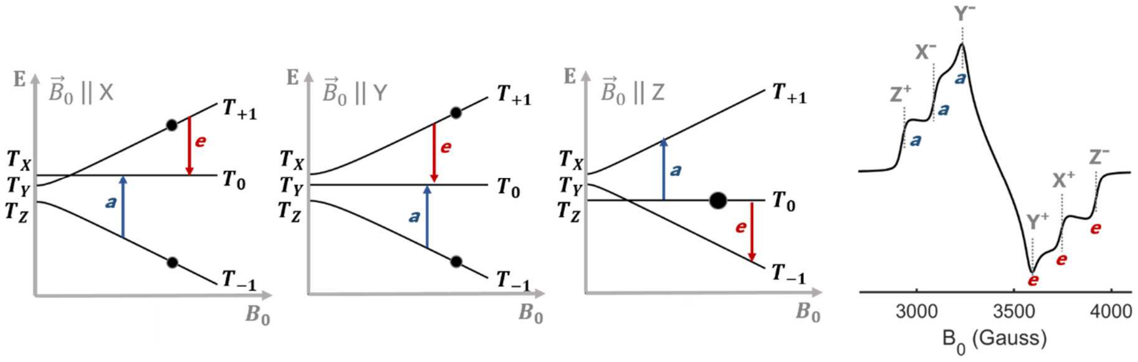

Figure 2.3 Scheme of the energy levels of a triplet state (with positive D and negative E) populated by ISC, assuming a selective population of the T_Z state (zero-field populations $P_X : P_Y : P_Z = 0.2 : 0.1 : 1$) with indication of the emissive (*e*) and absorptive (*a*) transitions and the resulting EPR spectrum.

2.2.1.2 Charge-recombination

In electron donor-acceptor (D-A) systems where photoexcitation induces electron-transfer, the recombination of charges can lead in some circumstances to the formation of the triplet state of D and/or A rather than their singlet ground states (see Chapter 1, section 1.4.2). The driving force of the process is the energy difference between the charge-transfer (CT) states and the triplet state, which must have lower energy.

In this case, the spin-polarization of the triplet state is determined by the precursor, i.e. the CT state, which transfers its polarization to the neutral triplet state of the molecule[6,7,8]. Therefore, to understand the origin of the polarization pattern of triplet states generated by charge recombination, the spin-polarization of the precursor CT states must be analyzed.

From the point of view of spins, the charge-transfer states can be modeled as *spin-correlated radical pairs* (SCRP). SCRPs are radical pairs in which the distance between the radical cation and anion is such that the two spins are weakly coupled by means of the exchange and dipolar interaction ($r = 1 \div 2$ nm). Therefore, the Hamiltonian of the SCRP, assuming isotropic g-factors for the two spins, is:

$$\widehat{\mathbf{H}} = \widehat{\mathbf{H}}_{\mathrm{eZ}} + \widehat{\mathbf{H}}_{\mathrm{exch}} + \widehat{\mathbf{H}}_{\mathrm{dip}} = \frac{g_1\mu_B}{\hbar}\widehat{\boldsymbol{S}}_1 \cdot \vec{B}_0 + \frac{g_2\mu_B}{\hbar}\widehat{\boldsymbol{S}}_2 \cdot \vec{B}_0 - 2J\widehat{\boldsymbol{S}}_1 \cdot \widehat{\boldsymbol{S}}_2 + \widehat{\boldsymbol{S}} \cdot \overline{\overline{\boldsymbol{D}}} \cdot \widehat{\boldsymbol{S}} \qquad \text{Eq. 2.30}$$

The exchange interaction is a quantum-mechanical effect due to the permutation symmetry of the electronic wavefunction which is antisymmetric with respect to the permutation of electrons (Pauli exclusion principle). This interaction becomes relevant when the orbitals of the two spins overlap significantly and consequently the two electrons can be exchanged. The J constant expresses the magnitude of the exchange coupling and it decays exponentially with the distance between electrons.

The interplay of the Zeeman, exchange and dipolar interactions produces a mixing of the singlet state (S) with the T_0 triplet substate, called S -T_0 *mixing*, as shown by the eigenstates of the Hamiltonian[9]:

$$\varphi_1 = T_{+1}$$

$$\varphi_2 = cos\theta \cdot S + sin\theta \cdot T_0 \qquad \text{Eq. 2.31}$$

$$\varphi_3 = -sin\theta \cdot S + cos\theta \cdot T_0$$

$$\varphi_4 = T_{-1}$$

where the mixing angle θ is defined by:

$$tan2\theta = \mu_B B_0(g_1 - g_2)/(2J - D_z) \qquad \text{Eq. 2.32}$$

In general, the SCRP can form upon electron-transfer from the excited singlet or triplet state of the D or A molecule, leading to the so-called *singlet-precursor* or *triplet-precursor* SCRP. However, the only case relevant to the discussion of recombination of SCRPs to triplet states is the singlet-precursor case, since the triplet excited state in this case must have lower energy compared to the SCRP. In a SCRP with singlet-precursor, the states with some singlet character (the S -T_0 mixed-states φ_2 and φ_3) are selectively populated, leading to spin-polarization of the radical pair. Such a spin-polarization is transferred to the neutral triplet state formed upon recombination of the SCRP, in which the T_0 state acquires the largest population. The resulting polarization pattern of the triplet state EPR spectrum is shown in Figure 2.4, where the dependence on the sign of the D parameter is also highlighted.

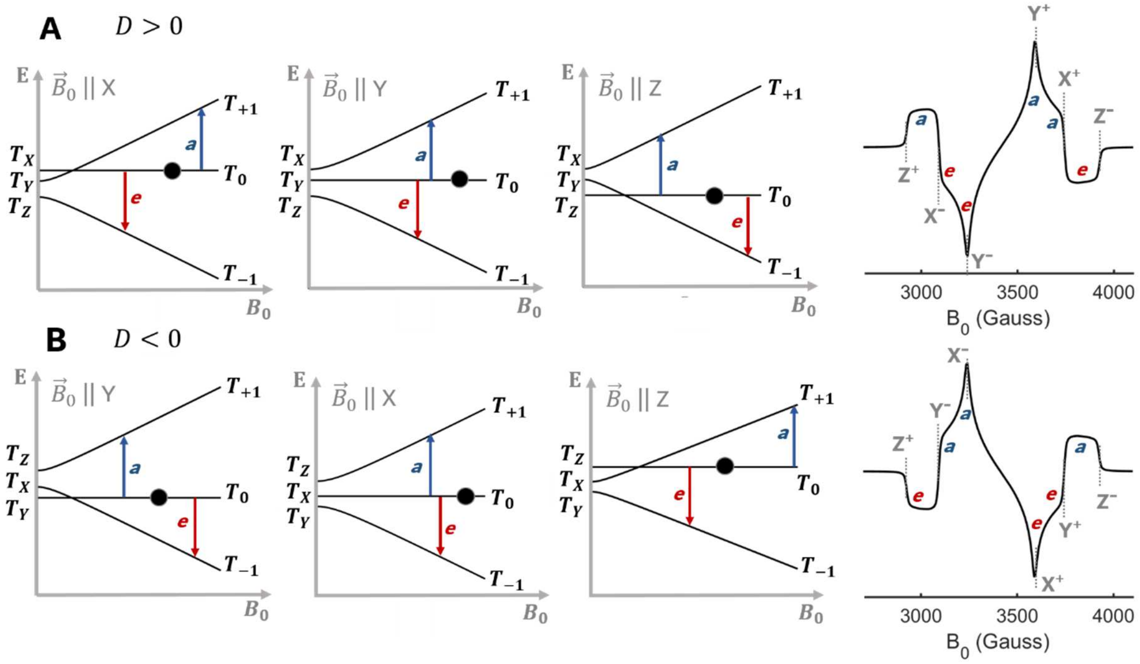

Figure 2.4 Energy levels and EPR spectrum of a triplet state populated by charge recombination, with selective population of the T_0 state, for positive (A) and negative (B) D value.

Recombination of singlet-precursor SCRPs can also lead to excess population of the T_{-1} and T_{+1} sublevels in the resulting triplet state. Indeed, the S -T_0 mixed-states of the SCRP (φ_2 and φ_3) have an enhanced recombination rate to the singlet ground-state with respect to the pure-triplet states (φ_1 and φ_4), for which this process is spin-forbidden and therefore slower[10]. As a consequence, if recombination to the ground state is sufficiently fast compared to recombination to the triplet state, the population of the φ_2 and φ_3 states is rapidly depleted resulting in an excess population of the φ_1 and φ_4 states, that is then transferred to the T_{-1} and T_{+1} sublevels of the triplet state. In this case, the polarization pattern of the EPR spectrum of the triplet is opposite to that reported in Figure 2.4, being *eaaeea* for $D > 0$ and *aeeaae* for $D < 0$.

Regardless of which kind of spin-polarization scheme the triplet state acquires from the recombining SCRP, consisting in either an excess population of the T_0 or the T_{-1} and T_{+1} levels, the resulting spectral polarization pattern is fully distinct from the ISC pattern, enabling for the assignment of the triplet generation mechanism from the EPR spectrum.

2.3 Spin relaxation

In EPR experiments, spin-systems are perturbed by an electromagnetic field in the microwave frequency region, which induces transitions between spin states. The processes restoring thermal equilibrium after microwave excitation are known as *spin-relaxation* mechanisms.

Two kind of spin relaxation processes can be distinguished, namely the *spin-lattice* or *longitudinal* relaxation and the *spin-spin* or *transverse* relaxation.

Spin-lattice relaxation phenomena involve an exchange of energy between the spin and the environment, associated to a transition between the spin-states, called *spin-flip*. In this way, spin-lattice phenomena act on the populations of the electron spin states restoring the thermal-equilibrium population distribution, with a characteristic time known as the *longitudinal relaxation time* (T_1).

Spin-flips are induced by local magnetic field fluctuations experienced by the spins. In liquid samples, the main source of spin-lattice relaxation is molecular motion. Indeed, molecular motion causes a modulation of the anisotropic interactions (Zeeman, hyperfine, electron dipolar), which creates fluctuating local magnetic fields that can induce spin-flip transitions if the fluctuations have a frequency component coinciding with the spin resonance frequency. Fluctuating magnetic fields can also be induced by collisions between molecules, therefore the longitudinal relaxation is slower in diluted solutions, where collisions between spins is less probable. In solid samples, spin-lattice relaxation is mediated by low-frequency solid-state dynamics, inducing fluctuations of the magnetic interactions.

Spin-spin relaxation processes do not involve an exchange of energy with the environment, since they are characterized by so-called *flip-flop* processes, in which two interacting spins undergo a transition between the spin states such that energy is conserved (one spin changes from the α to the β state providing energy for the other spin to undergo the opposite transition). These processes do not involve a change in spin population, but they destroy phase coherence between spins, with the characteristic *transverse relaxation* time T_2. As for spin-lattice relaxation phenomena, spin-spin relaxation is also induced by fluctuations in the magnetic field experienced by the spins.

2.4 EPR Techniques

EPR techniques rely on the use of a static magnetic field ($\vec{B}_0$), causing a Zeeman splitting in the energy levels of the paramagnetic species, and an electromagnetic field (microwave radiation, whose oscillating magnetic field is labelled as $\vec{B}_1(t)$), which induces transitions between the spin states. In EPR spectrometers the microwave frequency is kept fixed while the magnitude of $\vec{B}_0$ is varied to meet the resonance condition for each *spin-packet* (spin ensemble with a given resonance frequency) that composes the sample.

The various EPR techniques can be divided into Continuous-Wave (CW) and Pulse EPR methods, the first relying on continuous microwave irradiation of the sample, while the latter employ short microwave pulses, temporally separated from signal detection.

The basic principles of both CW and Pulse EPR methods will be illustrated in the following sections.

2.4.1 CW-EPR

A simple description of the continuous-wave EPR experiment can be given in the frame of a semiclassical model, the Bloch vectorial model, in which the electron spin is described by the associated magnetic dipole moment vector ($\vec{\boldsymbol{\mu}}$, see Eq. 2.2 in section 2.1.1). For a collection of N (non-interacting) spins, like those contained in a macroscopic sample, the *magnetization* ($\vec{\boldsymbol{M}}$) can be defined as the resultant macroscopic magnetic moment per unit volume:

$$\vec{\boldsymbol{M}} = \frac{1}{V}\sum_{i=1}^{N} \vec{\boldsymbol{\mu}}_i \qquad \text{Eq. 2.33}$$

In absence of a magnetic field, a paramagnetic sample has null magnetization, since the single magnetic moments are randomly oriented (in the quantum-mechanical description this corresponds to the degeneracy of spin-states in absence of magnetic field, involving equal population of the α and β states). On the other hand, the presence of a static magnetic field $\vec{B}_0$, like that applied during EPR experiments, induces a net magnetization parallel to the field ($M_z \neq 0$). This phenomenon is caused by the Zeeman interaction (see section 2.1.1) between $\vec{B}_0$ and the single magnetic moments, that tends to align them to the field to lower the energy of the system (in quantum-mechanical terms it creates an energy splitting between the α and β states, inducing a higher equilibrium population of the lower energy state). Figure 2.5 gives a pictorial representation of the equilibrium magnetization in the static magnetic field.

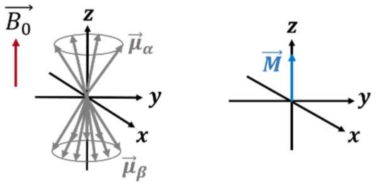

Figure 2.5 Pictorial representation of the individual magnetic moments in a static magnetic field (left) and the resulting magnetization (right).

When the oscillating magnetic field of the microwave radiation ($\vec{B}_1(t)$) is introduced in the xy plane, the equilibrium of the system is perturbed, since the magnetization experiences a torque that induces a time evolution expressed by the following equation of motion:

$$\frac{d\vec{\boldsymbol{M}}}{dt} = \gamma\vec{\boldsymbol{M}} \times \vec{\boldsymbol{B}} = \gamma\vec{\boldsymbol{M}} \times (\vec{B}_0 + \vec{B}_1) \qquad \text{Eq. 2.34}$$

where γ is the magnetogyric ratio ($\gamma = g\mu_B/\hbar$). By moving from the static frame to a rotating reference frame, in which the new x' and y' axes rotate around $z' = z$ with an angular frequency ω equal to the microwave frequency, and by introducing the longitudinal and transverse relaxation, Eq. 2.34 can be written as[2]:

$$\begin{aligned} \frac{dM_x}{dt} &= (\omega - \omega_0)M_y - \frac{M_x}{T_2} \\ \frac{dM_y}{dt} &= -(\omega - \omega_0)M_x + \gamma B_1 M_z - \frac{M_y}{T_2} \\ \frac{dM_z}{dt} &= -\gamma B_1 M_y - \frac{M_z - M_z^{eq}}{T_1} \end{aligned} \qquad \text{Eq. 2.35}$$

where $\vec{B}_1$ was taken along the x axis, and ω_0 is the resonance or *Larmor* frequency of the spin ($\omega_0 = -\gamma B_0$).

In stationary-state conditions ($\frac{dM_i}{dt} = 0$), as in the CW-EPR experiment, the solution of Eq. 2.35 for the resonance condition ($\omega = \omega_0$) is a relaxation-damped precession motion of the magnetization around the direction of $\vec{B}_1$, in which the longitudinal relaxation tends to restore the equilibrium magnetization along z, while the transverse relaxation cancels out the M_x and M_y components.

The EPR signal is proportional to the y component of the magnetization:

$$M_y = M_z^{eq} \frac{\gamma B_1 T_2}{1+(\omega-\omega_0)^2 \cdot T_2^2 + \gamma^2 B_1^2 T_1 T_2} \qquad \text{Eq. 2.36}$$

and it is described by the equation[2]:

$$f(\omega) = \chi_0 \omega_0 \frac{T_2}{1+(\omega-\omega_0)^2 \cdot T_2^2 + \gamma^2 B_1^2 T_1 T_2} \qquad \text{Eq. 2.37}$$

where χ_0 is the static *magnetic susceptibility* of the sample, a quantity directly proportional to the equilibrium magnetization M_z^{eq}. For small B_1, the term $\gamma^2 B_1^2 T_1 T_2$ at the denominator (also called *saturation factor* as explained below) can be neglected and Eq. 2.37 turns into a Lorentzian function centered at $\omega = \omega_0$, with a full width at half maximum (FWHM) equal to $2/T_2$. In CW-EPR experiments, the first-derivative of $f(\omega)$ is observed, due to the lock-in detection employing a modulation of the B_0 field.

This model applies to the CW-EPR experiment on a single spin-packet, i.e. a spin-ensemble composed of non-interacting spins experiencing the same time-average magnetic field and therefore having the same resonance frequency ω_0. In this situation the EPR line is said to be *homogeneously-broadened* and has a FWHM directly related to the spin-spin-relaxation time (FWHM$= 2/T_2$). However, this case is quite uncommon in real samples, especially in solids, where EPR lines are usually affected by the so-called *inhomogeneous broadening*. Inhomogeneously-broadened lines arise from the presence of a distribution of resonance frequencies which is due in general to the anisotropy of the magnetic interactions and to unresolved hyperfine couplings. In this case the EPR line is an envelope of Lorentzians, which is described by a Gaussian lineshape. Homogeneously broadened lines can be observed in liquid samples, if the anisotropies are averaged out by sufficiently fast molecular tumbling, and if the hyperfine interactions are well resolved.

From Eq. 2.37 it can be seen that the CW-EPR signal depends on the value of B_1, i.e. on the microwave power P ($P = {B_1}^2$), *via* the power saturation factor $s = \gamma^2 B_1^2 T_1 T_2$.
For $\gamma^2 B_1^2 T_1 T_2 \approx 1$ and > 1 the s term at the denominator in Eq. 2.37 cannot be neglected and it induces a decrease in amplitude and a broadening of the EPR signal. The physical reason of this phenomenon is the saturation of the EPR transition, due to the unfavorable balance between the transition rate (proportional to B_1^2) and the rate of spin relaxation (expressed by the inverse of T_1 and T_2) which restores the equilibrium populations of the states. In saturation conditions, spin relaxation is not sufficiently fast with respect to the transition rate, leading to a small steady-state population difference between the spin states with consequent reduced transition probability and signal intensity. Therefore, the longer are the relaxation times of the system, the smaller microwave power should be used in order to avoid signal saturation effects.
The dependence of the peak-to-peak intensity (I) of the first derivative CW-EPR signal on the microwave power is given by[11]:

$$I = \frac{\sqrt{P}}{(1+P/P_0)^{b/2}} \qquad \text{Eq. 2.38}$$

in which the P_0 parameter is defined as the microwave power level at which the saturation factor $\gamma^2 B_1^2 T_1 T_2$ equals 1. Eq. 2.38 holds for both homogeneous and inhomogeneous EPR lines, the b exponent being 3 for purely homogeneously-broadened lines and 1 for ideally inhomogeneously-broadened lines. The shape of the resulting saturation curve (I versus $\sqrt{P}$) is reported in Figure 2.6A while Figure 2.6B shows the effect of microwave power on the linewidth.

The acquisition of saturation curves, through the so-called power-saturation experiments, in which the microwave power is varied, are useful to identify the optimal P value for maximum EPR intensity and to provide indication on the type of EPR line (homogeneous or inhomogeneous). In case of systems with more than one paramagnetic species having different relaxation times, acquiring the spectrum at different P values allows to conveniently vary the relative intensities of the two signals.

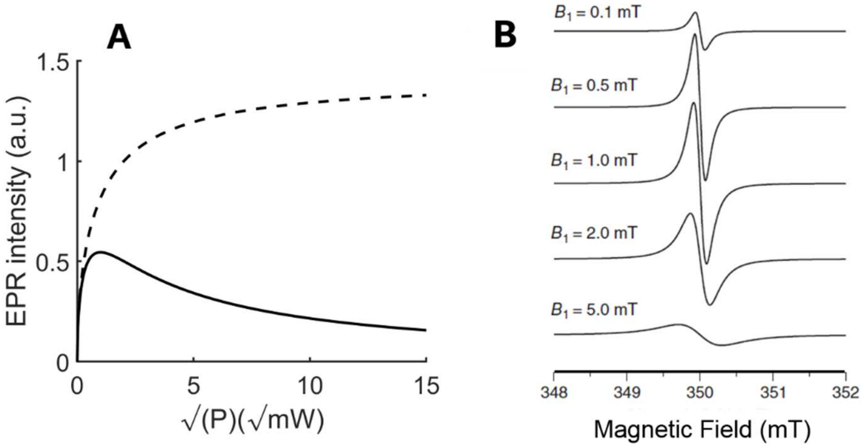

Figure 2.6 Saturation curves (left) for a homogeneous (thick line) and inhomogeneous (dashed line) EPR signal; linewidth dependence on B_1 (right).

The application of EPR to the study of processes occurring in photovoltaic materials under illumination requires the use of a photoexcitation source during the experiment. Photoexcitation can be continuous or pulsed and it distinguishes between the Light-induced and Time-resolved CW-EPR techniques (abbreviated as LEPR and TR-EPR respectively), that will be illustrated in the following sections.

2.4.1.1 Continuous photoexcitation in cw EPR: LEPR

In Light-induced EPR the sample is illuminated continuously during the time of the experiment. Since EPR is not selective for photogenerated species, the spectrum acquired under illumination (*light-on* spectrum) accounts for both light-induced and pristine paramagnetic species. Therefore, the spectrum recorded in absence of illumination (*dark* spectrum) is subtracted from the light-on one yielding the spectrum of the photogenerated species (*light-induced* spectrum or LEPR).

Since continuous illumination is used, the LEPR signal can be considered to be proportional to the steady-state concentration of the light-induced species, which is dictated by the balance between their rates of formation and annihilation. Hence, short-lived species (lifetime below milliseconds) are not detected by LEPR because of the small steady-state concentration falling below the spectrometer sensitivity. As a result, in photovoltaic materials LEPR cannot be used to detect spin-correlated radical pairs or triplet states as they typically have lifetimes in the microsecond or submicrosecond time scale. However, LEPR is useful to detect stable radicals.

Like in standard CW-EPR, LEPR spectra are in first-derivative form due to the use of field modulation and lock-in detection in order to increase the signal-to-noise ratio (SNR).

2.4.1.2 Pulse photoexcitation in cw EPR: TR-EPR

Time-resolved EPR is based on the use of pulse sample irradiation, provided by a laser source, for the photogeneration of paramagnetic species, whose transient EPR signal is then recorded under continuous microwave irradiation. It enables to follow the time-evolution of the photo-induced species EPR signal, from few nanoseconds after the laser pulse to several microseconds[12].

The laser flash is used to trigger the acquisition of the time-dependent signal at a fixed applied magnetic field B_0, in a time interval up to hundreds of microseconds after the laser flash (limited by the laser repetition rate), by the use of a digital oscilloscope. After the accumulation of a sufficient number of time-profiles (*transients*), in order to obtain the desired SNR, the magnetic field is swept as to cover the entire range of resonances. The resulting dataset is a two-dimensional matrix reporting the intensity of microwave absorption as a function of both the magnetic field and the time after the laser-flash (see Figure 2.7).

In the raw data matrix, the actual EPR signal of transient photogenerated species (light-induced species with lifetime below the laser shot repetition time) is superimposed to the background signal of the resonator and to the signal of pristine non-photogenerated species and stable light-induced species (with lifetime above the laser shot repetition time). Therefore, data manipulation is required to filter out the undesired contributions. Subtraction of the transient signal offset, i.e. the mean value of the EPR response before the laser pulse, from each transient, allows to eliminate the contribution of the pristine and the long-lived photo-induced components. The resonator background signal, which is independent on the magnetic field, can be filtered out by subtracting the off-resonance signal intensity from the spectra at each time point. In this way the processed data matrix contains only the contribution from the EPR signal of the photogenerated short-lived species. TR-EPR spectra can then be extracted from the 2D dataset as data vectors at given times after the laser flash.

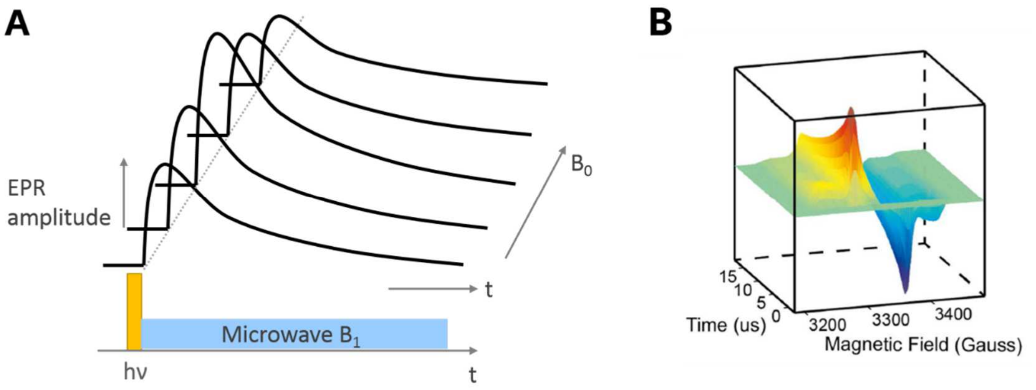

Figure 2.7 Scheme for the TR-EPR experiment (A) and example of dataset (B).

Besides the use of pulse optical excitation, the TR-EPR set-up differs from steady-state CW EPR (like LEPR) for the signal detection, called *direct detection* because the microwave power reflected from the resonator is directly detected and then recorded by a digital oscilloscope instead of passing through the lock-in amplifier, as in steady-state techniques. Avoiding field modulation and lock-in detection allows to increase the temporal resolution of the experiment, which is limited by the detection bandwidth and is usually around 100 ns. Another consequence of eliminating field modulation is that the sign of the TR-EPR signal reflects the spin-polarization of the EPR transition, being positive for absorptive transitions and negative for emissive ones.

The gain in time resolution associated to the direct and broad-bandwidth detection scheme, is accompanied by a loss in sensitivity. Therefore, TR-EPR is confined to spin-systems exhibiting large spin-polarization, which can compensate for the low sensitivity by increasing the population difference between the spin states and hence the transition probability. This condition is satisfied for transient paramagnetic species generated by a laser flash in photovoltaic materials, like triplet states and spin-correlated radicals pairs, that can be successfully detected by TR-EPR.

2.4.2 Pulse-EPR

Pulse-EPR techniques are based on the use of short microwave pulses to excite EPR transitions, followed by the detection of the signal in absence of microwave irradiation.

Various pulse sequences have been developed, that allow to study specific interactions and properties of the spin-system like hyperfine couplings, electron-electron dipolar couplings and relaxation times. Some of these have been used in this thesis and will be briefly described in the following sections.

Sample photoexcitation can be continuous or pulsed like in CW-EPR. In the case of pulsed photoexcitation, the laser pulse can be synchronized with the microwave pulse sequence, that can be programmed to start at a fixed delay after the laser-flash (*daf*). In this way, the pulse-EPR spectrum of the photogenerated species at a given *daf* can be obtained after subtraction of the signal of the pristine non-photogenerated species. Transient species like triplet states can be probed in this mode. Under continuous illumination the steady-state concentration of photogenerated species is probed by the experiment. In this thesis we employed continuous illumination during Pulse-EPR experiments, as they were used to investigate stable species (radicals), therefore pulse photoexcitation was not needed.

The simplest Pulse-EPR techniques can be described in the frame of the vector model introduced in section 2.4.1 to rationalize CW-EPR experiments.
Before any microwave (MW) pulse, every spin-packet in the system is in thermal equilibrium with a net magnetization along the direction (z) of the static magnetic field. The effect of a microwave pulse with magnetic field B_1 along x and frequency ω, in a frame rotating around z with $\omega_{rot} = \omega$, is to rotate the M_z magnetization around x, according to the Bloch equations in Eq. 2.35, where the relaxation terms can be neglected since in this case the MW radiation occurs in a time interval much shorter than the relaxation times (only few nanoseconds). The rotation has angular frequency $\omega_1 = -\gamma B_1$ and as a result M_z is rotated by an angle $\alpha = \omega_1 t_p$, also called flip-angle, where t_p is the pulse duration. For $\alpha = \pi/2$ the pulse rotates the z magnetization along the y axis. The rise of a transverse magnetization along y corresponds to the excitation of a transition between spin-states.
This precession motion strictly applies to the magnetization of on-resonance spin-packets, i.e. spin-packets with resonance frequency ω_0 equal to the radiation frequency ω. Off-resonance spin-packets precess around the direction of the total magnetic field ($\vec{B}_0 + \vec{B}_1$) with frequency $\Delta\omega = \omega - \omega_0$. Therefore, after a $\pi/2$ pulse, the magnetization vector of off-resonance spins has a residual z component. However, for strong B_1 (*hard* pulses) the effect of the $\vec{B}_1$ field on off-resonance spin-packets dominates on the effect of $\vec{B}_0$ and they tend to behave like on-resonance spins.
After the $\pi/2$ pulse, the MW radiation is turned off and the M_y magnetization experiences only the static magnetic field $\vec{B}_0$ along z. Therefore, the motion of $\vec{\boldsymbol{M}}$ is described by Bloch equations analogous to those reported in Eq. 2.35 where B_1 is zero. In this case relaxation must be taken into account since the time intervals between pulses can be several hundreds of nanoseconds long. The resulting motion is a precession of the magnetization around the z axis, at frequency $\Delta\omega$, damped by relaxation that progressively cancels out the transverse magnetization and restores the equilibrium magnetization along z. Consequently, the M_x and the M_y components oscillate in the xy plane yielding the so-called *free-induction decay* signal (FID).

In most samples, the anisotropic magnetic interactions (Zeeman, hyperfine, dipolar) lead to the presence of a distribution of resonance frequencies i.e. many spin-packets exist. In this situation, the total transverse magnetization (the FID) decays rapidly owing to the dephasing of the spin packets with different frequencies $\Delta\omega$ in the xy plane. Therefore, typically most of the FID decays in a time period which is below the dead-time of the spectrometer (the time after the pulse during which detection cannot start due to technical reasons). However, the use of a second pulse with π flip-angle, after a time period τ from the first $\pi/2$ pulse, can be used to refocus the magnetizations at time $t = 2\tau$, resulting in the so-called *electron spin-echo*. The sequence $\frac{\pi}{2} - \tau - \pi - \tau$ is known as the *Hahn Echo* sequence (see Figure 2.8) and it is largely used in Pulse-EPR for the detection of the magnetization signal.

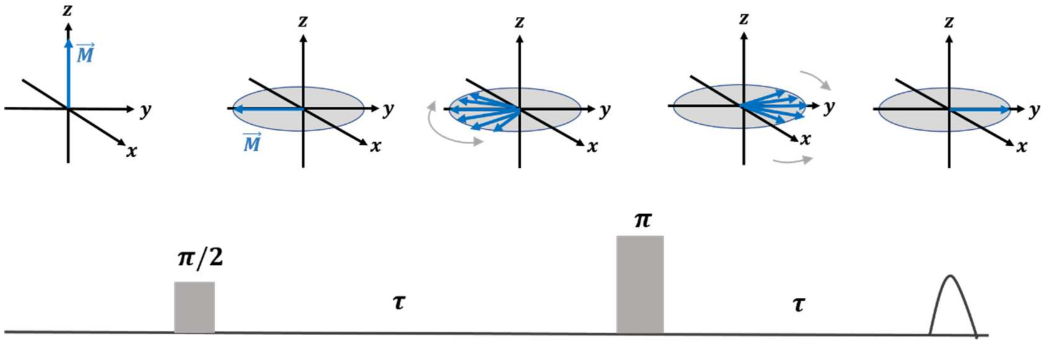

Figure 2.8 Two-pulse (Hahn) echo sequence.

During the τ time transverse relaxation is effective, causing a reduced echo intensity for increasing τ. Typically, the spectrometer dead-time imposes a minimum τ value of about 100 ns. Consequently, spin-packets with a comparable or smaller T_2 are undetectable.

2.4.2.1 EDEPR

The Echo-Detected EPR (EDEPR) or Field-Swept Electron Spin Echo (FSESE) experiment is performed by sweeping the applied magnetic field and recording the electron spin-echo integrated area at each B_0 value. The echo sequence can be the 2-pulse Hahn Echo or the 3-pulse *stimulated* echo sequence $(\frac{\pi}{2} - \tau - \frac{\pi}{2} - T - \frac{\pi}{2} - \tau - echo)$.

The shape of the EDEPR spectrum corresponds to the shape of the integrated CW spectrum, unless line distortions occur in one or the other experiments. EDEPR avoids distortions that could be present in CW-EPR spectra due to the field modulation of the signal. On the other hand, the EDEPR lineshape may be distorted by orientation dependent relaxation times (anisotropic relaxation), responsible for the alteration of the relative signal intensity between different fields. Therefore, it is often useful to compare EDEPR and CW lines to evaluate the real shape of the EPR signal of the investigated species.

EDEPR is particularly useful to detect species characterized by slow relaxation times, whose signal easily saturate in CW-EPR experiments. Furthermore, in case of overlapping species with different relaxation times, EDEPR can be used to suppress the spectrum of the fast-relaxing species by using sufficiently long interpulse delays.

2.4.2.2 Relaxation

Relaxation times can be measured by specific pulse EPR techniques.

The *Inversion-recovery* (IR) experiment is designed to measure the T_1 spin-lattice relaxation time. As shown in Figure 2.9, its pulse sequence consists in a π pulse separated by the Hahn-echo sequence through a time interval T. The resulting echo intensity at a fixed magnetic field is measured at variable T values. The first pulse inverts the magnetization of the spin-packet which is gradually restored along the $+z$ direction by the longitudinal spin-relaxation acting during the T time interval. As a consequence, the gradual increase of T causes the detected spin-echo to change its sign from negative to positive, with an exponential behavior given by:

$$f(T) \propto 1 - 2e^{-T/T_1} \qquad \text{Eq. 2.39}$$

Therefore, the spin-lattice relaxation time can be determined from a fitting of the IR curve.

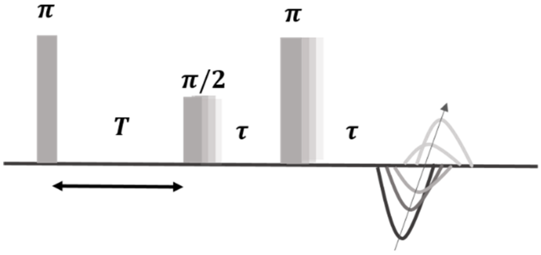

Figure 2.9 Inversion Recovery pulse sequence.

If multiple spin-packets are simultaneously excited in the experiment and they have different T_1 times, the IR curve deviates from a mono-exponential behavior.

The spin-spin relaxation time T_2 can be measured from the Hahn-Echo sequence by systematically increasing the τ interpulse delay (Figure 2.10). Indeed, the transverse relaxation, acting during the τ delays, induces the exponential decay of the echo intensity with τ:

$$f(\tau) \propto e^{-2\tau/T_2} \qquad \text{Eq. 2.40}$$

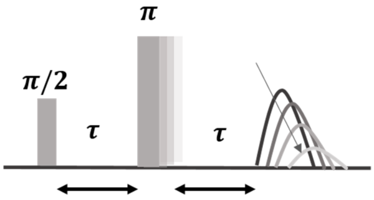

Figure 2.10 Two-pulse echo decay for T_2 measurement.

2.4.2.3 ESEEM

In presence of electron-nuclear hyperfine interactions, the time-decay of the electron spin-echo amplitude is modulated at frequencies corresponding to the nuclear resonance frequencies in the electron spin manifolds. This effect is known as *Electron Spin Echo Envelope Modulation* (ESEEM) and it is widely used to measure hyperfine coupling constants.

The understanding of the ESEEM phenomenon and its related techniques requires to refer to the quantum-mechanical description of magnetic resonance. In this approach, the collection of spins (spin-packet) probed by the experiment is described by the density matrix, a useful tool of widespread use in statistical mechanics allowing to describe the state of the spin ensemble. The diagonal elements of the density matrix correspond to the populations of the states while the off-diagonal terms represent coherent superpositions of states referred to as *coherences*. A spin-system at thermal equilibrium has all off-diagonal elements equal to zero and diagonal elements reflecting the existence of a macroscopic longitudinal magnetization, which arises in presence of a population difference between the states. When a microwave field induces transitions between the states, it makes some off-diagonal elements non-zero, because it introduces coherences. The concept of transverse magnetization precessing at a particular frequency corresponds to the coherence of the related transition. For instance, a $\pi/2$ pulse acting on a $S = 1/2$ system at equilibrium generates the coherence corresponding to the transition $\Delta m_s = 1$.

Given these premises, a qualitative description of the ESEEM experiment on a system composed of one electron spin S interacting with a nuclear spin I by means of the hyperfine interaction will be given in the following.

The $S = 1/2$, $I = 1/2$ spin system is described by four spin-states, namely $|\alpha_S\alpha_I\rangle$, $|\beta_S\beta_I\rangle$, $|\alpha_S\beta_I\rangle$, $|\beta_S\alpha_I\rangle$. In Figure 2.11 the 'allowed' ($\Delta m_s = 1$, $\Delta m_I = 0$) and 'forbidden' ($\Delta m_s = 1$, $\Delta m_I = 1$) transitions between these states are indicated. In case of anisotropic hyperfine interaction having comparable magnitude with the nuclear Zeeman interaction, the $|m_S m_I\rangle$ states are mixed (they are not eigenstates for the system) and, as a consequence, m_S and m_I do not represent good quantum numbers causing the $\Delta m_s = 1, \Delta m_I = 0$ selection rule to break down.

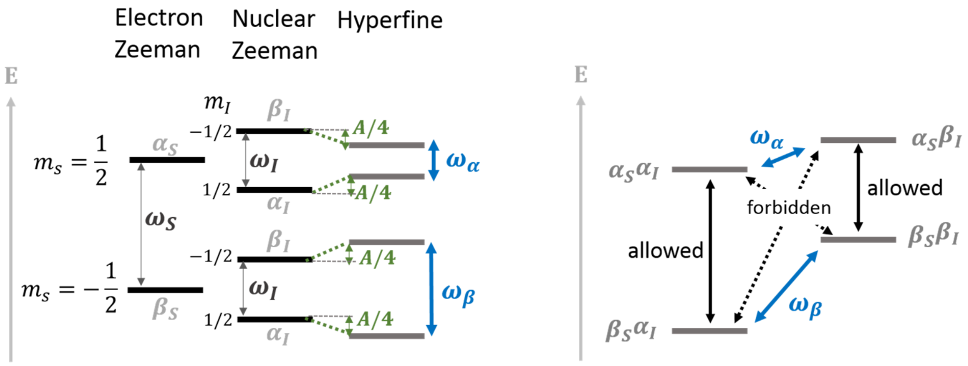

Figure 2.11 Energy levels for the $S = 1/2$, $I = 1/2$ spin system and related transitions. A is the effective hyperfine coupling at the given molecular orientation in the magnetic field.

In this frame, the 'forbidden' transitions have non-zero transition probabilities. Therefore, if a $\pi/2$ pulse is applied, all the four transitions will be excited (the corresponding four coherences will be generated). The evolution of the coherences in the time τ after the pulse can be visualized as the precession motion of the corresponding four magnetizations in the xy plane with frequencies equal to the transition frequencies. If a π pulse is then applied, the magnetizations are rotated about the x axis but also a coherence transfer between different transitions occurs[13], which can be seen as a transfer of magnetization between the different magnetization vectors. In the following evolution time, the contributions to each magnetization arising from the coherence-transfer will not be along y at the time τ after the π pulse, since their precession frequency has changed from the first τ evolution time. Therefore, the echo amplitude (proportional to M_y at the time τ after the last pulse) is reduced, by an amount depending on τ and on the precession frequencies. As a result, the echo amplitude as a function of τ is periodically modulated according to the equation[13]:

$$\mathrm{E}_{mod}(\tau) = 1 - \frac{k}{4}\left[2 - 2cos\omega_\alpha\tau - 2cos\omega_\beta\tau + cos(\omega_\alpha + \omega_\beta)\tau + cos(\omega_\alpha - \omega_\beta)\tau\right] \quad \text{Eq. 2.41}$$

where k is the modulation-depth constant and ω_α and ω_β are the nuclear frequencies in the two electron spin manifolds: $\omega_\alpha = \omega_I - A/2$, $\omega_\beta = \omega_I + A/2$ with ω_I being the nuclear Zeeman resonance frequency and A the hyperfine coupling constant.

This modulation is superimposed to the Hahn-echo decay induced by the transverse relaxation. However, by fitting the decay and subtracting it from the ESEEM time-trace, the echo modulation can be isolated. It is then Fourier-transformed to obtain a spectrum made of peaks at the frequencies ω_α, ω_β and the 'combination' frequencies $(\omega_\alpha - \omega_\beta)$, $(\omega_\alpha + \omega_\beta)$.

The just described experiment is the so-called *Two-Pulse ESEEM*, depicted in Figure 2.12A. Another kind of ESEEM experiment is the *Three-Pulse ESEEM*, schematized in Figure 2.12B. It consists in monitoring the stimulated echo $(\frac{\pi}{2} - \tau - \frac{\pi}{2} - T - \frac{\pi}{2} - \tau - echo)$ decay upon variation of the time T between the second and third pulse, and Fourier-transform the related modulation profile.

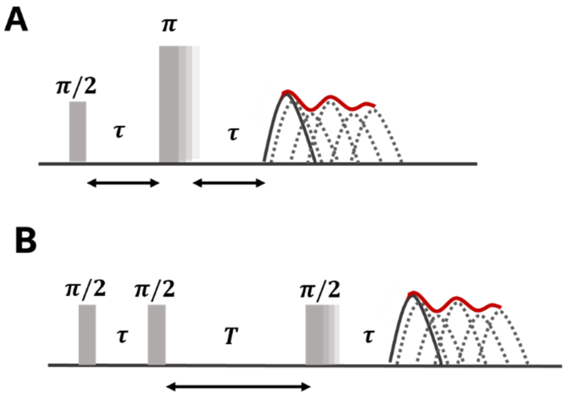

Figure 2.12 Two-pulse (A) and three-pulse (B) ESEEM sequences.

In this case the dynamics of the spins is different. The first $\pi/2$ pulse excites the four transitions generating the corresponding coherences as in the two-pulse experiment. However, the following $\pi/2$ pulse generates a coherence transfer from the electron to the nuclear coherences, which during the T time evolve with their nuclear frequencies ω_α and ω_β. The third $\pi/2$ pulse transfers the nuclear coherences back to electron coherences. As a result, these coherences will not be refocused at time τ after the last pulse, and if T is incremented the echo amplitude will be modulated according to the equation:

$$\mathrm{E}_{mod}(\tau, T) = 1 - \frac{k}{4}\left[(1 - cos\omega_\alpha\tau)\left(1 - cos\omega_\beta(\tau + T)\right) + (1 - cos\omega_\beta\tau)\left(1 - cos\omega_\alpha(\tau + T)\right)\right]$$

Eq. 2.42

As shown by this equation, the three-pulse ESEEM trace depends on both τ and T. The modulation at the nuclear frequency of one spin-manifold, $\omega_{\alpha/\beta}$, is suppressed for values of τ equal to $2\pi n/\omega_{\beta/\alpha}$ with $n = 1,2, \ldots$. This is the so-called *blind-spot* effect, causing the suppression of some nuclear frequencies depending on the chosen τ value. For this reason, three-pulse ESEEM spectra must be acquired at more than one τ value, and then summed in order to record the complete frequency spectrum. Despite this effect, the three-pulse ESEEM is in general more convenient compared to the two-pulse analog for various reasons. First, the stimulated echo decay upon variation of T is governed by the spin-lattice relaxation, therefore, the decay is usually much slower compared to the Hahn-echo decay since $T_1 > T_2$. Second, the combination frequencies $(\omega_\alpha - \omega_\beta)$, $(\omega_\alpha + \omega_\beta)$ are absent in the three-pulse echo modulation, which simplifies the spectrum. Furthermore, since nuclear coherences evolve in the incremented time delay T, the lineshape of the peaks is determined by the nuclear relaxation T_2, which is usually bigger than the electronic T_2, leading to smaller linewidths and better resolution in the spectra.

For both three- and two-pulse ESEEM experiments the fundamental requirement for the observation of a nuclear modulation effect is that the hyperfine interaction is anisotropic and of the same order of magnitude of the nuclear Zeeman interaction. Moreover, the B_0 magnetic field should not be aligned with any of the principal directions of the hyperfine tensor.

In case of more than one coupled nuclear spin, the ESEEM time trace can be derived as the product of the time traces due to each hyperfine-coupled nucleus. This leads to the appearance of combination frequencies between different nuclei. In case of two-pulse ESEEM all possible combinations occur, while in three-pulse ESEEM only combination of frequencies within the same electron spin manifold are possible.

2.4.2.4 HYSCORE

Hyperfine Sublevel Correlation Spectroscopy (HYSCORE) is a two-dimensional technique based on the ESEEM effect[14]. Its pulse sequence (see Figure 2.13) recalls the three-pulse ESEEM sequence with the addition of a π pulse between the second and third $\pi/2$ pulses. The time intervals t_1 and t_2 preceding and following the inversion pulse are both varied in the experiment, where the echo time trace is recorded as a function of t_1 for each t_2 value. Two-dimensional Fourier-transform of the 2D time trace leads to a frequency-domain spectrum displaying correlation peaks between the nuclear frequencies in the different electron spin manifolds.

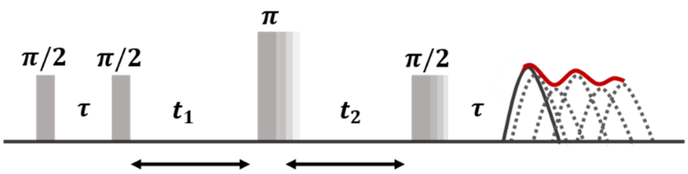

Figure 2.13 HYSCORE pulse sequence.

Although it is more time-consuming than mono-dimensional ESEEM, the bidimensionality of HYSCORE consistently improves the spectral resolution enabling to disentangle multiple hyperfine couplings.

Like in three-pulse ESEEM, the first $\pi/2$ pulse generates electron coherences evolving during the time τ that are then transferred to nuclear coherences by the second $\pi/2$ pulse. These nuclear coherences evolve during time t_1 with frequency corresponding to the nuclear transition frequency in the definite electron spin manifold in which they were generated. The π pulse then inverts the electron spin and consequently induces a transfer of the nuclear coherence to the other electron spin manifold, which determines the evolution frequency during the t_2 time interval. The last $\pi/2$ pulse transfers the nuclear coherences back to electron coherences to allow for their detection. These coherences refocus at time τ after pulse giving rise to an echo. The change in the evolution frequency of the nuclear coherence between the t_1 and t_2 delays gives rise to correlation peaks between the two frequencies (cross-peaks) in the HYSCORE spectrum. Diagonal peaks may arise if the inversion pulse provides incomplete transfer of nuclear coherences between the two manifolds.

Similarly to three-pulse ESEEM, HYSCORE is affected by the presence of blind-spots which imposes the necessity of acquiring multiple spectra at different τ values.

For a $S = 1/2\,, I = 1/2$ spin system the HYSCORE spectrum consists of two cross-peaks. These occur in the (+,+) quadrant in case of weak hyperfine coupling, i.e. $|A| < 2|\omega_I|$, and in the (-,+) quadrant in case of strong hyperfine coupling, i.e. $|A| > 2|\omega_I|$, as shown in Figure 2.14.

In case of powder samples, the peaks appear as elongated correlation *ridges*, due to the distribution of hyperfine couplings across the different molecular orientations. The typical shapes of the cross-peaks in case of axial hyperfine tensor ($\overline{\overline{\boldsymbol{A}}}_{dip}$ principal values: $A_{dip,X} = A_{dip,Y} = -\mathrm{T}$, $A_{dip,Z} = 2\mathrm{T}$) are reported in Figure 2.14, showing that information on both the isotropic and dipolar component of the interaction can be extracted from the spectrum.

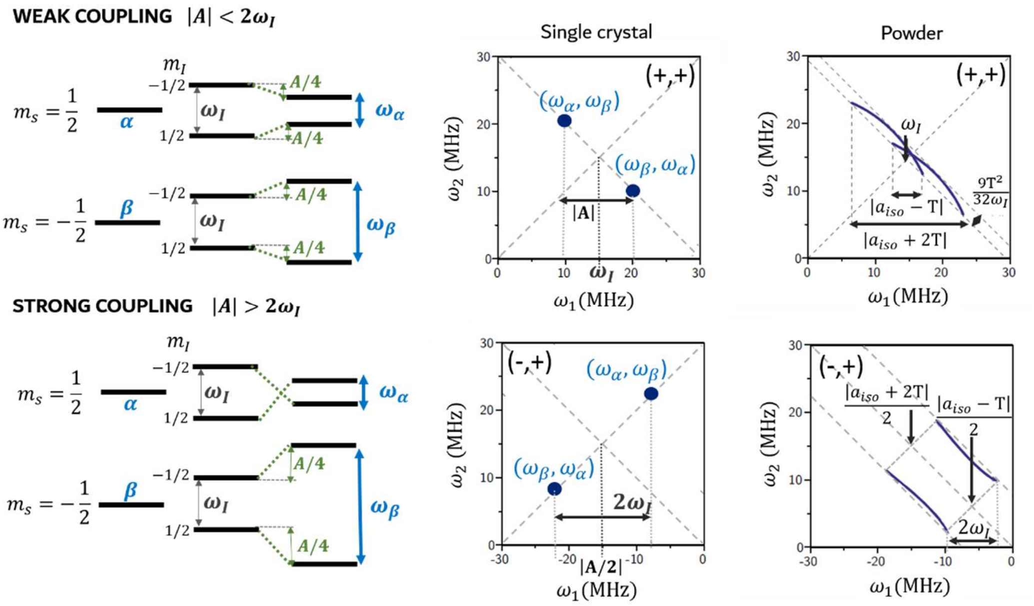

Figure 2.14 Energy levels for the S=1/2 , I=1/2 spin system and corresponding HYSCORE spectra for single crystal and powder samples.

In the case of an electron spin interacting with a $I = 1$ nucleus, like ^{2}H and ^{14}N, the spectrum is complicated by a higher number of cross peaks due to the presence of the nuclear quadrupolar interaction (NQI). Indeed, from the energy levels scheme of the system (see Figure 2.15) it can be seen that, in each electron spin manifold, two single-quantum transitions (SQ) ($\Delta m_I = 1$) and one double-quantum (DQ) transition ($\Delta m_I = 2$) are possible, leading to 36 cross-peaks. However, they have different intensities and only a part of them can be detected experimentally.

For nuclear spins with a strong quadrupolar interaction, like ^{14}N, the correlation peaks between the DQ transitions are usually the most intense, since the nuclear quadrupole interaction contributes in second order to the DQ frequencies (see Figure 2.15, showing that NQI first order shifts do not affect ΔE(DQ)), while the SQ peaks are less intense because they are broadened by the first order contribution of the nuclear quadrupole interaction to the SQ frequencies. The quadrant of the DQ cross-peaks depends on the magnitude of the hyperfine coupling, being the (+,+)/(-,+) quadrant for weak/strong coupling.

Under the assumptions of collinear hyperfine and dipolar parameters the DQ nuclear frequencies are equal to[11]:

$$\omega^{DQ}_{\alpha,\beta} = 2\sqrt{\left(\omega_I \pm \frac{A}{2}\right)^2 + \left(\frac{e^2Qq}{4h}\right)^2 (\eta^2 + 3)} \qquad \text{Eq. 2.43}$$

where A is the hyperfine coupling for the observed orientation, Q is the quadrupole moment, q is the EFG parameter and η is the quadrupolar asymmetry parameter.

However, the hyperfine and quadrupolar tensors are not in general collinear, and most samples are powder samples, where the inhomogeneous broadening of peaks (ridges) complicates the spectrum. Therefore, the interpretation of $I = 1$ HYSCORE spectra is in general not trivial. When performing spectral simulations, the number of variable parameters is quite high, since it includes the hyperfine and quadrupolar tensors and their mutual orientation.

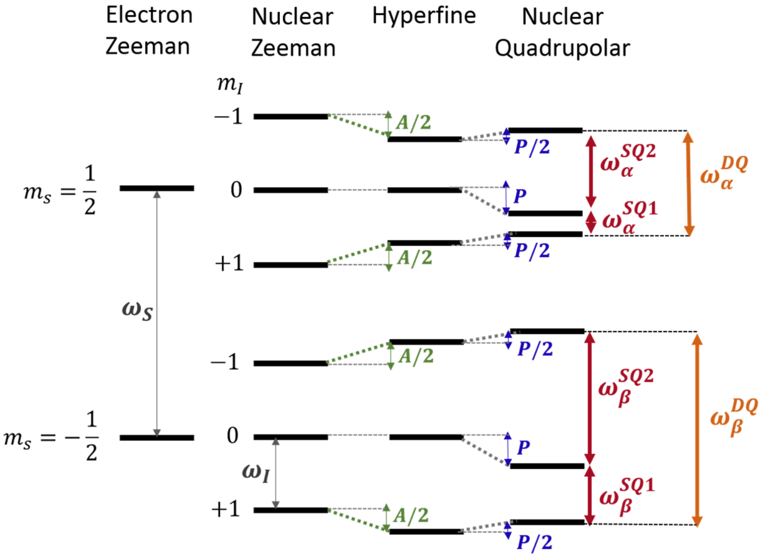

Figure 2.15 Energy levels diagram for the spin system $S = 1/2$, $I = 1$. A and P are the effective hyperfine and nuclear quadrupolar couplings for the given molecular orientation in the magnetic field. First-order nuclear quadrupolar shifts are reported, hence this scheme is valid for the case of small NQI compared to the nuclear Zeeman and hyperfine interactions. In case of strong NQI, like in ^{14}N, second order effects consistently affect the energy levels.

2.5 References

(1) Atherton, N. M. *Principles of Electron Spin Resonance*; Ellis Horwood: Chichester, 1993.

(2) Bolton, J. R.; Weil, J. A. *Electron Paramagnetic Resonance: Elementary Theory and Practical Applications*; John Wiley & Sons, 2007.

(3) Carrington, A.; McLachlan, A. D. *Introduction to Magnetic Resonance*; Chapman and Hall: London, 1979.

(4) Atkins, P. W. *Molecular Quantum Mechanics*; Oxford University Press: London, 1970.

(5) Marian, C. M. Spin-Orbit Coupling and Intersystem Crossing in Molecules. *Wiley Interdiscip. Rev. Comput. Mol. Sci.* **2012**, *2*, 187–203.

(6) Levanon, H.; Norris, J. R.; Levanon, H.; Norris, J. R. The Photoexcited Triplet State and Photosynthesis. *Chem. Rev.* **1978**, *78*, 185–198.

(7) Dance, Z. E. X.; Mi, Q.; McCamant, D. W.; Ahrens, M. J.; Ratner, M. A.; Wasielewski, M. R. Time-Resolved EPR Studies of Photogenerated Radical Ion Pairs Separated by P-Phenylene Oligomers and of Triplet States Resulting from Charge Recombination. *J. Phys. Chem. B* **2006**, *110*, 25163–25173.

(8) Niklas, J.; Beaupré, S.; Leclerc, M.; Xu, T.; Yu, L.; Sperlich, A.; Dyakonov, V.; Poluektov, O. G. Photoinduced Dynamics of Charge Separation: From Photosynthesis to Polymer–Fullerene Bulk Heterojunctions. *J. Phys. Chem. B* **2015**, *119*, 7407–7416.

(9) Buckley, C. D.; Hunter, D. a.; Hore, P. J.; McLauchlan, K. a. Electron Spin Resonance of Spin-Correlated Radical Pairs. *Chem. Phys. Lett.* **1987**, *135*, 307–312.

(10) Franco, L.; Toffoletti, A.; Ruzzi, M.; Montanari, L.; Carati, C.; Bonoldi, L.; Po', R. Time-Resolved EPR of Photoinduced Excited States in a Semiconducting polymer/PCBM Blend. *J. Phys. Chem. C* **2013**, *117*, 1554–1560.

(11) *EPR Spectroscopy: Fundamentals and Methods*, First Edit.; Goldfarb, D., Stoll, S., Eds.; John Wiley & Sons: Chichester, UK, 2018.

(12) *Advanced EPR: Applications in Biology and Biochemistry*; Hore, P. J., Ed.; Elsevier: Amsterdam, 1989.

(13) Schweiger, A.; Jeschke, G. *Principles of Pulse Electron Paramagnetic Resonance*; Oxford University Press: New York, 2001.

(14) Hofer, P.; Grupp, A.; Nebenfuhr, H.; Mehring, M. Hyperfine Sublevel Correlation (HYSCORE) Spectroscopy: A 2D ESR Investigation of the Squaric Acid Radical. *Chem. Phys. Lett.* **1986**, *132*, 279–282.

CHAPTER 3. MOLECULAR ORDER IN CONJUGATED POLYMER FILMS

Since the early development of Bulk Heterojunction Solar Cells (BHJSCs), it was clear that the photoactive films based on blends of conjugated polymers and small molecular acceptors, are rather heterogeneous materials with a great complexity of factors influencing their functionality. The morphology of the films, and in particular molecular packing and ordering, was soon acknowledged as a critical variable for the optimization of materials performance[1–9], and in some reports it is claimed to be as important as the chemical characteristics of the polymer and fullerene components[10,11]. Indeed, molecular arrangement and order were shown to be intimately related with the charge transport properties of the material[12,13].

Crystalline and amorphous phases coexist in polymer/fullerene films and the microstructure of the material is strongly affected by deposition parameters such as concentration of the solution, solvent, temperature and by the polymer molecular weight. The important role of the crystalline phase is widely recognized by a remarkable number of studies that correlate XRD-based analyses with charge mobility and charge transport studies, showing that crystalline domains drive the charge transport which is highly anisotropic. For the benchmark P3HT/PCBM blend and for other blends also, efficient hole transport is believed to preferentially occur in the interchain π-stacking direction[13,14,15]. Such anisotropy determines the relevance of crystallites' orientation and average order for the efficacy of charge transport inside the film. For example, it is generally accepted that a *face-on* orientation of P3HT chains favors vertical hole-transport and hole-collection in P3HT/PCBM solar cells.

As far as P3HT was involved, being a polymer with a strong self-organization ability that forms highly ordered films, the amorphous regions were considered to be detrimental for charge transport, although they appeared fundamental for creating an interface between the polymer and fullerene phases, where charge generation occurs. However, the efficiency of charge transport observed in the new emerging class of low-bandgap donor-acceptor copolymers, has changed this belief. Indeed, these polymers usually display a very low crystallinity, which does not undermine charge mobility. The explanation for this behavior was found in the presence of non-crystalline domains that are not completely amorphous but contain small π-aggregates with short-range orientational order and lacking translational order, that are responsible for charge transport [8,16].

Therefore, molecular order in either crystalline or non-crystalline phases is an essential feature for optimal polymer conductivity. For this reason, several techniques have been employed for the investigation of molecular order and molecular orientation in polymeric thin films[17,18], aiming at studying their impact on device performances and also at learning how to control them by tuning the molecular design and the deposition conditions.

The most common technique is GI-XRD (Grazing Incidence X-Ray diffraction), a very informative technique but limited to the investigation of crystalline regions[19,20], which is often not sufficient especially for studying low-crystallinity block copolymers. Hence, optical polarizing spectroscopies are occasionally used as they probe the average orientational order of the whole film[21,16]. In this case Variable-angle spectroscopic ellipsometry (VASE) and near-edge X-ray absorption (NEXAFS) are usually used jointly to achieve a full description of the average molecular orientation, since the first gives information about the orientation of the polymer backbone while the latter probes the orientational order of the π-conjugated plane.

Magnetic resonance spectroscopies are far less popular compared to XRD and optical spectroscopies for this application. Recently, solid state NMR spectroscopy in conjunction with computational methods was used to predict a variety of molecular ordering properties in a polythienothiophene film, such as the average backbone conformation, the degree of π-stacking and the ordering of the side chains[22,23]. Despite this rich information content, solid state NMR is usually unfit for the investigation of thin film samples, due to sensitivity issues.

On the other hand, EPR spectroscopy is particularly suited to the study of the average molecular orientation, relying on the anisotropy of magnetic interactions in paramagnetic species, such as the Zeeman interaction and the dipolar interaction, that dominate the spin-Hamiltonian (and therefore the EPR spectra) of polymer polarons and photoexcited triplet states respectively. EPR allows to determine the average orientation of the magnetic tensors relative to the substrate, and consequently - if the tensors can be assigned to the molecule - it leads to a full description of the average molecular orientation. The degree of order can also be determined from spectral simulations using an appropriate orientational distribution function. Like optical spectroscopies and opposite to XRD, EPR probes the orientational order of the entire sample, including both crystalline and non-crystalline regions.

This Chapter will show how we used EPR to study the average molecular orientation and the degree of orientational order in the films of two low-bandgap conjugated polymers. In order to highlight the effect of the deposition method on the molecular order inside the film, we studied two different films for each polymer, obtained *via* drop-casting and spin-coating.

The analysis was carried out using the photoexcited triplet state of the polymers as the probe of molecular order, that was investigated by Time Resolved EPR (TR-EPR). Although examples of both the use of polymer polarons[24,25] and triplet states[26,27] for similar EPR investigations are known in literature, we chose to use the triplet state of the polymers because of the larger anisotropy of the Zero-field splitting (ZFS) interaction compared to the Zeeman interaction, leading to a higher resolution of the EPR transitions corresponding to different molecular orientations in the triplet state spectrum with respect to the spectrum of the polymer radical. This ensures a higher accuracy of the orientational analysis.

The study was carried out in two steps. The first one was the determination of the ZFS tensor orientation in the molecular frame. Indeed, this knowledge is necessary to deduce the molecular orientation inside the films from the second step of the investigation, in which the average ZFS tensor orientation in the polymer films is determined.

Unlike previous EPR studies, we stressed the importance of the first step, i.e. an accurate assignment of the magnetic tensor to the molecular frame, for achieving a reliable description of molecular orientation in the sample. We showed that DFT calculations and the study of the polymers in liquid crystal matrices can be used to gain this knowledge.

The Chapter will first introduce the studied polymers and the theoretical basis for the orientational analysis *via* EPR. The presentation of the results will follow, starting from the assignment of the ZFS tensor and proceeding with the study of the polymer films.

3.1 Materials

The materials chosen for the investigation are two representative polymers belonging to the class of the low-bandgap conjugated polymers for BHJSCs[28], namely PSiF-DBT (poly-silafluorene-benzothiadiazole) and PBDT-BT-BTA (poly-benzodithiophene-benzothiadiazole-benzotriazole), shown in Figure 3.1. In these polymers, donor and acceptor groups are simultaneously present in the monomeric units to reduce the bandgap and consequently widen the absorption spectrum towards the infrared region.

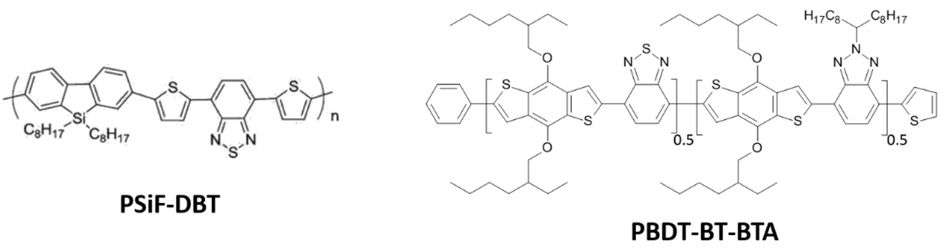

Figure 3.1 Chemical structures of the polymers.

The PSiF-DBT monomer alternates a silafluorene unit (SiF), as the electron-rich portion, and a dithienyl-benzothiadiazole electron-poor unit (DBT), resulting in a low bandgap of 1.82 eV[29,30]. The low energy HOMO (-5.39 eV) justifies the high V_{oc} value of 0.9V that was reported for devices based on the polymer blend with PCBM, and it is expected to ensure a better air-stability compared to other polymers like the benchmark P3HT (having HOMO with energy -5 eV). Solar cells based on PSiF-DBT also showed a good short-circuit current (9.5 mA/cm^2) and a PCE of 5.4%[30].
This polymer is very similar to PCDTBT, where a carbazole unit takes the place of the silafluorene one. PCDTBT was for a long time classified as a disordered polymer, as GIXRD studies showed very poor diffractions from its spin-coated films[31,32]. However, EPR on the triplet state of the drop-cast polymer recently showed a high degree of order[27]. Such controversial evidences can be explained with the difference in the phases probed by the two techniques: EPR probes both crystalline and amorphous regions, where significant average order may also occur, and therefore it should be coupled with XRD to achieve a more complete description of the molecular arrangement and order. We chose to apply EPR to the very similar but less studied PSiF-DBT and to investigate both drop-cast and spin-coated films to highlight any effect of the deposition technique.

The PBDT-BT-BTA polymer is composed of two different acceptor moieties, the benzothiadiazole (BT) and the benzotriazole (BTA), that are randomly alternated to the benzodithiophene (BDT) donor unit. While BDT and BT groups are quite common in the design of low bandgap copolymers, the use of benzotriazole is less diffuse[28,33]. Although it is a weaker acceptor compared to BT[34], BTA is among the few electron-accepting moieties that can incorporate alkyl substituents, combining the electron-withdrawing role with the improved solution processability of the resulting polymers.

The bandgap of PBDT-BT-BTA was reported to be 1.8 eV, leading to a broad absorption in the visible range between 400 and 750 nm[35]. A promising PCE of 5% was found by Kotowski et al.[35] for this polymer blended with $PC_{71}BM$, that was shown to be more than three times higher compared to the analogous polymer having regular alternation of the BT and BTA acceptor units. Therefore, the random alternation of building blocks seems to be a promising characteristic, that may spread-up in the field of molecular design of semiconducting polymers, as it is very convenient for the industrial scale-up of the production, since it implies a much easier synthesis compared to the regular alternating polymers[36].

The absence of morphological studies on this copolymer encouraged our EPR investigation.

3.2 Theoretical background

3.2.1 EPR lineshape and molecular orientation

The study of molecular orientation through EPR is possible because EPR spectra depend on the orientation of the paramagnetic species inside the magnetic field of the spectrometer.

As reported in Chapter 2, in the case of a triplet state species, the spin Hamiltonian describing the system can be written as:

$$\hat{\mathrm{H}} = \mu_{\mathrm{B}} \cdot \hat{\boldsymbol{S}} \cdot \overline{\overline{\boldsymbol{g}}} \cdot \vec{B}_0 + \hat{\boldsymbol{S}} \cdot \overline{\overline{\boldsymbol{D}}} \cdot \hat{\boldsymbol{S}} \qquad \text{Eq. 3.1}$$

where μ_{B} indicates the Bohr magneton, $\vec{\boldsymbol{B}}_{\mathbf{0}}$ is the static magnetic field vector, $\overline{\overline{\boldsymbol{D}}}$ is the ZFS tensor and $\hat{\boldsymbol{S}}$ the total spin operator. The eigenfunctions of the Hamiltonian in Eq. 3.1 are field-dependent linear combinations of the ZFS eigenstates (approaching high-field limit eigenstates for strong $\vec{\boldsymbol{B}}_{\mathbf{0}}$ fields), and their relative populations can be derived from the zero-field ones using the same coefficients. Furthermore, the energy of the states depends on the orientation of the molecule in the magnetic field. For each orientation two transitions are in general allowed ($\Delta M_s = \pm 1$) and their splitting in terms of resonance field (for isotropic g factor) is given by:

$$\Delta B(\theta, \varphi) = \frac{1}{g\mu_B}\left[D(3\ \cos\theta^2 - 1) + 3E\sin\theta^2\cos 2\varphi\right]^{1/2} \qquad \text{Eq. 3.2}$$

where θ and φ are the azimuthal and polar angles that describe the orientation of $\vec{\boldsymbol{B}}_{\mathbf{0}}$ in the principal axes system of the $\overline{\overline{\boldsymbol{D}}}$ tensor, while D and E are the parameters that fully describe the ZFS tensor (see Chapter 2). In randomly oriented samples all molecular orientations are equally probable, resulting in a wide spectrum that is independent on the orientation of the sample in the magnetic field ("powder spectrum”). The EPR intensity of powder spectra at each field position can be calculated by integrating over all possible orientations according to Eq. 3.3[37,38]:

$$I(B) = \sum_{\pm} \iint G(B - B_{res\pm}(\theta,\varphi)) \cdot p_{\pm}(B,\theta,\varphi) \cdot \sin(\theta)\, d\theta d\varphi \qquad \text{Eq. 3.3}$$

Here the summation is over the two transitions ($\Delta M_s = \pm 1$) and $G(B - B_{res\pm}(\theta,\varphi))$ is a Gaussian lineshape function centered at the resonance field $B_{res\pm}(\theta,\varphi)$, while $p_{\pm}(B,\theta,\varphi)$ is the population difference between the two triplet sublevels involved in the $\Delta M_s = \pm 1$ transitions, which determines the transition probability.

Triplet state powder spectra are highly informative because they show ‘turning points’ at the resonant field values $B_{\mathrm{res}}(\theta = 0)$, B_{res} $(\theta = 90\ ,\ \varphi = 0)$, B_{res} $(\theta = 90,\ \varphi = 90)$, i.e. for those molecular orientations in which the principal $\overline{\overline{\boldsymbol{D}}}$ axes are parallel to $\vec{\boldsymbol{B}}_{\mathbf{0}}$. Considering that the spacing between these peaks is related to the $\overline{\overline{\boldsymbol{D}}}$ tensor according to Eq. 3.2, the powder spectrum can be used to easily derive the D and E parameters.

In samples with some degree of molecular order the EPR spectrum deviates from the powder spectrum because the molecular orientations are not equally distributed. In other words, there is a non-uniform distribution of molecular orientations, $P(\theta,\varphi)$, that must be taken into account to reproduce the spectral shape. Indeed, the contribution of each orientation to the spectrum is weighted by the value of the distribution function:

$$I(B) = \sum_{\pm} \iint G(B - B_{res\pm}(\theta,\varphi)) \cdot p_{\pm}(B,\theta,\varphi) \cdot P(\theta,\varphi) \cdot sin(\theta)\, d\theta d\varphi \qquad \text{Eq. 3.4}$$

In this case the spectrum depends on the orientation of the sample inside the magnetic field and this dependence can be exploited to derive the molecular orientational order inside the sample, as will become clearer in the next sections.

3.2.2 Modelling orientational order

To understand molecular order from the analysis of triplet state EPR spectra, an appropriate orientational distribution function must be introduced and used to calculate the spectra according to Eq. 3.4, in order to reproduce the experimental spectra.

In this study we analyzed two kinds of partially oriented samples: the oriented liquid crystal matrices in which the polymers were dissolved, that were used for the assignment of the ZFS tensor to the molecular frame, and the films of the polymers.

For the liquid crystal samples, we chose a nematic liquid crystal (E7) that was oriented using the magnetic field of the spectrometer. The nematic phase is a uniaxial phase (i.e. a phase with cylindrical symmetry) in which the liquid crystal (LC) molecules are preferentially aligned with their symmetry axis along one direction, that is called the *nematic director*. As will be shown in section 3.3.1, polymer solute molecules in a nematic phase behave like if they were cylindrically symmetric molecules (i.e. molecules with an axially symmetric interaction with the LC molecules). Therefore, their orientation in the nematic is described by only one angle which is the angle θ between the symmetry axis of the phase (the nematic director, $\hat{\boldsymbol{n}}$) and the pseudo symmetry axis of the solute molecules, that will be referred to as *molecular orienting axis* or *molecular director* ($\hat{\boldsymbol{k}}_{\boldsymbol{mol}}$). In this situation the orientational distribution function is uniaxial, i.e. it is a function of only one angle.

The orientational distribution function $P(\theta)$ is defined as a probability density, so that the probability P that the molecule is oriented between the angles θ_1 and θ_2 from the director is given by:

$$\mathrm{P} = \int_{\theta_1}^{\theta_2} \int_0^{2\pi} P(\theta)\ sen(\theta) d\theta d\varphi \qquad \text{Eq. 3.5}$$

where the normalization condition imposes:

$$\int_0^{\pi} \int_0^{2\pi} P(\theta)\ sen(\theta) d\theta d\varphi = 1 \qquad \text{Eq. 3.6}$$

When dealing with uniaxial solute molecules dissolved in nematic LCs, the orientational distribution function derived from Maier-Saupe theory for uniaxial molecules in uniaxial nematics is usually used to model the orientational order of the solute[37,39].

According to this theory the dissolved molecules are subjected to an orienting potential $\mathrm{U}(\theta)$ that can be expressed as:

$$\mathrm{U}(\theta) = -\varepsilon \cdot \mathrm{P}_2(\cos\theta) \qquad \text{Eq. 3.7}$$

where $\mathrm{P}_2(\cos\theta)$ is the second Legendre polynomial: $(3\cos^2\theta - 1)/2$. In principle, the orienting potential can be expressed as a summation over L polynomials $\mathrm{P}_\mathrm{L}(\cos\theta)$. Due to the form of the polynomials, only even terms should be included since the terms with odd L have opposite signs for θ and $\theta \pm \pi$, while the orientational distribution should be invariant. We considered the simplest form of $\mathrm{U}(\theta)$, which is truncated at the first even term of the summation, i.e. L=2.

The ε parameter has energy dimension and it is related to the anisotropy in the molecular polarizability of the solute molecule. It measures the strength of the orienting potential and therefore determines the width of the orientational distribution function.

In thermal equilibrium conditions the orientational distribution function can be derived according to the Boltzmann distribution as $P(\theta) = \frac{1}{Q} e^{-U(\theta)/kT}$:

$$P(\theta) = \frac{1}{Q} \cdot \exp \frac{\varepsilon}{2kT}(3\cos^2\theta - 1) \qquad \text{Eq. 3.8}$$

where Q is the orientational partition function:

$$Q = \int_0^{\pi} \int_0^{2\pi} e^{-U(\theta)/kT} \operatorname{sen}(\theta) d\theta d\varphi \qquad \text{Eq. 3.9}$$

As shown by Luckhurst[40] the ε parameter is proportional to the nematic-isotropic transition temperature T_{NI}. We can define a new ε' parameter as $\varepsilon' = \varepsilon / kT$, which is a dimensionless parameter that depends on the reduced temperature T/T_{NI}. Thus Eq. 3.8 can be written as:

$$P(\theta) = \frac{1}{Q} \cdot e^{\varepsilon\prime(3\cos^2\theta - 1)} \qquad \text{Eq. 3.10}$$

The order parameter is defined as the ensemble average of the $P_2(\cos\theta)$ polynomial:

$$S = \langle P_2(\cos\theta) \rangle = \frac{1}{Q} \cdot \int_0^{\pi} \int_0^{2\pi} P_2(\cos\theta)\, P(\theta) \operatorname{sen}(\theta) d\theta d\varphi \qquad \text{Eq. 3.11}$$

so it is also dependent on the reduced temperature T/T_{NI}. S ranges from -0.5 to 1, corresponding to the situations of perfect order in which the molecular director is respectively perpendicular ($\theta = 90°$) or parallel ($\theta = 0°$) to the nematic director for 100% of the molecules. S is zero for a completely disordered sample since the integral in Eq. 3.11 vanishes for a constant $P(\theta)$.

Figure 3.2 shows the shape of the orientational distribution function in Eq. 3.10 for different values of ε' and the dependency of the order parameter on ε'.

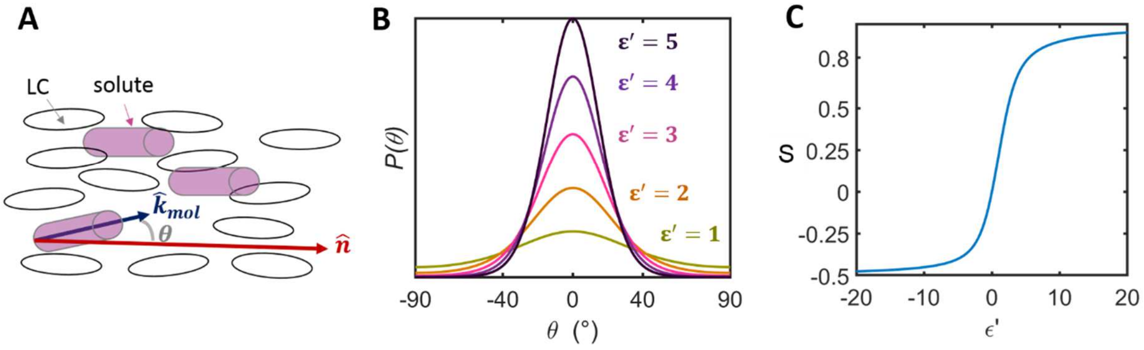

Figure 3.2 A: Schematic representation of the orientation of uniaxial molecules in a uniaxial nematic LC; B: Orientational distribution function for variable ε'; C: Order parameter as a function of ε'.

The orientational distribution function described by Eq. 3.10 for uniaxial molecules in uniaxial nematics could be adapted also to the description of the orientational order in the polymer films. Indeed, we experimentally verified that the films are uniaxial phases in terms of molecular ordering, since there is no preferential order inside the film plane, meaning that the films are symmetrical with respect to the normal to the substrate. Furthermore, the satisfying simulations of the spectra of the film samples, based on the use of Eq. 3.10, confirmed that the polymer molecules behave like uniaxial molecules also in this case. The validity of the choice of a uniaxial distribution function is also confirmed by previous EPR studies, where similar distributions were adopted[24,26,27].

Considering the symmetry of the films with respect to the normal to the plane, this axis was chosen as director ($\hat{\boldsymbol{n}}$). Therefore, in this case the angle θ in the orientational distribution is the angle between the normal to the film plane and a molecular orienting axis ($\hat{\boldsymbol{k}}_{\boldsymbol{mol}}$).

Clearly in this case, once the film is formed, the order is not determined by thermodynamics, thus ε' should be only considered as a phenomenological parameter, independent on temperature over a large T range.

The orientational distribution function described so far was used to calculate the triplet state EPR spectra of the polymers in order to simulate the experimental spectra of the partially ordered samples. The only variable parameters in the simulation were ε', which defines the width of the orientational distribution function, and the coordinates of the molecular orienting axis $\hat{\boldsymbol{k}}_{\boldsymbol{mol}}$. All the parameters characterizing the spin system, i.e. $\overline{\overline{\boldsymbol{g}}}$ and $\overline{\overline{\boldsymbol{D}}}$ tensors, triplet sublevels populations, linewidth, were kept fixed to the values determined from the simulations of spectra of isotropic samples of the same polymers (consisting in the isotropic LC and the *bulk* films of the polymers, i.e. films obtained through evaporation of the solvent inside the EPR tube).

In this way, the value of ε' and the coordinates of $\hat{\boldsymbol{k}}_{\boldsymbol{mol}}$ in the ZFS principal axes reference system were obtained from the simulations. From ε', the order parameter S, expressing the degree of orientational order in the sample, could be readily calculated using Eq. 3.11. The coordinates of $\hat{\boldsymbol{k}}_{\boldsymbol{mol}}$ revealed what is the average preferred orientation of the ZFS tensor with respect to the director (see Figure 3.3). Thus, to infer the orientation of the molecule in the film samples, it was necessary to determine the orientation of the ZFS tensor in the molecular frame, which is the reason why liquid crystalline matrices were used.

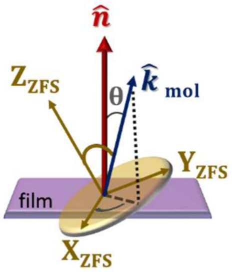

Figure 3.3 Scheme for the description of molecular orientation inside the films.

To summarize, in the present study we adopted the following method: 1) we assigned the ZFS tensor of the polymers to the molecular frame, as described in section 3.3.1 2) we acquired and simulated the EPR spectra of completely disordered film samples of the polymers (*bulk* films), to determine the ZFS tensor parameters, the triplet populations and the linewidths (section 3.3.2) ; 3) we performed EPR on the spin-coated and drop-casted films and simulated the spectra using the orientational distribution function in Eq. 3.10 (section 3.4). The molecular orientation was then derived by comparison of the results obtained for the films with the assignment of the magnetic tensors to the polymer molecule.

3.3 Assignment of the ZFS tensor to the molecular frame

In order to determine the orientation of the ZFS tensor in the molecular frame of the polymers we used both experimental and computational methods, as described in the following sections.

3.3.1 Alignment of the polymers in the nematic LC

In principle, the assignment of the ZFS tensor to the molecular reference system could be done by performing EPR experiments on single crystals. By orienting the crystal in the magnetic field of the spectrometer and by exploring many orientations, the principal axes of the tensor can be determined. In our case, the lack of polymers single crystals ruled out this possibility. However, other partially ordered phases, with known orientation of the polymer molecules, can be used, such as nematic liquid crystalline matrices[41,42]. Indeed, following the predictions of Onsager's theory[43] for the orientation of rod-shaped molecules in nematic phases, it is generally accepted that conjugated polymer molecules tend to align their backbone to the nematic director of the liquid crystal. This was demonstrated in past studies, performed with polarized fluorescence spectroscopy, on the MEH-PPV polymer (metoxy-ethylhexyloxy-*p*-phenylenevinylene) dissolved in the nematic liquid crystal known as *5CB* (4-cyano-4-pentylbiphenyl)[44,45]. Thanks to the anisotropic solvation interactions, the polymer was found to be highly oriented with the backbone parallel to the director.

For our study we chose the *E7* liquid crystal, a mixture of cyano-biphenyls and triphenyls shown in Figure 3.4, having a nematic-isotropic transition temperature (T_{NI}) of 333 K[46].

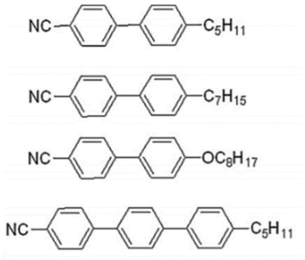

Figure 3.4 Components of the E7 liquid crystal mixture.

In order to obtain an oriented matrix of the polymers dissolved in the LC, the nematic phase was oriented using the magnetic field of the spectrometer, exploiting the anisotropy of the magnetic susceptibility ($\bar{\bar{\boldsymbol{\chi}}}$) of the LC molecules, which is the tensorial physical quantity determining the magnetization ($\vec{\boldsymbol{M}}$) induced in the system by the application of a magnetic field ($\vec{\boldsymbol{B}}_{\boldsymbol{0}}$):

$$\vec{\boldsymbol{M}} = \bar{\bar{\boldsymbol{\chi}}} \cdot \vec{\boldsymbol{B}}_{\boldsymbol{0}} \qquad \text{Eq. 3.12}$$

In case of axially-symmetric molecules, the $\bar{\bar{\boldsymbol{\chi}}}$ tensor has axial symmetry and the magnetic anisotropy $\Delta\chi$ is defined as the difference between its principal values:

$$\Delta\chi = \chi_{||} - \chi_{\perp} \qquad \text{Eq. 3.13}$$

where $\chi_{||}$ and $\chi_{\perp}$ correspond to the principal axes that are respectively parallel and perpendicular to the symmetry axis. The sign of the magnetic anisotropy determines the kind of alignment of the nematic LC in the applied magnetic field. For positive $\Delta\chi$ the nematic director tends to be parallel to the magnetic field. This is also the case of E7 molecules.

The aligned nematic phase obtained by the application of the magnetic field was cooled-down to 130 K inside the resonator, in order to obtain a frozen polycrystalline phase (E7 melting point is 210 K) preserving the nematic alignment, which allowed to vary the sample orientation in the magnetic field while retaining the original orientation of the nematic director. In this way we could detect TR-EPR triplet spectra of the polymers with different orientations of the nematic director in the magnetic field. It was also necessary to acquire the spectra in the isotropic liquid crystal phase, to allow to characterize the triplet states of the polymers in the E7 solvent, without any ordering effect. Indeed, as described in the previous section, the interpretation of the spectra of the oriented phases requires the knowledge of the ZFS parameters that can be derived from the analysis of isotropic samples. For this reason, the isotropic phase was studied by heating the samples over the T_{NI} temperature and freezing them in liquid N_2 before insertion into the cooled (130 K) EPR resonator.

The spectra of the frozen isotropic and nematic phases of the polymers solutions in E7 are reported in Figure 3.5.

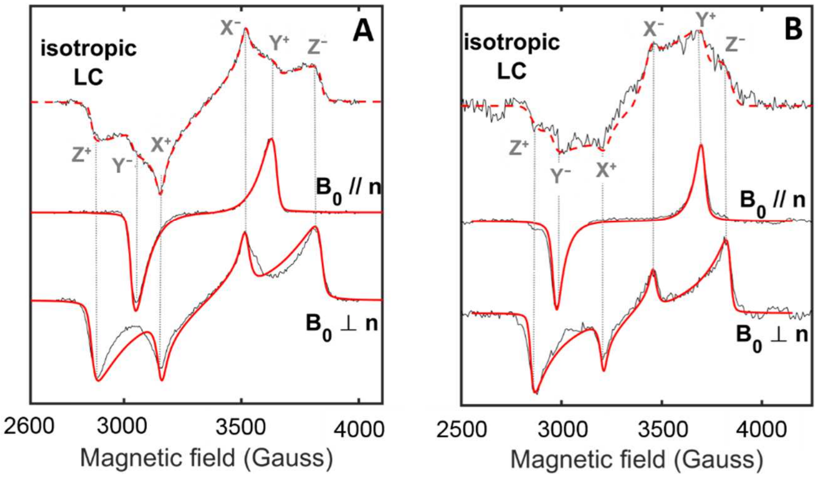

Figure 3.5 TR-EPR spectra of the PSiF-DBT (A) and the PBDT-BT-BTA (E7) polymers dissolved in the E7 liquid crystal, in the frozen isotropic and nematic phases. The spectra of the frozen nematics were acquired with the magnetic field (**B_0**) parallel or perpendicular to the nematic director (**n**). Red lines are spectral simulations.

From the simulation of the isotropic phase spectra, the triplet sublevels zero-field populations and the ZFS parameters were determined (see Table 3.1). These parameters were used to simulate the spectra of the oriented nematic phases using the orientational distribution function in Eq. 3.10. However, even a simple inspection of the spectra reveals that a high degree of molecular orientation is present in the nematic phases, since only one triplet component, corresponding to the Y_{ZFS} direction of the dipolar tensor, is detected when the magnetic field is parallel to the nematic director, while both the X_{ZFS} and Z_{ZFS} components are recorded when the field is perpendicular to the nematic director. This corresponds to the uniaxial ordering of the polymer molecules inside the aligned nematic phases. Indeed, the spectra were well fitted by the uniaxial orientational distribution function, with Y_{ZFS} as the molecular orienting axis ($\hat{\boldsymbol{k}}_{mol}$) preferentially aligned to the nematic director. Therefore, we assigned this direction to the polymers backbones.

The order parameters derived from the simulations are 0.70-and 0.88 for the PSiF-DBT and the PBDT-BT-BTA respectively, corresponding to ~50% and 80% of molecules oriented within ±20° from the nematic director respectively. This difference in the ordering of the two polymers might be related to the linearity of the backbone: in contrast to PSiF-DBT, the PBDT-BT-BTA polymer has a linear backbone that likely helps the ordering in the nematic.

Table 3.1 ZFS tensor parameters and zero-field populations of the polymers triplet state in E7 solution. The polymers molecular axes ($\hat{\boldsymbol{k}}_{\boldsymbol{mol}}$) aligned to the nematic director are also indicated, with the relative order parameter (S).

Polymer	D (G)	E (G)	P_X:P_Y:P_Z	$\hat{\boldsymbol{k}}_{\boldsymbol{mol}}$	S
PSiF-DBT	490	43	0.57:0.43:0	Y_{ZFS}	0.70 ± 0.05
PBDT-BT-BTA	495	87	0.48:0.52:0	Y_{ZFS}	0.88 ± 0.02

By comparing the D value of the polymers in the liquid crystal (Table 3.1) with the value of a small aromatic molecule such as pentacene[47] ($D = 495$ G), and considering the dimension of the monomeric unit of our polymers, we can infer that the triplet delocalization in the polymers does not exceed one monomer. Therefore, the high orientational order found for the triplet wavefunction in the frozen nematic, suggests that the polymers have an elongated conformation inside the nematic liquid crystal, in which the majority of the monomeric units are approximately aligned. This agrees with past predictions on the MEH-PPV polymer on the basis of optical measurements and calculations[45].

Besides revealing the collocation of the backbone direction in the ZFS principal axes frame, our results confirm the tendency of conjugated polymers to form highly oriented phases in liquid crystals. This could be explored as a strategy to produce orientationally ordered polymeric materials.

3.3.2 Magnetophotoselection

The photoexcited triplet state wavefunction of conjugated polymers can slightly depend on the polymer phase, for instance it is usually slightly different between solutions and films, and this affects the ZFS tensor parameters and populations, hence it is evident from the TR-EPR triplet spectra.

In this case we observed that the ZFS parameters characterizing the triplet state of the polymers in the liquid crystal, as determined from the isotropic LC samples (see Table 3.1), were to some extent different from the triplet state parameters in the polymers bulk films, that are reported in Table 3.2.

Table 3.2 ZFS parameters and zero-field populations of the polymers triplet states in the bulk films.

Polymer	D (G)	E (G)	P_X:P_Y:P_Z
PSiF-DBT	445	40	0.26:0.74:0
PBDT-BT-BTA	435	65	0.34:0.66:0

These discrepancies reflect slightly different triplet wavefunctions and they are likely due to a difference in the polymers conformation between the liquid crystal matrix and the bulk films. In principle, this may result also in a different orientation of the ZFS principal axes in the molecular frame. Such observation casted some doubts on the possibility of transferring the information on the ZFS tensor orientation obtained from the liquid crystalline phase to the films in which we want to determine the molecular order. For this reason, we used the bulk films to perform an experiment which provides analogous results compared to the LC experiments, namely magnetophotoselection. Indeed, magnetophotoselection experiments allow to identify the relative orientation of the dipolar tensor and the optical transition dipole moment, which for conjugated polymers in the visible region typically coincides with the backbone direction[48,49].

Magnetophotoselection arises in solid samples where the paramagnetic photoexcited species are formed upon illumination with linearly polarized light, like the laser beam that is used in TR-EPR[50]. To observe magnetophotoselection it is necessary that no depolarizing phenomena are active in the sample, like light scattering or energy transfer between molecules. If this condition is satisfied, the molecules inside the sample are selectively excited with a probability that is proportional to the square cosine of the angle between the transition dipole moment and the light electric field vector $\vec{E}(t)$. When this phenomenon is coupled with magnetic resonance of the photoselected species - characterized by anisotropic spin interactions - the resulting spectrum deviates from the powder spectrum due to the preferential orientation of the formed paramagnetic species, with a higher number of species oriented with the transition dipole moment parallel to the applied electric field $\vec{E}(t)$. If the electric field is parallel to the static magnetic field of the spectrometer ($\vec{B}_0$), the molecules oriented with the transition dipole moment parallel to $\vec{B}_0$ will be selected, causing the enhancement of the contribution of this orientation to the EPR spectrum. Conversely, if $\vec{E}(t)$ is perpendicular to $\vec{B}_0$, the orientations corresponding to the transition dipole perpendicular to $\vec{B}_0$ will be enhanced, resulting in higher contribution to the spectrum (magnetophotoselection). In triplet state spectra the result is that the triplet dipolar tensor direction corresponding to the transition dipole moment will contribute more to the spectrum acquired with $\vec{E}(t)||\vec{B}_0$, while the perpendicular directions will be enhanced with $\vec{E}(t)\perp\vec{B}_0$.

We performed magnetophotoselection experiments on the polymers bulk films by changing the direction of $\vec{E}(t)$ with respect to $\vec{B}_0$. This caused the enhancement of the Y transition in the $\vec{E}(t)||\vec{B}_0$ case, and the enhancement of the Z transition in the $\vec{E}(t)\perp\vec{B}_0$ case (Figure 3.6), which indicates that the Y_{ZFS} axis of the triplet coincides with the direction of the transition dipole moment and therefore with the polymer backbone.

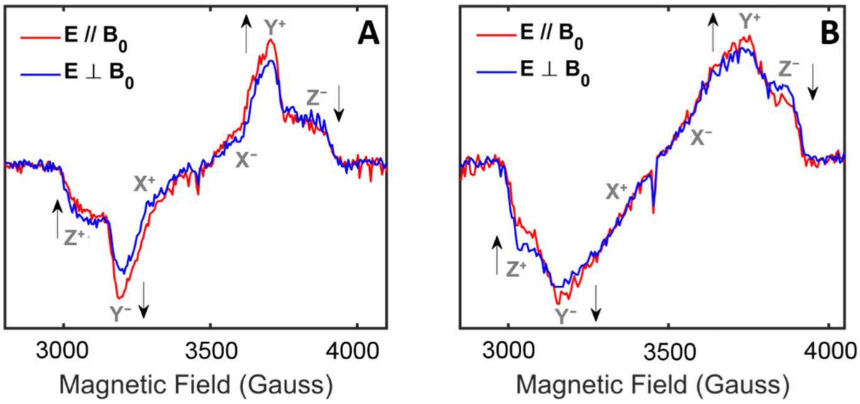

Figure 3.6 Magnetophotoselection TR-EPR spectra of PSiF-DBT (A) and PBDT-BT-BTA (B) bulk films (λ = 532 nm).

The result of magnetophotoselection confirms the assignment of the backbone proposed on the basis of the experiments on the LC polymer phases, and proves that the triplet wavefunction in the LC is not much different from the films, at least for the Y_{ZFS} direction, that coincides with the backbone in both cases.

3.3.3 Calculation of the ZFS tensor

So far, we determined the ZFS principal direction coinciding with the polymers backbones. However, a complete assignment of the ZFS tensor is needed for our scopes. Therefore, we used computational methods to calculate the zero-field splitting interaction in the first excited triplet state of the polymers.

Due to computational constraints we performed the calculations on the monomers. However, this choice seems to be appropriate since the experimental D values suggest that the triplet wavefunction is approximately localized on one monomer (see previous section). Two monomers were considered for the PBDT-BT-BTA copolymer, one containing the BT unit as acceptor and the other containing the BTA unit.

Geometry optimizations of the monomers in their triplet states were carried out in Gaussian[51] using the B3LYP/6-31G(d) DFT method. The aliphatic substituents were approximated as methyl groups. Two different methods for the calculation of the ZFS tensor were tried.

The first method relies on the point-dipole approximation for the calculation of the dipolar interaction[52]. In this case the electron densities were considered as centered at the atoms positions and the dipolar interaction was weighted using the Mulliken spin-populations of the triplet wavefunction, that was calculated in Gaussian at the B3LYP/6-311G(d) DFT level. This method was used quite often in EPR studies to provide insights into the ZFS tensor of aromatic molecules and fullerenes[52,53,54], although it is known to usually overestimate the tensor principal values. In our case it produced D and E parameters largely deviating from the experimental results, on the scale of one order of magnitude.

The second approach is based on the use of the ORCA program[55], in which algorithms for the calculation of the spin-spin contribution to the dipolar interaction are included[56]. This method requires as input the spin-density matrix of the triplet state under investigation, which was calculated in ORCA using DFT with the B3LYP functional combined with the EPR-II basis set for H-C-N-O atoms and the def2-TZVPP basis set for S atoms. This approach was found to give satisfactory predictions of the ZFS principal values for small aromatic molecules in the triplet state, despite the calculation of the triplet wavefunction neglecting configuration interaction[56,54]. For our monomers it led to D and E values that are smaller compared to the experimental ones by almost a factor of 3. However, the calculated Y_{ZFS} principal axis roughly coincided with the polymer backbone as verified experimentally in the previous sections. Therefore, we can trust the validity of the calculation, at least for the orientation of the principal axes. For all monomers the (X_{ZFS} Y_{ZFS}) plane was predicted to correspond to the aromatic plane, as shown in Figure 3.7.

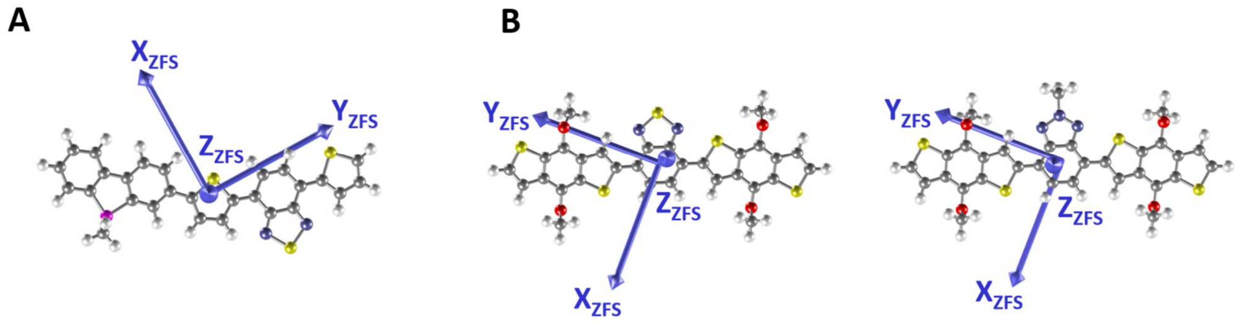

Figure 3.7 ZFS tensor principal directions derived by DFT calculations on the monomers of PSiF-DBT (A) and PBDT-BT-BTA (B).

3.4 Molecular order analysis on the spin-coated and drop-cast films

The TR-EPR triplet state spectra of the PSiF-DBT and the PBDT-BT-BTA polymers in spin-coated (SC) and drop-cast (DC) films showed a remarkable dependence on the sample orientation in the spectrometer magnetic field. This demonstrates the existence of molecular order inside the films.

In Figure 3.8 the spectra recorded on the PSiF-DBT films are shown. The samples were rotated using a goniometer (with 3° sensitivity) so that the magnetic field was alternatively parallel and perpendicular to the film plane.

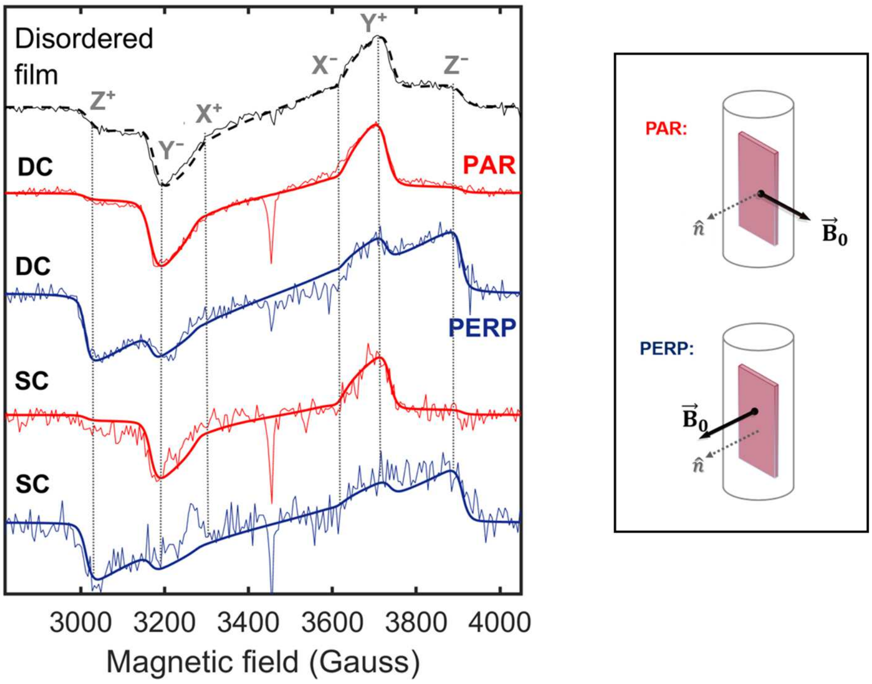

Figure 3.8 TR-EPR spectra (T = 80 K) of the PSiF-DBT films with variable orientation in the magnetic field ($\vec{B}_0$). PAR= $\vec{B}_0$ parallel to the film plane, PERP= $\vec{B}_0$ perpendicular to the film plane. SC= spin-coated films, DC= drop-cast films. Disordered film = bulk film. Thick lines are simulations.

For the simulations of the spectra in DC and SC films, the spin-system parameters that were determined from the simulation of the disordered film spectrum (i.e. the bulk film deposited on the inner walls of the EPR tube by solvent evaporation) were assumed (reported in Table 3.2).

By looking at the spectra of the drop-cast and spin-coated films it can be noticed that they are very similar and that in both cases the main difference between the two orientations of the film in the magnetic field ($\vec{B}_0$) consists in the intensity ratio between the Z and the Y transitions. Indeed, the Z/Y intensity ratio is smaller in the spectrum recorded with the field parallel to the film plane and larger when the field is perpendicular to the film plane. In the parallel and perpendicular field orientations, the Z/Y ratio is also respectively smaller and larger compared to the isotropic film spectrum. This may arise from two possible average uniaxial molecular orientations: one in which the Y_{ZFS} axis is mostly parallel to the substrate and the other in which Z_{ZFS} is mostly perpendicular to the substrate, as both these orientations would have the same effect on the Z/Y ratio in the TR-EPR spectra. However, the discrimination between the two situations comes from the evaluation of the intensity of the X transition as well. In the case of Y_{ZFS} laying in the film plane, the Z/Y and the X/Y ratios are larger when $\vec{B}_0$ is normal to the film, however, the Z/X ratio should be invariant on field orientation and equal to the value it has in the isotropic film spectrum. On the other hand, if Z_{ZFS} is perpendicular to the film, the Z/X ratio should increase in the spectrum recorded with $\vec{B}_0$ perpendicular to the film. In the recorded spectra, the Z/X intensity ratio increases for $\vec{B}_0$ perpendicular to the film, therefore this hypothesis seems to be the correct one.

This interpretation was confirmed by the spectral simulations that were successfully obtained using the uniaxial model described in section 3.2.2, in which the Z_{ZFS} axis was considered as the molecular orienting axis ($\hat{\boldsymbol{k}}_{\boldsymbol{mol}}$) preferentially aligned to the director ($\hat{\boldsymbol{n}}$, chosen normal to the film plane). The reliability of the simulations was assured by the fact that both spectral orientations were simulated by a unique set of parameters. Other attempts of simulating the spectra, considering the Y_{ZFS} as the molecular orienting axis laying in the film plane, were not satisfactory.

The presence of a molecular axis which is predominantly perpendicular to the substrate implies the existence of an average orientational order of the molecular plane in the film. Since Z_{ZFS} is preferentially normal to the film plane, the (X_{ZFS} Y_{ZFS}) plane lays parallel to the substrate.

No significant differences between the DC and SC films of the PSiF-DBT were found from the simulations, that revealed the same kind of order and also the same order parameter for the two deposition methods (see Table 3.3).

The spectra recoded on the PBDT-BT-BTA polymer films are reported in Figure 3.9.

The drop-cast film spectra show a sharp predominance of the Z transitions in the direction normal to the film plane, with indiscernible contributions of the other triplet transitions, while the X and Y transitions dominate the spectrum acquired with $\vec{B}_0$ parallel to the plane. These observations rule out the hypothesis of a molecular orientation characterized by the Y_{ZFS} axis laying in the film plane, since it would imply a Z/X ratio equal to the value of the isotropic film in all field orientations, while we found that the X component is completely missing in the spectrum with $\vec{B}_0$ perpendicular to the plane. This spectral shape is only reproduced considering the Z_{ZFS} axis strongly aligned to the film normal, as confirmed by the spectral simulations. Therefore, the analysis of the TR-EPR spectra revealed that also for this polymer the (X_{ZFS} Y_{ZFS}) plane is mainly parallel to the substrate.

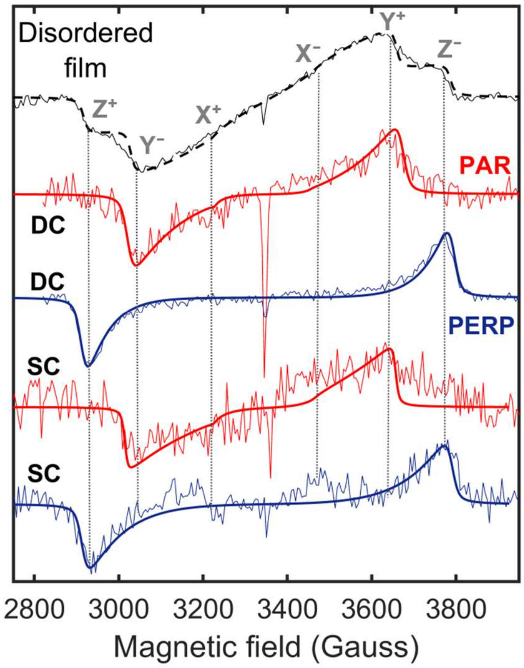

Figure 3.9 TR-EPR spectra (T = 80 K) of the PBDT-BT-BTA films with variable orientation in the magnetic field (B_0). PAR= B_0 parallel to the film plane, PERP= B_0 perpendicular to the film plane. SC= spin-coated films, DC= drop-cast films. Disordered film = bulk film. Thick lines are simulations.

The spectra of the spin-coated film have a lower signal-to-noise ratio, due to the smaller thickness of the films, resulting in a lower amount of material in the resonator. However, their shape is comparable to that of the drop-cast film, suggesting the same kind of molecular orientation. The order parameters determined for DC and SC films of the PBDT-BT-BTA polymer are reported in Table 3.3, showing that the difference between the two depositions is inside the experimental error.

Table 3.3 Parameters describing the molecular orientational order in the film samples, as obtained from the spectral simulations.

Polymer	**Film sample**	$\hat{\boldsymbol{k}}_{\boldsymbol{mol}}$	**S**
PSiF-DBT	Drop-cast	Z_{ZFS}	0.31 ± 0.02
	Spin-coated	Z_{ZFS}	0.31 ± 0.02
PBDT-BT-BTA	Drop-cast	Z_{ZFS}	0.82 ± 0.04
	Spin-coated	Z_{ZFS}	0.79 ± 0.08

These results show that for both polymers there is no appreciable difference in terms of molecular orientation between the static deposition, i.e. drop-casting, and the spin-coating deposition. Therefore, we deduced that the spin-coating deposition in the particular conditions of this study (3000 rpm, see the Experimental section for details), does not influence the ordering of the polymer on the substrate.

The assignment of the ZFS tensor reported in section 3.3 showed that the Z_{ZFS} axis is perpendicular to the aromatic plane of the polymers, while Y_{ZFS} coincides with the backbone. By combining this information with the above results on molecular ordering in the films, showing that the (X_{ZFS} Y_{ZFS}) plane is preferentially parallel to the substrates, we deduced that the polymer molecules in the films are mainly oriented with their backbones in the plane and they also lay with the aromatic plane parallel to the substrate, in the so-called *face-on* orientation (Figure 3.10A).

The acquisition of TR-EPR spectra of the films with the magnetic field parallel to the substrate but in the direction normal to the one already explored, allowed to verify that the spectra with $\vec{B}_0$ spanning different directions inside the film plane are superimposable. This proved that there is no preferential order inside the plane of the films, confirming the uniaxiality of the molecular orientational order. Therefore, our analysis showed that the films contain stacked polymer molecules with face-on arrangement but with random orientation of the backbone direction inside the film plane (Figure 3.10B).

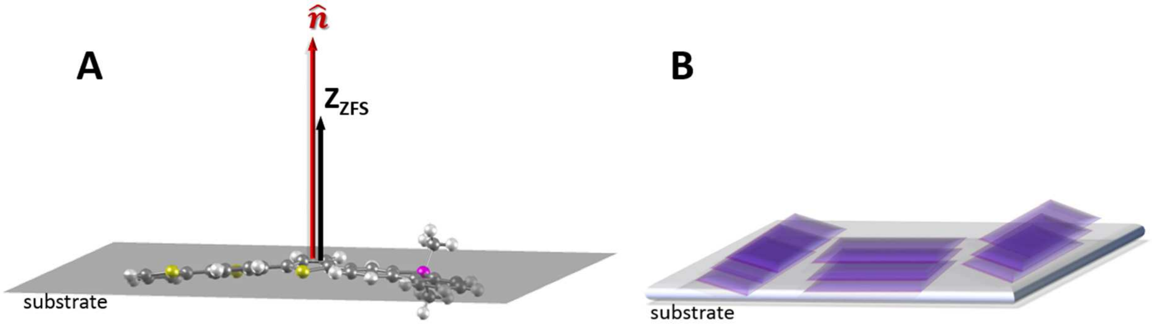

Figure 3.10 Representation of the face-on orientation of polymer molecules; B: Representation of the arrangement of polymer stacks, having random orientation of the backbone inside the plane of the film.

The order parameters reported in Table 3.3 reveal that the PBDT-BT-BTA polymer forms films with a much higher degree of order compared to PSiF-DBT. To the best of our knowledge, no XRD studies on the PBDT-BT-BTA were published yet. However, our results suggest it tends to form highly ordered structures, with a specific favored orientation of the molecular plane with respect to the substrate. This feature foreshadows good charge transport properties for this polymer as it is probably related to a fair polymer crystallinity with ordered crystallite growth and/or to a high degree of orientational order in the non-crystalline phase. The preferential orientation of the aromatic plane in the film is expected to provide directionality to charge transport, which enhances the charge collection efficiency at the electrodes of the photovoltaic devices.

The smaller order displayed by PSiF-DBT is in line with the XRD studies on the very similar polymer PCDTBT (where a carbazole unit takes the place of the silafluorene unit), showing very low crystallinity of the films. However, EPR shows that small molecular order occurs also in the non-crystalline domains of the PSiF-DBT polymer.

3.5 Conclusions

In this Chapter we showed how EPR spectroscopy can be used to probe molecular order in conjugated polymer films for photovoltaic applications, exploiting the anisotropy of the ZFS interaction in the photoexcited triplet state of the polymers. This method is expected to be particularly relevant for the investigation of molecular ordering features in films of low-bandgap conjugated copolymers, that have been extensively shown to possess low-crystallinity but consistent order in the non-crystalline phase, which is not accessible through XRD techniques. For these polymers, EPR is expected to be especially useful since it probes the average molecular order of the sample, including crystalline and amorphous domains, leading to the evaluation of the average degree of order inside the films.

The use of EPR for this kind of investigation requires the assignment of the ZFS tensor to the polymer molecular frame, that can be achieved by the interplay of EPR experiments and calculations. It was shown that the polymers dissolved in a nematic liquid crystal, properly oriented in the magnetic field of the spectrometer, are highly oriented with their backbone parallel to the nematic director and assume an elongated conformation. This allowed to experimentally determine the coordinates of the polymer backbone in the ZFS tensor principal axes system, that were confirmed by magnetophotoselection experiments on disordered films of the same polymers. The experimental data on the orientation of the polymers backbones in the ZFS reference system were used to confirm the validity of the DFT calculations of the polymers ZFS tensors, that provided the full determination of the tensors orientation in the molecular frame.

The analysis of the TR-EPR spectra of the PSiF-DBT and the PBDT-BT-BTA polymers in spin-coated and drop-cast films, detected with variable orientation of the film planes in the spectrometer magnetic field, was successfully carried out assuming a uniaxial orientational order. The results of the simulations, combined with the knowledge of the ZFS tensor assignment, revealed that the polymers backbones tend to lay in the film plane for all investigated films, and that the aromatic plane of the polymers is preferentially oriented parallel to the substrate (*face-on* configuration).

The comparison between the results for drop-cast and spin-coated films lead to no detectable differences in terms of molecular orientational order. This suggests that the mechanical spinning action of the spin-coating deposition has no considerable effect on the average ordering of polymer chains, that remains unaltered with respect to the static deposition. This conclusion is restricted to the specific spin-coating deposition conditions that were used (see Experimental section), since we did not explore the effect of their variation on the resulting molecular order. However, the choice of the deposition parameters was in line with the commonly adopted spin-coating conditions for the production of conjugated polymer films, which points to a generalization of our result. Although spin-coating is the most common technique for the preparation of conjugated polymer films for research scopes, the breakthrough in the production of these films, that paves the way to their commercialization, is represented by the large-area roll-to-roll printing techniques[57]. Therefore, it would be interesting to investigate if and how these techniques allow to control molecular order.

The PBDT-BT-BTA polymer films were found to have a very high degree of order. Although EPR cannot discern between molecular order due to the ordered growth of polymer crystallites or to the presence of ordered domains in non-crystalline regions, it predicts a particular tendency of this polymer to form highly ordered structures. This suggests that the high number of aliphatic side chains of this polymer, that are bound to both electron-donor and electron-acceptor units, does not hamper molecular packing and ordering. Therefore, the use of electron-accepting units that can bear aliphatic substituents, like benzotriazole, seems to be a good strategy allowing to improve the solubility and hence the processability of the polymers without ruining their molecular packing. Furthermore, the results on PBDT-BT-BTA show that the random alternation of accepting units in the polymer backbone is compatible with the formation of well-ordered films, which supports the convenience of this simplified synthetic strategy.

3.6 Experimental

3.6.1 Materials

The ODCB solvent for the preparation of the film samples was purchased from Sigma-Aldrich. The E7 liquid crystal was purchased from Merck.

The PSiF-DBT polymer (Mw 10-80 kDa) was purchased from Sigma-Aldrich. The PBDT-BT-BTA polymer (Mw 61 kDa, PDI 3) was synthesized as described in ref.[35].

3.6.2 Samples preparation

For the preparation of the liquid crystalline solutions of the polymers, a small quantity of PSiF-DBT and PBDT-BTD-BTA, lower than 1 mg, was dissolved in 1 ml of the E7 liquid crystal upon few hours of heating and sonication. Then 200 μL of the solutions were put in EPR quartz tubes and sealed under vacuum after few freeze-pump-thaw cycles in order to eliminate dissolved oxygen. The isotropic phase of the samples was obtained by heating the tubes above the nematic-isotropic transition temperature of 333 K and freezing them in liquid N_2 before insertion into the cooled (130 K) EPR resonator. The nematic liquid crystalline phase was aligned at room temperature by applying a 0.6 T magnetic field to the sample in the resonator of the EPR spectrometer for few minutes. Without changing the orientation of the EPR tube, the resonator was then cooled to 130 K.

The disordered films of the polymers were obtained in the EPR tubes (3 mm ID, 4 mm OD) by solvent evaporation under vacuum from the ODCB solutions of the polymers, having 1 mg/mL concentrations. More concentrated solutions were employed for spin-coating and drop-casting depositions, namely 10 mg/ml for PSiFDBT and 5 mg/ml for PBDT-BTD-BTA. The solutions were deposited on glass substrates (Brand microscope cover glass 18x18x0.15 mm) previously cleaned by sonicating in an isopropyl alcohol bath first, and finally in acetone.

Spin-coating was performed using a SCS G3P-8 machine and depositing the solution (~100 μL) on the substrate at rest. The spinning procedure was composed of two steps, each of which consisting of a first phase where the angular velocity was linearly increased with time and a second that maintained a constant velocity. In order to reduce the amount of solution ejected from the substrate, the velocity of the first step was kept lower compared to the second step, where an acceleration was imposed to favor solvent evaporation (1000 rpm were used for the first step and 3000 rpm for the second). The total spinning time was around 2 minutes. Drop-cast films were obtained by depositing ~80 μL of solution on the substrates and leaving them drying in air.

The resulting films were cut into 18x2 mm slices that were put parallel to each other in the EPR quartz tubes (4 mm OD, 3 mm ID). The tubes were degassed using a vacuum line (10^{-3} Torr) and then sealed under a N_2 atmosphere to ensure good thermal contact between the tube walls and the inside. All the orientational measurements were performed by attaching a goniometer to the sample tube, enabling for a ±3° precision.

3.6.3 EPR spectroscopy

TR-EPR experiments were performed on two different spectrometers. For the experiments on the LC matrices, an X-band ER200D Bruker spectrometer was used, equipped with a cylindrical cavity and a nitrogen-flow variable-temperature system (Bruker BVT200), providing a minimum temperature of 130K. The photoexcitation was obtained from a Nd:YAG pulsed laser (Quantel Brilliant, pulse length = 5 ns; E/pulse = ca. 5 mJ; repetition rate 50 Hz), equipped with a second-order harmonic generator (λ = 532 nm). The signal was obtained without field modulation and by recording the microwave diode output (after a 10 MHz bandwidth preamplifier) with a LeCroy digital oscilloscope triggered by the laser pulse. The spectra were acquired at 25 dB microwave power attenuation (0.6 mW nominal power), with 256 field points and 500 averages per point.

The films spectra were acquired on an X-band ELEXSYS E580 spectrometer, equipped with a dielectric resonator inside an Oxford CF900 cryostat. Liquid N_2 was used to keep the samples at the temperature of 80 K. A Nd:YAG pulsed laser (Quantel Brilliant, pulse length = 5 ns; E/pulse = ca. 5 mJ; repetition rate 10 Hz) was used as source of photoexcitation (λ = 532 nm). The spectra were acquired at 25 dB microwave power attenuation (0.6 mW nominal power), with 256 field points and 300 averages per point.

Spectral simulations of disordered samples (films deposited in the EPR tubes, isotropic liquid crystalline phase) were obtained using the Matlab toolbox Easyspin[58]. Spectral data of partially oriented systems (frozen nematic phases, drop-cast and spin-coated films) were instead simulated using a home-made program implemented in Matlab, that diagonalizes the spin Hamiltonian and then calculates the spectrum by considering a large number of molecular orientations, each of which is weighted by the value of the orientational distribution function as described in section 3.2.1.

3.7 References

(1) Kline, R. J.; McGehee, M. D.; Toney, M. F. Highly Oriented Crystals at the Buried Interface in Polythiophene Thin-Film Transistors. *Nat. Mater.* **2006**, *5*, 222–228.

(2) Chirvase, D.; Parisi, J.; Hummelen, J. C.; Dyakonov, V. Influence of Nanomorphology on the Photovoltaic Action of Polymer – Fullerene Composites. *Nanotechnology* **2004**, *15*, 1317–1323.

(3) Li, G.; Shrotriya, V.; Huang, J.; Yao, Y.; Moriarty, T.; Emery, K.; Yang, Y. High-Efficiency Solution Processable Polymer Photovoltaic Cells by Self-Organization of Polymer Blends. *Nat. Mater.* **2005**, *4*, 864–868.

(4) Kim, Y.; Cook, S.; Tuladhar, S. M.; Choulis, S. a.; Nelson, J.; Durrant, J. R.; Bradley, D. D. C.; Giles, M.; McCulloch, I.; Ha, C.-S.; et al. A Strong Regioregularity Effect in Self-Organizing Conjugated Polymer Films and High-Efficiency Polythiophene:fullerene Solar Cells. *Nat. Mater.* **2006**, *5*, 197–203.

(5) Keivanidis, P. E.; Clarke, T. M.; Lilliu, S.; Agostinelli, T.; Macdonald, J. E.; Durrant, J. R.; Bradley, D. D. C.; Nelson, J. Dependence of Charge Separation Efficiency on Film Microstructure in Poly(3-Hexylthiophene-2,5-diyl):[6,6]-Phenyl-C61 Butyric Acid Methyl Ester Blend Films. *J. Phys. Chem. Lett.* **2010**, *1*, 734–738.

(6) Chen, D.; Nakahara, A.; Wei, D.; Nordlund, D.; Russell, T. P. P3HT/PCBM Bulk Heterojunction Organic Photovoltaics: Correlating Efficiency and Morphology. *Nano Lett.* **2011**, *11*, 561–567.

(7) Brabec, C. J.; Heeney, M.; McCulloch, I.; Nelson, J. Influence of Blend Microstructure on Bulk Heterojunction Organic Photovoltaic Performance. *Chem. Soc. Rev.* **2011**, *40*, 1185–1199.

(8) Noriega, R.; Rivnay, J.; Vandewal, K.; Koch, F. P. V; Stingelin, N.; Smith, P.; Toney, M. F.; Salleo, A. A General Relationship between Disorder, Aggregation and Charge Transport in Conjugated Polymers. *Nat. Mater.* **2013**, *12*.

(9) Beaujuge, P. M.; Fréchet, J. M. J. Molecular Design and Ordering Effects in π-Functional Materials for Transistor and Solar Cell Applications. *JACS* **2011**, *133*, 20009–20029.

(10) Liu, Y.; Zhao, J.; Li, Z.; Mu, C.; Ma, W.; Hu, H.; Jiang, K.; Lin, H. Aggregation and Morphology Control Enables Multiple Cases of High-Efficiency Polymer Solar Cells. *Nat. Commun.* **2014**, *5*, 1–8.

(11) Jackson, N. E.; Savoie, B. M.; Marks, T. J.; Chen, L. X.; Ratner, M. A. The Next Breakthrough for Organic Photovoltaics? *J. Phys. Chem. Lett.* **2015**, *6*, 77–84.

(12) Salleo, B. A.; Kline, R. J.; Delongchamp, D. M.; Chabinyc, M. L. Microstructural Characterization and Charge Transport in Thin Films of Conjugated Polymers. *Adv. Mater.* **2010**, *22*, 3812–3838.

(13) Sirringhaus, H.; Brown, P. J.; Friend, R. H.; Nielsen, M. M.; Bechgaard, K.; Langeveld-Voss, B. M. W.; Spiering, a. J. H.; Janssen, R. a. J.; Meijer, E. W.; Herwig, P.; et al. Two-Dimensional Charge Transport in Self-Organized, High-Mobility Conjugated Polymers. *Nature* **1999**, *401*, 685–688.

(14) Steyrleuthner, R.; Pietro, R. Di; Collins, B. A.; Polzer, F.; Himmelberger, S.; Schubert, M.; Chen, Z.; Zhang, S.; Salleo, A.; Ade, H.; et al. The Role of Regioregularity, Crystallinity, and Chain Orientation on Electron Transport in a High-Mobility N-Type Copolymer. *JACS* **2014**, *136*, 4245–4256.

(15) Vohra, V.; Kawashima, K.; Kakara, T.; Koganezawa, T.; Osaka, I.; Takimiya, K.; Murata, H. Efficient Inverted Polymer Solar Cells Employing Favourable Molecular Orientation. *Nat. Photonics* **2015**, *9*, 1–5.

(16) Zhang, X.; Bronstein, H.; Kronemeijer, A. J.; Smith, J.; Kim, Y.; Kline, R. J.; Richter, L. J.; Anthopoulos, T. D.; Sirringhaus, H.; Song, K.; et al. Molecular Origin of High Field-Effect Mobility in an Indacenodithiophene-Benzothiadiazole Copolymer. *Nat. Commun.* **2013**, *4*, 1–9.

(17) Huang, Y.; Kramer, E. J.; Heeger, A. J.; Bazan, G. C. Bulk Heterojunction Solar Cells: Morphology and Performance Relationships. *Chem. Rev.* **2014**, *114*, 7006–7043.

(18) Giridharagopal, R.; Ginger, D. S. Characterizing Morphology in Bulk Heterojunction Organic Photovoltaic Systems. *J. Phys. Chem. Lett.* **2010**, *1*, 1160–1169.

(19) Baker, J. L.; Jimison, L. H.; Mannsfeld, S.; Volkman, S.; Yin, S.; Subramanian, V.; Salleo, A.; Alivisatos, A. P.; Toney, M. F.; Science, M.; et al. Quantification of Thin Film Crystallographic Orientation Using X-Ray Diffraction with an Area Detector. *Langmuir* **2010**, *26*, 9146–9151.

(20) Chiu, M.; Jeng, U.; Su, M.; Wei, K. Morphologies of Self-Organizing Regioregular Conjugated Polymer / Fullerene Aggregates in Thin Film Solar Cells. *Macromolecules* **2010**, *43*, 428–432.

(21) Gurau, M. C.; Delongchamp, D. M.; Vogel, B. M.; Lin, E. K.; Fischer, D. A.; Sambasivan, S.; Richter, L. J. Measuring Molecular Order in Poly (3-Alkylthiophene) Thin Films with Polarizing Spectroscopies. *Langmuir* **2007**, *23*, 834–842.

(22) Cochran, J. E.; Junk, M. J. N.; Glaudell, A. M.; Miller, P. L.; Cowart, J. S.; Toney, M. F.; Hawker, C. J.; Chmelka, B. F.; Chabinyc, M. L. Molecular Interactions and Ordering in Electrically Doped Polymers: Blends of PBTTT and F4TCNQ. *Macromolecules* **2014**, *47*, 6836–6846.

(23) Melnyk, A.; Junk, M. J. N.; Mcgehee, M. D.; Chmelka, B. F.; Hansen, M. R.; Andrienko, D. Macroscopic Structural Compositions of π-Conjugated Polymers: Combined Insights from Solid-State NMR and Molecular Dynamics Simulations. *J. Phys. Chem. Lett.* **2017**, *8*, 4155–4160.

(24) Aguirre, A.; Gast, P.; Orlinskii, S.; Akimoto, I.; Groenen, E. J. J.; El Mkami, H.; Goovaerts, E.; Van Doorslaer, S. Multifrequency EPR Analysis of the Positive Polaron in I_2-Doped poly(3-Hexylthiophene) and in poly[2-Methoxy-5-(3,7-Dimethyloctyloxy)]-1,4-Phenylenevinylene. *Phys. Chem. Chem. Phys.* **2008**, *10*, 7129–7138.

(25) Konkin, a.; Roth, H. K.; Scharff, P.; Aganov, a.; Ambacher, O.; Sensfuss, S. K-Band ESR Studies of Structural Anisotropy in P3HT and P3HT/PCBM Blend Polymer Solid Films: Paramagnetic Defects after Continuous Wave Xe-Lamp Photolysis. *Solid State Commun.* **2009**, *149*, 893–897.

(26) Cambré, S.; De Ceuster, J.; Goovaerts, E.; Bouwen, A.; Detert, H. Quantitative Evaluation of the Preferential Orientation of Para-Phenylene Vinylene Pentamers in Polystyrene Films by Optically Detected Magnetic Resonance. *Appl. Magn. Reson.* **2007**, *31*, 343–355.

(27) Biskup, T.; Sommer, M.; Rein, S.; Meyer, D. L.; Kohlstädt, M.; Würfel, U.; Weber, S. Ordering of PCDTBT Revealed by Time-Resolved Electron Paramagnetic Resonance Spectroscopy of its Triplet Excitons. *Angew. Chemie Int. Ed.* **2015**, *54*, 7707–7710.

(28) Liu, C.; Wang, K.; Heeger, A. J. Low Bandgap Semiconducting Polymers for Polymeric Photovoltaics. *Chem. Soc. Rev.* **2016**, *45*, 4825–4846.

(29) Boudreault, P. T.; Michaud, A.; Leclerc, M. A New Poly (2 ,7-Dibenzosilole) Derivative in Polymer Solar Cells. *Macromol. Rapid Commun.* **2007**, No. 28, 2176–2179.

(30) Wang, E.; Wang, L.; Lan, L.; Luo, C.; Zhuang, W. High-Performance Polymer Heterojunction Solar Cells of a Polysilafluorene Derivative. *Appl. Phys. Lett.* **2008**, *92*, 5–7.

(31) Beiley, Z. M.; Hoke, E. T.; Noriega, R.; Dacuña, J.; Burkhard, G. F.; Bartelt, J. A.; Salleo, A.; Toney, M. F.; Mcgehee, M. D. Morphology-Dependent Trap Formation in High Performance Polymer Bulk Heterojunction Solar Cells. *Adv. Energy Mater.* **2011**, *1*, 954–962.

(32) Lu, X.; Hlaing, H.; Germack, D. S.; Peet, J.; Jo, W. H.; Andrienko, D.; Kremer, K.; Ocko, B. M. Bilayer Order in a Polycarbazole-Conjugated Polymer. *Nat. Commun.* **2012**, *3*, 1–7.

(33) Lu, L.; Zheng, T.; Wu, Q.; Schneider, A. M.; Zhao, D.; Yu, L. Recent Advances in Bulk Heterojunction Polymer Solar Cells. *Chem. Rev.* **2015**, *115*, 12666–12731.

(34) Patel, D. G. D.; Feng, F.; Ohnishi, Y.; Abboud, K. A.; Hirata, S.; Schanze, K. S.; Reynolds, J. R. It Takes More Than an Imine: The Role of the Central Atom on the Electron-Accepting Ability of Benzotriazole and Benzothiadiazole Oligomers. *J. Am. Chem. Soc.* **2012**, *134*, 2599–2612.

(35) Kotowski, D.; Luzzati, S.; Bianchi, G.; Calabrese, A. Double Acceptor D-A Copolymers Containing Benzotriazole and Benzothiadiazole Units: Chemical Tailoring towards Efficient Photovoltaic Properties. *J. Mater. Chem. A* **2013**, *1*, 10736–10744.

(36) Bonoldi, L.; Calabrese, A.; Pellegrino, A.; Perin, N.; Po, R.; Spera, S.; Tacca, A. Optical and Electronic Properties of Fluorene/Thiophene/Benzothiadiazole Pseudorandom Copolymers for Photovoltaic Applications. *J. Mater. Sci.* **2011**, *46*, 3960–3968.

(37) Segre, U.; Pasimeni, L.; Ruzzi, M. Simulation of EPR and Time Resolved EPR Lineshapes in Partially Ordered Glasses. *Spectrochim. Acta - Part A Mol. Biomol. Spectrosc.* **2000**, *56*, 265–271.

(38) Barbon, A.; Bortolus, M.; Maniero, A. L.; Brustolon, M. Structure and Dynamics of the Triplet State of Oligothiophenes in Isotropic and Partially Oriented Matrices. *Phys. Chem. Chem. Phys.* **2005**, 7, 2894–2899.

(39) Maier, W.; Saupe, A. Eine Einfache Molekulare Theorie Des Nematischen Kristallinflüssigen Zustandes. *Zeitschrift für Naturforsch. A* **1958**, *13*, 564–566.

(40) Dunmur, D.; Fukuda, A.; Luckhurst, G. *Physical Properties of Liquid Crystals: Nematics*; INSPEC, The Institution of Electrical Engineers: London, United Kingdom, 2001.

(41) Bortolus, M.; Ferrarini, A.; Tol, J. Van; Maniero, A. L. Full Determination of Zero Field Splitting Tensor of the Excited Triplet State of C60 Derivatives of Arbitrary Symmetry from High Field TREPR in Liquid Crystals. *J. Phys. Chem. B* **2006**, *110*, 3220–3224.

(42) Ceola, S.; Corvaja, C.; Franco, L. The Orientation of the Principal Axes of the Electron Dipolar Interaction Tensor in Triplet State C60 Monoadducts. *Mol. Cryst. Liq. Cryst.* **2003**, 31–43.

(43) Onsager, L. The Effects of Shapes on the Interaction of Colloidal Particles. *Ann. N. Y. Acad. Sci.* **1949**, *51*, 627–659.

(44) Fritz, K. P.; Scholes, G. D. Alignment of Conjugated Polymers in a Nematic Liquid-Crystal Host. *J Phys Chem B* **2003**, *107*, 10141–10147.

(45) Barbara, P. F.; Chang, W.; Link, S.; Scholes, G. D.; Yethiraj, A. Structure and Dynamics of Conjugated Polymers in Liquid Crystalline Solvents. *Annu. Rev. Phys. Chem.* **2007**, 58, 565–584.

(46) Michaeli, S.; Soffer, S.; Levanon, H.; Senge, M. O.; Kalisch, W. W. Triplet Dynamics of Conformationally Distorted Porphyrins in Isotropic Liquids and Liquid Crystals. Time-Resolved Electron Paramagnetic Resonance Study. **1999**, *103*, 1950–1957.

(47) Montalti, M.; Credi, A.; Prodi, L.; Gandolfi, M. T. *Handbook of Photochemistry*, 3rd ed.; CRC Press, Boca Raton, 2006.

(48) Lammi, R. K.; Fritz, K. P.; Scholes, G. D.; Barbara, P. F. Ordering of Single Conjugated Polymers in a Nematic Liquid Crystal Host. *J. Phys. Chem. B* **2004**, No. 108, 4593–4596.

(49) Hammond, M. R.; Kline, R. J.; Herzing, A. A.; Richter, L. J.; Germack, D. S.; Ro, H.; Soles, C. L.; Fischer, D. A.; Xu, T.; Yu, L.; et al. Molecular Order in High-Efficiency Polymer/Fullerene Bulk Heterojunction Solar Cells. *ACS Nano* **2011**, No. 10, 8248–8257.

(50) El-Sayed, M. A.; Siegel, S. Method of "Magnetophotoselection" of the Lowest Excited Triplet State of Aromatic Molecules. *J. Chem. Phys.* **1966**, *44*, 1416–1423.

(51) Frisch, M. J.; Trucks, G. W.; Schlegel, H. B.; Scuseria, G. E.; Robb, M. A.; Cheeseman, J. R.; Scalmani, G.; Barone, V.; Mennucci, B.; Petersson, G. A.; et al. Gaussian 09, Revision B.01. *Gaussian 09, Revision B.01, Gaussian, Inc., Wallingford CT.* 2009.

(52) Visser, J.; Groenen, E. J. J. The Fine-Structure in the Lowest Triplet State of C60 and C70. *Chem. Phys. Lett.* **2002**, *356*, 43–48.

(53) Toffoletti, A.; Wang, Z.; Zhao, J.; Tommasini, M.; Barbon, A. Precise Determination of the Orientation of the Transition Dipole Moment in a Bodipy Derivative by Analysis of the Magnetophotoselection Effect. *Phys. Chem. Chem. Phys.* **2018**, *20*, 20497–20503.

(54) Tait, C. E.; Neuhaus, P.; Anderson, H. L.; Timmel, C. R. Triplet State Delocalization in a Conjugated Porphyrin Dimer Probed by Transient Electron Paramagnetic Resonance Techniques. *J. Am. Chem. Soc.* **2015**, *137*, 6670–6679.

(55) Neese, F. The ORCA Program System. *WIREs Comput Mol Sci* **2012**, *2*, 73–78.

(56) Sinnecker, S.; Neese, F. Spin - Spin Contributions to the Zero-Field Splitting Tensor in Organic Triplets, Carbenes and Biradicals: a Density Functional and Ab Initio Study. *J. Phys. Chem. A* **2006**, *110*, 12267–12275.

(57) Krebs, F. C.; Søndergaard, R. R.; Markus, H. Roll-to-Roll Fabrication of Large Area Functional Organic Materials. *J. Polym. Sci. Part B Polym. Phys.* **2013**, *51*, 16–34.

(58) Stoll, S.; Schweiger, A. EasySpin, a Comprehensive Software Package for Spectral Simulation and Analysis in EPR. *J. Magn. Reson.* **2006**, *178*, 42–55.

CHAPTER 4. ALL-POLYMER BLENDS

Recently, the paradigm of polymer/fullerene photoactive layers for bulk heterojunction solar cells became less strong as research on non-fullerene polymer acceptors made consistent progresses. Such an interest was spurred by the intrinsic shortcomings of fullerene materials such as the limited optical absorption, the poor bandgap tunability due to the small effects of chemical derivatizations, the high costs of synthesis and extensive purifications, and the lack of morphological stability[1].

A lot of small molecular acceptors were developed, having the advantage of an easier synthesis and easier tunability of the electronic properties. The most common building blocks were naphthalene diimide (NDI) or perylene diimide (PDI), benzothiadiazole (BT) and indacenodithiophene (IDT), that could reach up to 13% PCEs [1–5].

A second category of fullerene alternatives is represented by n-type conjugated polymers to be used in *all-polymer* blends, that add other benefits to those offered by small molecular acceptors, namely the high extinction coefficients, improved mechanical properties of the resulting films i.e. strength and flexibility[6], and the flexibility in tuning the solution viscosity, which is an important feature for the industrial scale-up of the solution-processed modules[7]. So far, two main kinds of architectures for n-type polymers were explored, namely cyano-polyphenylenevinylenes and NDI/PDI-based polymers, with the latter achieving the best performances[6,7,8,9].

Recently, a new kind of architecture was proposed by Beaujuge et al.[10,11] based on the electron deficient thieno-[3,3-c]pyrrole-4,6-dione (TPD) and the 3,4-difluorothiophene ([2F]T) units. These two building blocks were shown to lead to increased electron affinity compared to NDI/PDI-based polymers.

In this Chapter, the EPR study on two all-polymer blends, containing two polymer acceptors synthesized by Beaujuge's group[11], will be presented. The study is the result of a collaboration with the groups of Prof. Beaujuge (who provided the materials) and Prof. Laquai (who coordinated the optical spectroscopy characterizations) in KAUST (King Abdullah University of Science and Technology).

The acceptor polymers, abbreviated as P2TPD-[2F]T and P2TPD-BT-[2F]T, are based on the TPD-[2F]T unit bound to a second TPD block. In the more complex polymer a BT (benzothiadiazole) unit was also introduced (Figure 4.1), which lowered the bandgap from 1.9 eV to 1.7 eV, extending the optical absorption to longer wavelengths (Figure 4.2). The two polymers were blended with the PBDT-TS1 donor, a polymer of recent synthesis, having a very small bandgap (1.57 eV), that was chosen as one of the best-performing donor polymers so far, reaching over 9% PCEs in blends with $PC_{71}BM$[12,13,14]. The good complementarity in the optical absorption of the two counterparts provided a wide spectral absorption in the visible range (Figure 4.2).

Solar cells made from spin-coated solutions of these donor/acceptor blends in 1:2 weight ratio showed promising efficiencies, namely 2.4% for the P2TPD-[2F]T blend and 4.6% for the P2TPD-BT-[2F]T blend[11].

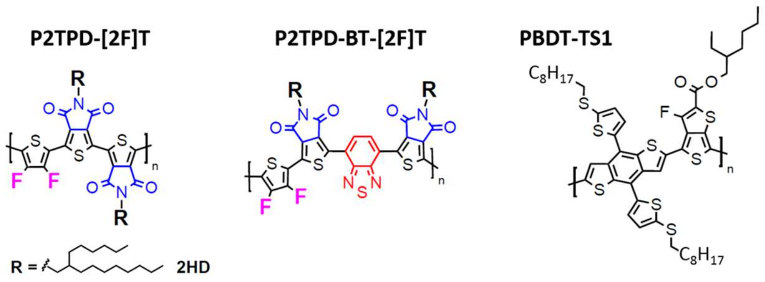

Figure 4.1 Chemical structures of the polymers.

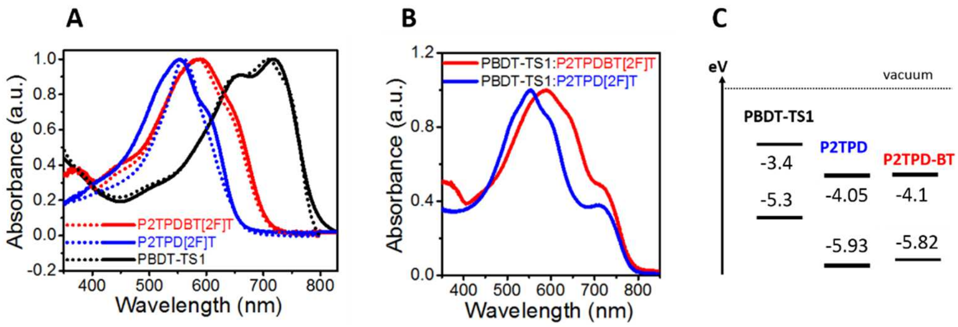

Figure 4.2 A: absorption spectra of the polymers in solution in chlorobenzene (dotted lines) and in spin-coated films (solid lines), taken from ref.[11] ; B: absorption spectra of the donor/acceptor spin-coated films, taken from ref. [11]; C: energy levels diagram where lower levels indicate the ionization potentials derived from photoelectron spectroscopy experiments, and upper levels indicate electron affinities determined from cyclic voltammetry in ref.[11].

The aim of the EPR study was to provide insights in the photophysical processes occurring in the two blends, with the attempt of assessing the reasons of their different photovoltaic performance.

Furthermore, the ability of EPR spectroscopy to unravel also morphological features of the materials encouraged the investigation.

The results will be organized as follows: the characterization of the pristine materials will be presented first, followed by the study of the D/A blend films obtained from the solutions by solvent evaporation inside the EPR tube. These films will be referred to as ‘bulk films’ and are used to achieve preliminary information about the photophysics of the blends as well as on the characteristics of the photogenerated species, avoiding molecular ordering effects. Secondly, the spin-coated thin films of the blends will be examined as the spin-coating provides more controlled film morphology and it is indeed the currently used technique for the deposition of the active layer for building the photovoltaic devices on a laboratory scale.

4.1 Pristine polymers

The neat polymers were examined individually in order to characterize their pristine paramagnetic species.

For the acceptor polymers, no EPR signal could be detected in the frozen solutions, neither in dark nor under light-illumination. On the other hand, the donor polymer PBDT-TS1 in frozen oDCB solution showed an intense signal in dark that was only slightly increased upon illumination (Figure 4.3). This is the common observation for p-type conjugated polymers that are processed in air, as they are easily oxidized by O_2 [15,16]. Thus, the dark signal can be attributed to the donor radical cation generated by air oxidation, while the photoinduced effect can be ascribed to additional light-promoted oxidation by O_2 or solvent molecules. From the spectral simulation the g-tensor of the PBDT-TS1 radical cation was obtained (g_1= 2.0040 g_2=2.0031 g_3=2.0022).

The absence of an EPR signal of the acceptor polymers was expected based on their very high oxidation potential, that inhibits oxidation by O_2, and also considering that no reducing agents are present in the system to cause the reduction of the polymers.

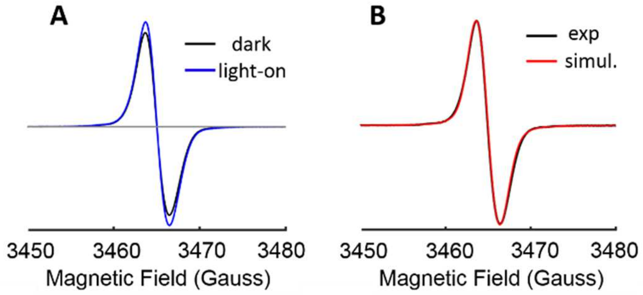

Figure 4.3 A: dark and light-on CW spectra (80K) of PBDT-TS1 in ODCB; B: simulation of the spectrum.

Bulk films of the individual polymers gave same results and are not reported as they don't add any other information.

The above experiments showed that the donor polymer contains pristine radicals while the acceptors do not, and allowed to identify the donor radical cation g-factor. We then wanted to characterize the spectral features of the excited triplet states of the polymers, since they are involved in the photophysical processes occurring in the photoactive blends. The TR-EPR spectra extracted at 0.5 µs from laser excitation are reported in Figure 4.4 along with the simulations.

The spectral shape is substantially different between the frozen solutions and the bulk films in terms of the relative intensity of the triplet transitions, indeed, the Z transition is more intense in the film samples and the spectrum could not be reproduced as an ISC-populated triplet state spectrum. Similar observations in literature were explained as the effect of an orientational order inside the films, causing a preferential orientation of the triplet Z axis in the direction of the magnetic field[17]. However, it is hard to believe that such a kind of molecular order can exist in a sample in which the polymer is deposited on the round walls of the EPR tube. We hypothesized that magnetophotoselection effects may affect the experiments on the bulk film samples. As described in Chapter 3, magnetophotoselection arises when the paramagnetic photoexcited species in solid samples are formed upon illumination with linearly polarized light, like the laser beam that is used in TR-EPR[18]. This implies a selective excitation of molecules on the basis of their orientation with respect to the light electric field vector ($\vec{E}(t)$), with favored excitation of the molecules oriented with the transition dipole moment parallel to $\vec{E}(t)$. Consequently, the EPR spectrum of the photoexcited species will depend on the relative orientation between $\vec{E}(t)$ and the magnetic field of the spectrometer ($\vec{B}_0$). In triplet state spectra the triplet dipolar tensor direction corresponding to the transition dipole moment will contribute more to the spectrum acquired with $\vec{E}(t)||\vec{B}_0$, while the perpendicular directions will be enhanced with $\vec{E}(t) \perp \vec{B}_0$.

By changing the direction of $\vec{E}(t)$ with respect to $\vec{B}_0$ we verified that magnetophotoselection is effective on the acceptor polymers films, causing the enhancement of the Y transition in the $\vec{E}(t)||\vec{B}_0$ case, and the enhancement of the Z transition in the $\vec{E}(t) \perp \vec{B}_0$ case (Figure 4.4). The first spectra (Figure 4.4 top) were acquired without modification of the normal laser polarization, which is $\vec{E}(t) \perp \vec{B}_0$. Thus, magnetophotoselection provides the explanation for the anomalous EPR lineshape observed in the spectra, without the need to consider less plausible possibilities related to samples characteristics (like molecular order). The effect of magnetophotoselection can be eliminated by the use of an optical depolarizer or by simply summing the parallel spectrum with two times the perpendicular spectrum: the result is a spectrum superimposable to the frozen solution spectrum (Figure 4.4 insets) showing that there is no substantial difference in the polymers triplets in the two phases. Only small differences are found in the D parameters of the triplets, that are slightly smaller in the films (Table 1) due to higher triplet delocalization in the solid state.

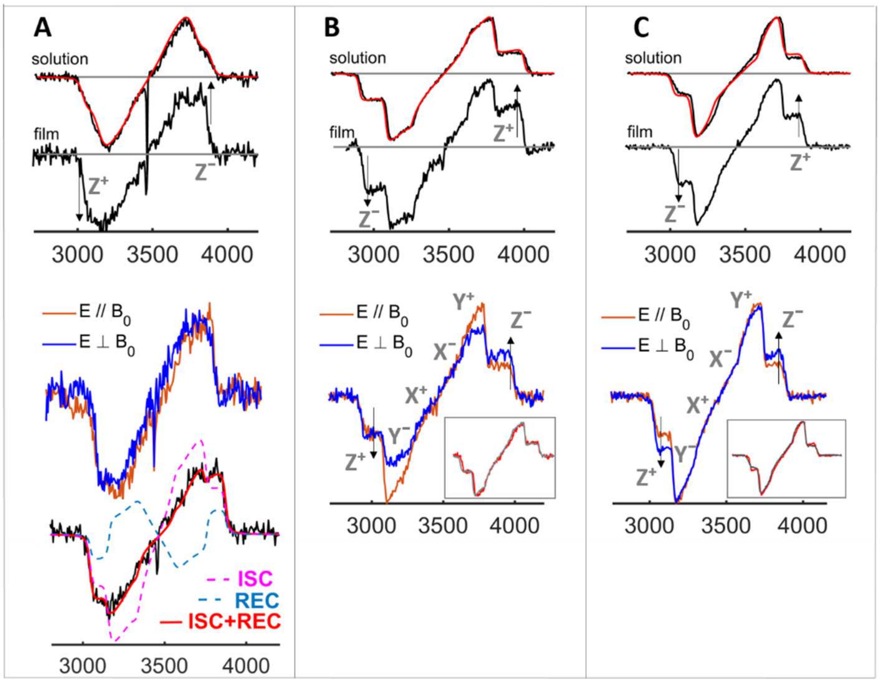

Figure 4.4 TR-EPR spectra (80K) of the polymers in frozen solutions and bulk films. A: PBDT-TS1, solution and film spectra (top), magnetophotoselection on the film (middle), simulation of the film spectra including InterSystem Crossing – ISC – and recombination – REC – (bottom); B and C: P2TPD and P2TPD-BT, solution and film spectra (top), magnetophotoselection on the film (bottom); Insets: superposition of solution spectrum (grey line) and film spectrum without magnetophotoselection (red line).

In the case of the PBDT-TS1 donor polymer film we detected no magnetophotoselection effect. This might be due to superimposed transition dipole moments at the laser excitation wavelength (532 nm) or to energy transfers from the excited molecules to other molecules. Therefore, the difference between the solution and the film triplet spectra seems to be real in this case. We could simulate the film spectrum assuming a contribution to the population of the triplet state by the charge recombination process (Figure 4.4A).

In Table 4.1 the triplet parameters for the various samples are reported.

Table 4.1 Triplet state parameters of the three polymers in frozen solutions and bulk films.

	D (Gauss)	E (Gauss)	Px:Py:Pz
PBDT-TS1 sol	430	70	0.33:0.63:0.04
film	415	60	ISC 0.36:0.46:0.18
			REC T_1-T_0= -1 T_0-T_{-1}=1
P2TPD-[2F]T sol	550	57	0.38:0.58:0.04
film	530	58	0.38:0.58:0.04
P2TPD-BT-[2F]T sol	440	52	0.30:0.49:0.21
film	430	52	0.30:0.49:0.21

The analysis presented in this section allowed to identify and characterize the spectral features of the donor polymer radical cation and to characterize the triplet spectra of each polymer, providing useful information for the interpretation of the results on the blends that will be presented in the following paragraphs.

4.2 Bulk blend films

The bulk blends were obtained upon dissolving in ortho-dichlorobenzene the donor polymer and the acceptors in a 1:2 weight ratio and by removing the solvent inside the EPR tube. The Light-induced EPR spectra at 80K showed a substantial photoinduced charge generation (Figure 4.5). In the case of the blend containing the P2TPD-BT polymer, the spectrum is composed of a signal belonging to the donor radical cation (having the g factor determined in the previous section) and a low field shoulder attributable to the acceptor radical anion. For the blend containing the P2TPD polymer as acceptor, a low-field signal in addition to the radical cation is hardly visible. Despite the low contribution of the anion signal to the spectra, there is no doubt that the acceptor polymers are responsible for the photoinduced electron-transfer in these blends, as the photoinduced signal in absence of the acceptor was much smaller (Figure 4.5).

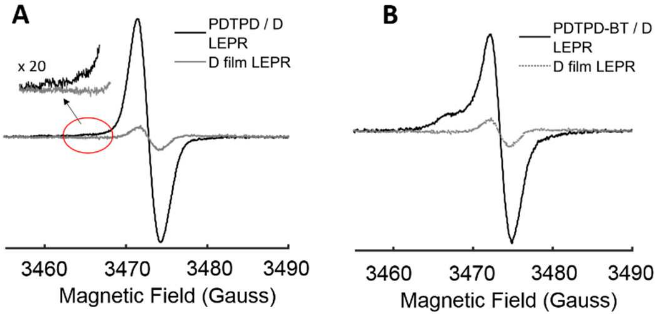

Figure 4.5 Light-induced EPR spectra (80K) of the bulk films of the P2TPD/PBDT-TS1 (A) and the P2TPD-BT/PBDT-TS1 (B) blends. The grey line shows the LEPR spectrum in a film made by the PBDT-TS1 polymer alone.

The small contribution of the anion to the photoinduced signal may have three main origins: unfavorable spin relaxation times, either very short T_2, causing consistent broadening of the line, or a long T_1, giving rise to saturation effects; large inhomogeneity or hyperfine splitting resulting in large linewidth; small lifetime of the anion species, reducing the steady-state concentration detected by the LEPR technique. The effect of relaxation on the detection of the signal can be probed by microwave power saturation experiments, in which the CW-EPR spectrum is measured at various microwave power values. From these experiments (not shown) the relative contribution of the two species was shown to be invariant upon changing the MW power, revealing that saturation factors of the two species are fairly similar so they cannot consistently affect the relative intensities of the two species in CWEPR, at least under ordinary conditions. Another explanation based on an extreme broadening of the inhomogeneous anion line caused by a very large g tensor anisotropy is rather unlikely for organic radicals. The same applies to the hyperfine splittings, that are expected to be small considering the delocalization of the spin over many monomers in conjugated polymers[19,20]. A final possibility considers that the anions are much less stable compared to the cations, for example due to their reactivity towards O_2. This seems to be the most probable reason for the experimental low intensity of EPR signal of the polymer anions.

Literature EPR data confirm the difficulty in detecting anion EPR signals in similar systems: recent work on a blend of the well-known donor polymer MDMO-PPV with a small-molecule acceptor based on the 2,5-dithienylthiazolo[5,4-d]thiazole unit (DTTzTz) showed that only a weak signal of the anion could be detected even at very low T[21].

Despite the low radical anion signal we tried to disentangle it from the cation aiming at determining its characteristics. A double approach was used for this scope: the replacement of the donor polymer with another donor, and the relaxation-based filtering based on Pulsed EPR methods[22].

We chose P3HT to replace the PBDT-TS1 donor, since it has got a well characterized g-tensor (g_1= 2.0030 g_2=2.0020 g_3=2.0010)[19,23], lower than the PBDT-TS1 one, giving rise to an EPR line shifted to higher field. The LEPR spectra of the bulk films of the acceptor polymers blended with P3HT are reported in Figure 4.6. In the P2TPD/P3HT sample the radical anion gives rise to a small low field bump in the EPR spectrum, in analogy to the P2TPD/PBDT-TS1 sample (Figure 4.6A). However, insufficient separation and low signal intensity make the extraction of the anion spectrum impossible. For the P2TPD-BT/P3HT blend the contribution of the anion to the LEPR signal is more intense, allowing for the determination of the g-tensor principal values (Figure 4.6B, Table 2).

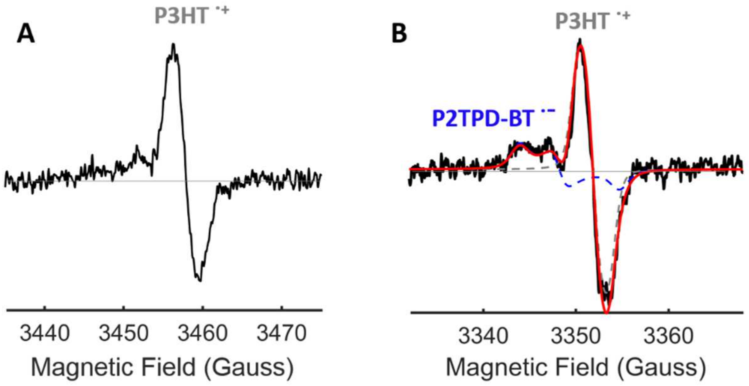

Figure 4.6 LEPR spectra (80K) of P2TPD/P3HT (A) and P2TPD-BT/P3HT (B) blends. B includes the simulation (red line) obtained as summation of P3HT$^{\cdot+}$ (grey dashed line) and P2TPD-BT$^{\cdot-}$ (blue dashed line).

In order to disentangle the P2TPD radical anion signal as well, we used Pulse EPR methods on the P2TPD/PBDT-TS1 blend. Indeed, Pulse EPR allows to disentangle different paramagnetic species on the basis of their difference in electron spin relaxation times. In particular, the electron spin-lattice relaxation T_1 is more often used for this purpose[22]. By measuring the T_1 relaxation times through Inversion Recovery (IR) experiments we verified that the two radicals have sufficiently different longitudinal relaxation: the biexponential fitting of the IR curves at cation ($D^{\cdot+}$) and anion ($A^{\cdot-}$) resonance field positions reveals characteristic relaxation times of 5μs and 60μs for the cation, and 23μs and 260μs for the anion (Figure 4.7). Such a difference in T_1 allows to perform Inversion

Recovery-filtered EDEPR (IRf-EDEPR) experiments (Figure 4.8). In IRf-EDEPR, like in Inversion Recovery experiments, a π pulse precedes the two-pulse echo π/2-τ-π-τ sequence, which is used for detection. However, instead of varying the time T between the inversion pulse and the detection sequence like in IR, the T time is kept fixed and the field is swept. The value of T (T_f) is chosen as to filter out one component of the EDEPR exploiting its relaxation. The radical cation $D^{\cdot +}$, having a faster longitudinal relaxation, can be filtered out from the acquired IRf-EDEPR spectrum by setting the time T_f equal to the time at which its echo crosses the zero-intensity due to the longitudinal relaxation. In this way $D^{\cdot +}$ will not contribute to the detected echo while $A^{\cdot -}$ will give rise to a negative echo (due to the initial inversion pulse).

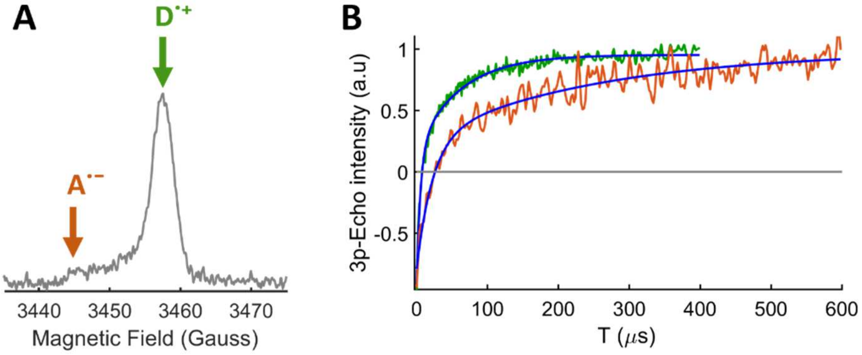

Figure 4.7 A: 2p-EDEPR spectrum (80K) of the P2TPD/PBDT-TS1 bulk film, acquired under light illumination; B: Inversion Recovery at the field positions indicated in A, with biexponential fittings (blue lines).

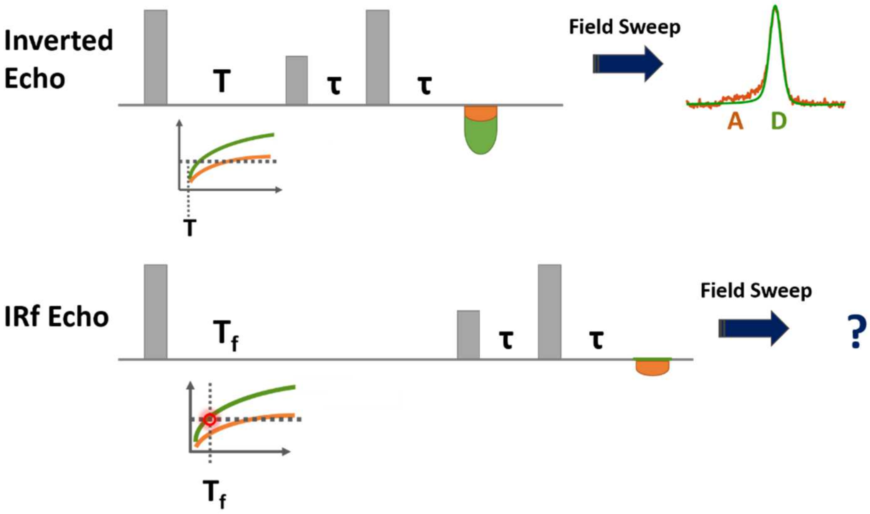

Figure 4.8 Inversion Recovery-filtered EDEPR (IRf-EDEPR) experiment.

The time T_f to filter out the donor contribution was determined from its Inversion Recovery at the maximum intensity field position (Figure 4.7) and corresponds to 5 µs. The resulting IRf-EDEPR spectrum (reversed to have positive intensity) is shown in Figure 4.9 (black line). The normalized donor EDEPR, obtained from an EDEPR measurement on a donor-only film, is superimposed for clarity (green dotted line). High field and low filed shoulders in the IRf spectrum are not present in the donor EDEPR. Therefore, they are attributable to the acceptor radical anion. Assuming that hyperfine interactions are not dominating the spectrum, the two shoulders can be reproduced by a rhombic g-tensor with principal values g_1= 2.0108 g_2=2.0045 g_3=2.0004 (red simulation). The remaining experimental IRf-EDEPR intensity (lilac dotted line) can be explained as residual echo by the donor, due to T_1 anisotropy (slower relaxation with respect to the filtered spin-packets). The validity of this interpretation was checked by comparing the sum of the extracted $A^{\cdot-}$ signal and the $D^{\cdot+}$ experimental EDEPR with the original EDEPR spectrum of the blend, showing good correspondence (Figure 4.9, right). However, considering both the presence of residual Echo by $D^{\cdot+}$ in the IRf-spectrum and the small contribution of the anion to the EDEPR spectrum used for checking the extracted $A^{\cdot-}$ g-tensor, the uncertainty in the determination of the lower g components, that are partially superimposed to the donor spectrum, is quite high.

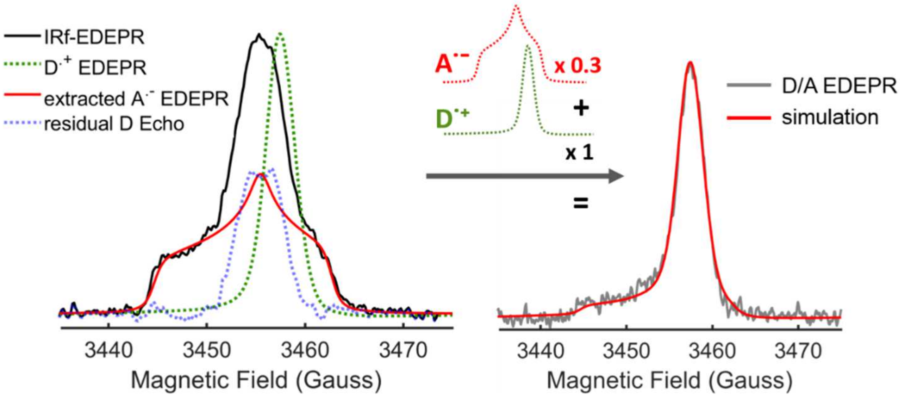

Figure 4.9 Left: IRf-EDEPR spectrum of the P2TPD/PBDT-TS1 bulk film, acquired with Tf=5µs to filter-out the $D^{\cdot+}$ echo (black line), $D^{\cdot+}$ EDEPR spectrum (green dotted line), residual $D^{\cdot+}$ EDEPR intensity after filtration (lilac dotted line), extracted $A^{\cdot-}$ EDEPR spectrum (red line). Right: simulation of the EDEPR spectrum by summing the extracted $A^{\cdot-}$ EDEPR with the $D^{\cdot+}$ EDEPR (right).

DFT calculations were performed in order to support the experimental g-tensor determination for the $P2TPD^{\cdot-}$ and $P2TPD\text{-}BT^{\cdot-}$ radicals. Previous studies have shown that negligible change in the calculated g-values is associated to the length of the oligomer[19]. For this reason, we studied the monomers in order to reduce the computational cost of the calculations. The geometry of the monomers radical anions was optimized using the B3LYP/6-31G method, and the basis set was extended to 6-311G(d) for the calculation of g. The results are reported in Table 4.2 and compared to the experimental values. Excellent correspondence was found for P2TPD-BT$^{\cdot -}$ confirming the adequacy of the computational method. For P2TPD$^{\cdot -}$ the g_1 value was consistently underestimated by the calculation. However, the calculation confirmed the observed decrease in g_1 upon addition of the BT unit with consequent decrease in g-anisotropy. The calculated spin density distribution, depicted in Figure 4.10, highlights the electron-accepting character of the BT moiety, over which 60% of the total spin density is localized in the 2TPD-BT-[2F]T$^{\cdot -}$ monomer.

Table 4.2 Experimental and calculated g-tensor principal values of the radicals of the polymers.

		g_1	**g_2**	**g_3**
PBDT-TS1$^{\cdot +}$	**Exp**	2.0040 (±0.0003)	2.0031 (±0.0003)	2.0022 (±0.0003)
P2TPD-BT$^{\cdot -}$	**Exp**	2.0068 (±0.0003)	2.0042 (±0.0003)	2.0010 (±0.0007)
	Calc	2.0068	2.0044	2.0021
P2TPD$^{\cdot -}$	**Exp**	2.0108 (±0.0005)	2.0045 (±0.0010)	2.0004 (±0.0010)
	Calc	2.0084	2.0055	2.0019

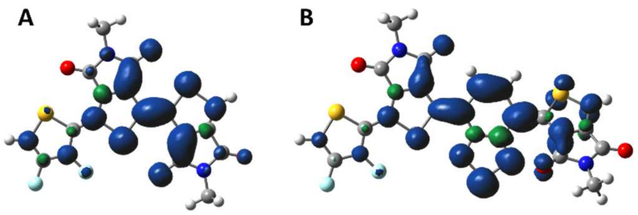

Figure 4.10 Calculated 2TPD-BT-[2F]T$^{\cdot -}$ monomer 2TPD-BT-[2F]T$^{\cdot -}$ monomer spin density.

The g-tensors of the examined radicals are much more anisotropic and with higher values compared to the g-tensors of the majority of the conjugated polymer polarons known in literature, having g_{iso} close to g_e (2.0023) and Δg (g_1-g_3) around 0.0020÷0.0030, regardless of their chemical structure[19,24]. Two examples of this category are the P3HT and the PBDT-TS1 polarons reported in the previous pages. However, the species under examination are negative polarons that have a consistent amount of spin-density localized over the S atoms, namely 18% of the total spin-density for the 2TPD-BT-[2F]T$^{\cdot -}$ and 16% for the 2TPD-[2F]T$^{\cdot -}$ monomers, according to our calculations. To have an idea of the difference with commonly observed polarons, we report that same calculations on the BDT-TS1$^{\cdot +}$ monomer, having close molecular weight and containing even more S atoms, showed that only 6% of the spin-density is localized on them. We believe that this feature may explain the large anisotropy and high g_{iso} value in the radical anions that we detected, due to the large spin-orbit coupling of sulphur atoms. Although there is no literature report on g-tensors of negative polarons in conjugated polymers, some papers can be found in which EPR of the radical anions of small thiophene-based aromatic molecules are reported, revealing high g_{iso} values[25,26]. In ref. [26] the radical anions and cations of two dithienylthiazolo[5,4-d]thiazoles (DTTzTz)-based molecules were studied by EPR and computational methods, showing that higher g-values were associated to the anions along with a higher spin-density on S atoms, in line with our findings.

In this section we showed by LEPR that photoinduced electron-transfer between the PBDT-TS1 donor polymer and the TPD-[2F]T -based acceptors occurs. We also identified the g-tensors of the generated negative polarons, and thus completed the set of preliminary investigations that are useful to interpret data on the spin-coated blends discussed in the following section.

4.3 Spin-coated films

The spin-coated samples of the D/A blends were prepared with the same procedure used for the photoactive films in the devices studied in ref [11] (see Experimental section at the end of the chapter for details).

The EPR study on these samples unraveled both photophysical features of the materials and molecular ordering features, that will be presented in the sections below.

4.3.1 Photophysics

The photogeneration of charges in the spin-coated blends was verified by Light-induced CW-EPR (LEPR) at different temperatures (Figure 4.11). The two blends showed an opposite behavior: in the P2TPD-BT blend a LEPR signal could be detected at room temperature and it was drastically reduced by lowering the temperature down to 80K, while in the P2TPD blend no signal was formed at room temperature but it increased at low T. The spectral shape depends on the orientation of the films inside the magnetic field of the spectrometer, a clear sign of the presence of molecular order, that will be discussed in the following section, while the present discussion will be focused on the photophysical processes occurring in the materials.

The observed signals could be simulated in both blends using the PBDT-TS1 radical cation g-tensor and including some degree of molecular order. Thus, also in the spin-coated blends CW EPR allows to observe the radical cation of the donor polymer only. This is in line with the previous investigations on the bulk films of the blends, where a low contribution of the anion signal was found and attributed to the small lifetime of these species (section 4.2).

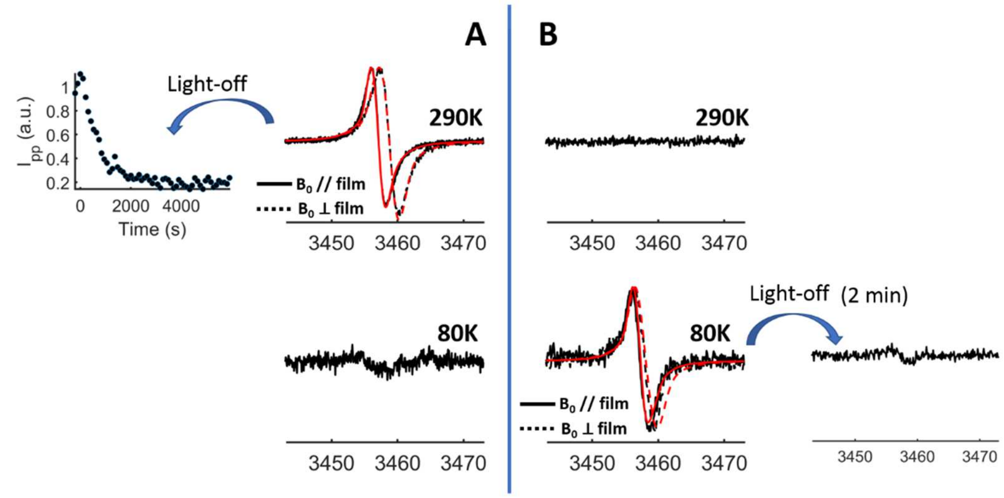

Figure 4.11 A: LEPR spectra of the P2TPD-BT/PBDT-TS1 blend; B: LEPR spectra of the P2TPD/PBDT-TS1 blend. Red lines are simulations obtained using the donor radical cation g-tensor and introducing molecular order as described in section 4.3.2.

In order to rationalize our observations on the temperature dependence of the LEPR signals, we need to refer to the physical description of charge transport in organic semiconductors[27]. According to such description, charge transport in disordered organic materials occurs via a hopping mechanism, opposed to band-like transport that applies to crystalline inorganic semiconductors. Indeed, in molecular materials, the electronic coupling between states of adjacent molecules is weak, introducing energetic barriers for charge-transport (charge transfer). The hopping process can be modeled in the frame of semiclassical Marcus theory and as such it is a thermally-activated mechanism. The charge mobility in the hopping regime is therefore temperature dependent, and its dependence is generally well fitted by the Bassler model according to which $\mu \propto exp(-T_0/T)^2$, where T_0 expresses the energetic disorder of the material[27].

Non-geminate charge recombination in organic semiconductors can often be described according to the Langevin model[28,29], which predicts a recombination rate R proportional to charge mobility:

$$R_{Lang} = \frac{e(\mu_e+\mu_h)}{\varepsilon_r \cdot \varepsilon_0} \cdot n_e n_h \qquad \text{Eq. 4.1}$$

where e is the unit charge, μ_e and μ_h are the electron and hole mobilities, ε_r and ε_0 are the dielectric constants of the material and the vacuum permittivity, and n_e and n_h are the electron and hole densities.

Therefore, we expect that increasing temperature causes an increase in the hopping rate – and thus a more efficient diffusion of charges from the interface where they were formed, reducing geminate recombination – but it also causes an increase in the rate of non-geminate recombination.

In light of this photophysical picture we can explain what happens in the P2TPD/PBDT-TS1 blend. At low T, the hopping rate is small and so is the LEPR signal because only few charges can separate and move far from the interface. The charges that remain close to the interface undergo geminate recombination. At room temperature, although the separation of charges is more efficient due to the increased hopping rate, non-geminate recombination is more effective for the same reason. Non-geminate recombination at room temperature in P2TPD/PBDT-TS1 is so efficient that the resulting steady state concentration of radicals is too low to be detected by LEPR. A direct evidence of the high rate of non-geminate recombination in this blend is given by the light-off spectrum at 80K (Figure 4.11 B) showing that the signal decays immediately after turning off the light, so the rate at room temperature must be even faster.

In the P2TPD-BT/PBDT-TS1 blend the intensity of the light-induced signal increases with T (Figure 4.11 A). At low T we see even a lower photoinduced signal compared to the P2TPD blend, possibly due to a more finely mixed morphology between the two polymers, as suggested by TEM and AFM investigations in ref[11], that is expected to favor geminate recombination. By increasing T, diffusion from the interface is favored, like in the previous blend, however here the impact of non-geminate recombination must be reduced a lot, resulting in an increasing steady state concentration of charges with increasing temperature, i.e. increasing LEPR intensity. A direct observation of the rather slow recombination in this blend compared to the previous one is given by the light-off kinetics at room T (Figure 4.11 A) showing that the charges take more than one hour to recombine after light is switched-off.

This behavior can be explained with the hypothesis of a non-Langevin recombination regime for this blend. Non-Langevin recombination was observed for other semiconducting polymers for which a suppressed recombination rate compared to the one predicted by the Langevin model was observed[30,31]. Furthermore, it was observed that this kind of recombination is not dominated by mobility[32], so high mobility polymers can have low recombination rates, and increasing mobility by increasing T does not have dramatic effects on charge recombination, as it happens in the P2TPD-BT/PBDT-TS1 blend. Among the proposed explanations for this behavior there is the fact that the transport of electrons and holes occurs separately in the two polymers phases, in ‘percolation pathways’ that are energy ‘valleys’ through which charges hop, and recombination only occurs where the two pathways overlap. So, even if charge mobility is high inside these pathways, it has low impact on the recombination rate.

The slower recombination rate in the P2TPD-BT blend compared to the P2TPD one was pointed out also from the electrical characterization of the devices, together with mobility measurements that showed higher mobility of both holes and electrons for this blend[11]. This shows that EPR can be used to correctly predict materials properties in the working devices.

Besides Light-induced EPR, also TR-EPR can be used to probe the photoinduced formation of paramagnetic species inside the materials, and thanks to its higher time resolution (about 100 ns response time), it can be used to reveal short-lived species. The TR-EPR spectra of the spin-coated all-polymer blends extracted at 5 µs after the 532 nm laser flash are shown in Figure 4.12 A and B. The large spectral features can be assigned to triplet states, while the sharp central emissive lines are due to transient polarized radical species. Like in LEPR spectra, we observed a clear spectral dependence on the orientation of the films inside the spectrometer that was simulated as an effect of the internal molecular order, as will be discussed in the following section. In addition to molecular ordering features, two other kinds of information can be obtained from the spectra, i.e. the identity of the detected triplet state and its population mechanism.

The D and E parameters characterize the triplet wavefunction and so they can be used to assign the spectrum to one or the other polymer. Considering the D and E values determined from the single-polymer films (see Table 4.1) we could assign the triplet observed in the P2TPD/PBDT-TS1 blend to the donor PBDT-TS1 polymer. Indeed, P2TPD has a hundred gauss larger value of D, that would lead to a broader spectrum with respect to the observed one. This was confirmed by the simulation, that could be obtained using the PBDT-TS1 triplet dipolar parameters and populations, thus excluding any contribution of the acceptor polymer. For the P2TPD-BT/PBDT-TS1 blend the dipolar parameters and zero field-populations of the triplet states are too similar to allow to distinguish between them in the blend. As a result, the triplet spectrum of the blend film could be satisfyingly simulated using both triplet parameters (in Figure 4.12 only the simulation using the donor triplet parameters is shown). Therefore, in this case the dipolar tensor and populations could not be exploited to determine the identity of the triplet signal. In principle, other spectroscopic parameters can be used for this purpose such as hyperfine couplings with magnetic nuclei. The P2TPD-BT polymer contains ^{14}N atoms, that are absent in PBDT-TS1, so their hyperfine coupling with the electronic spin could be exploited to assign the triplet species. Hence, we tried to perform pulsed ENDOR (Electron-Nuclear DOuble

Resonance) experiments on the photoexcited triplet state. ENDOR is a double resonance technique in which a double excitation is used, microwave excitation for the electron spin and radiofrequency excitation for the nuclear spins, generating peaks at the resonance frequency positions of the coupled nuclear spins, that enable the identification of the hyperfine-coupled nuclei in the paramagnetic species and the determination of their hyperfine constants. Unfortunately, the triplet electron spin-echo of the P2TPD-BT/PBDT-TS1 sample was very weak, resulting in very poor S/N ratio in the ENDOR spectrum. The two main reasons for the low echo intensity were the fast relaxation of the triplet state and the small amount of material in the spin-coated films. Indeed, there is no literature record of ENDOR investigations on triplet states in spin-coated materials, while similar studies were limited to high-triplet yield molecules in solutions[33]. Hence, the assignment of the triplet spectrum in the P2TPD-BT blend was missing from the EPR study.

Considering that both the PBDT-TS1 and the P2TPD polymers have shown significant triplet yield in the single-polymer films (section 4.1), the completely suppressed generation of the acceptor triplet upon photoexcitation of the P2TPD/PBDT-TS1 blend implies a quenching mechanism of the excited state of the acceptor, clearly induced by the interaction with the donor polymer. A possible quenching mechanism that explains our observation is energy transfer from the acceptor singlet excited state to the donor. Due to the superposition of the absorption spectra of the two polymers we could not investigate such a process by selectively exciting the acceptor polymer and recording the TR-EPR spectrum of the blend at this wavelength. However, the demonstration of energy transfer came from TR-PL measurements performed in KAUST in the group of Professor Laquai, showing that, by exciting at 532 nm (where both the donor and the acceptor polymers absorb), the photoluminescence of the donor polymer, monitored at 850 nm (where the acceptor photoluminescence is negligible), increases in the first few ps after excitation (Figure 4.13). The same was found for the P2TPD-BT/PBDT-TS1 blend which suggests that an A*→D* energy transfer is effective in this blend. Therefore, the triplet state that we detected by EPR should correspond to the triplet state of the donor polymer also in this case, in analogy to the other blend.

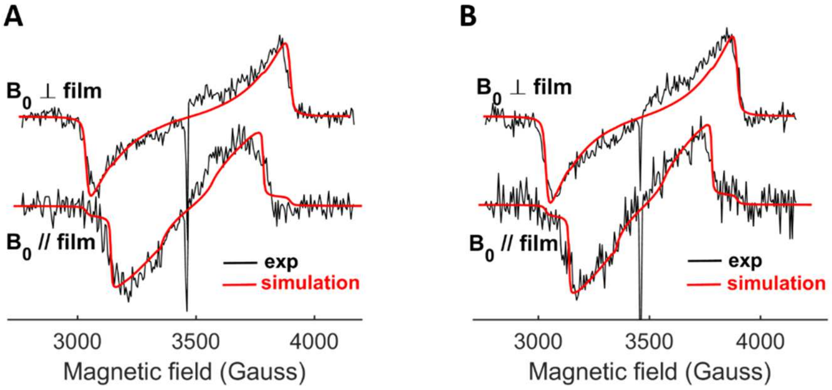

Figure 4.12 TR-EPR spectra of the P2TPD/PBDT-TS1 spin-coated blend (black) with the simulation obtained using the PBDT-TS1 triplet parameters and including molecular order (red); B: TR-EPR spectra of the P2TPD-BT/PBDT-TS1 spin-coated blend (black) with the simulation obtained using the PBDT-TS1 triplet parameters and including molecular order (red); C: TR-PL spectra of the P2TPD/PBDT-TS1 and P2TPD-BT/PBDT-TS1 spin-coated blends.

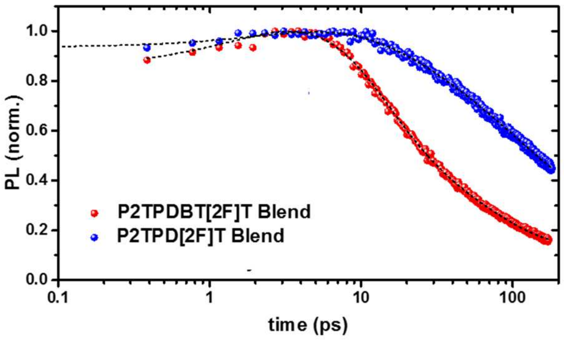

Figure 4.13 TR-PL spectra of the P2TPD/PBDT-TS1 (blue) and P2TPD-BT/PBDT-TS1 (red) spin-coated blends.

The polarization pattern of the TR-EPR spectra could be reproduced assuming Intersystem Crossing as the only population mechanism of the triplet states. Therefore, there is no contribution of charge recombination to the polymers triplet states in the blends. On the contrary, in the donor-only film we found that part of the triplet states was formed upon back electron transfer (see section 4.1). Likely, the suppression of recombination to the triplet in the blend is due to the energy stabilization of the charge-transfer states, since the electron transfer from the donor polymer to the acceptor polymer molecules is more energetically favorable compared to electron transfer from donor molecules to other donor molecules. This stabilization lowers the energy of the CT states below the energy of the triplet state, making recombination to the triplet state impossible.

To summarize, from the above data we can draw a picture of the photophysical processes occurring in these blends (Figure 4.15 A). After light-excitation some molecules undergo electron transfer from the donor to the acceptor polymer. Among the excited molecules that are not immediately involved in electron transfer, there are some donor polymer molecules that undergo Intersystem crossing to the triplet state, and some excited acceptor molecules that transfer energy to donor molecules that are promoted to their excited singlet state. These newly excited donor molecules can transfer electrons to the acceptor or convert to the triplet state by ISC. The triplet state is higher in energy compared to the charge-transfer states, so it could be formally able to undergo electron transfer.

Since the P2TPD and P2TPD-BT acceptor polymers are meant to replace fullerene derivatives in polymer solar cells, we used EPR to bring to light potential differences between the photophysics of the all-polymer blends and the blend of the same donor with PCBM. To this end, we prepared a bulk film of the PBDT-TS1/PCBM blend and studied it by TR-EPR. The TR-EPR spectrum extracted at 5 μs after the laser pulse is reported in Figure 4.14. The spectral region of the PCBM triplet is shown in the figure as it reveals the most interesting information: the triplet of PCBM in the blend is populated by both ISC and charge recombination. Indeed, the ISC polarization pattern of PCBM triplet[34] is strikingly different from the observed polarization, that can be fitted only by adding a contribution of charge recombination to the PCBM excited triplet state. This phenomenon was already observed in other systems and it is related to the energy of the PCBM triplet, being often lower compared to the charge-transfer states, that therefore can easily recombine to the PCBM triplet state[34,35]. Charge recombination to triplet states is generally recognized as a loss mechanism in organic solar cells, since the energy-matching requirement between the CT state and the triplet implies that the excitation energy stored in the triplet state cannot undergo further electron transfer to produce free charges[34,36,37,38,39]. It is then remarkable that this mechanism is absent when PCBM is replaced by one of the acceptor polymers that we studied, as we verified that only ISC triplets are formed when they are used in blends with the same donor. This makes the polymers attractive substitutes of PCBM.

In Figure 4.15 a scheme is reported showing the different photophysical processes occurring in the all-polymer blends and in the PCBM blend, that were unraveled by EPR.

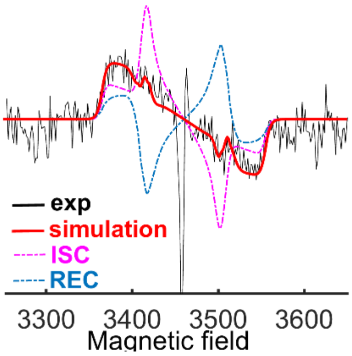

Figure 4.14 TR-EPR spectrum of PCBM in the PBDT-TS1/PCBM blend film, simulated by summing ISC and recombination contributions.

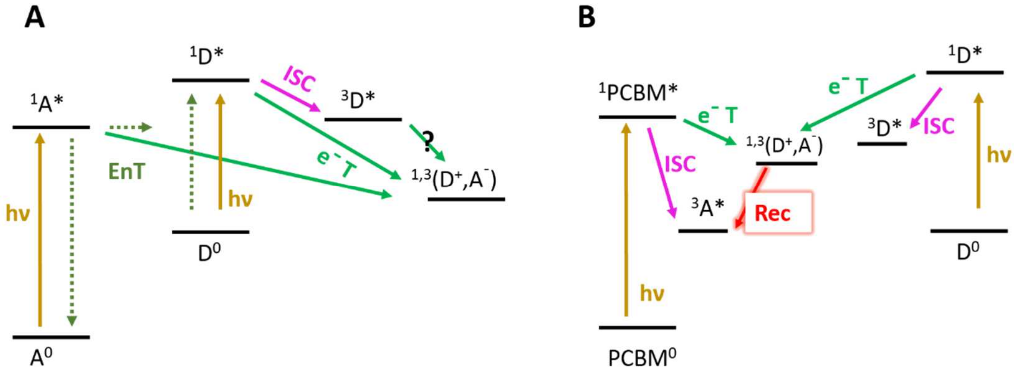

Figure 4.15 Schemes for the photo-induced processes in the all-polymer blends (A) and in the PBDT-TS1/PCBM blend (B).

4.3.2 Molecular Order

We observed that both the spectra of photoinduced radicals (Figure 4.11) and triplet states (Figure 4.12) in the spin-coated films depend on the orientation of the films with respect to the static magnetic field of the spectrometer. This is a consequence of partial orientational order at the molecular level in the material and it can be analyzed as described in Chapter 3.

The orientational order was modeled using the uniaxial orientational distribution function reported in Chapter 3 (Eq. 3.10), characterized by the ε' parameter and depending on the angle θ between a director vector, defined in the laboratory frame, in our case chosen as the normal to the film plane ($\hat{\mathrm{n}}$), and a vector in the molecular frame ($\hat{\mathrm{k}}_{\mathrm{mol}}$). The spectral simulations were obtained using this orientational distribution function to weight each orientation contributing to the spectrum. In this way we found the best ε' value reproducing the experimental data, and the coordinates of the molecular axis $\hat{\mathrm{k}}_{\mathrm{mol}}$ with respect to the magnetic tensor frame (Zero-Field Splitting tensor in case of triplet species, g tensor in case of radical species). From ε' knowledge we could calculate the order parameter S (Eq. 3.11), while we needed to express $\hat{\mathrm{k}}_{\mathrm{mol}}$ in the molecular frame in order to understand how the molecules were oriented. For this reason, the assignment of the magnetic tensors to the molecular frame was necessary, and it was addressed by combining experiments and calculations.

For the assignment of the dipolar tensor to interpret the angular dependence of the triplet spectra, we started by using a nematic liquid crystal (E7) solution of the donor polymer, since it is the polymer to which the observed triplet was assigned (see previous section). As shown in Chapter 3 polymers tend to assume an elongated conformation in the oriented nematic liquid crystal, with the backbone oriented parallel to the nematic director. Thus, the analysis of the triplet spectrum inside the nematic phase allows to place the backbone direction in the dipolar tensor frame.

The TR-EPR spectra of the PBDT-TS1 liquid crystal matrix are reported in Figure 4.16 A. The frozen isotropic phase was studied first, in order to determine the dipolar parameters of the polymer in the E7 solvent. Then the liquid crystal was oriented using the spectrometer magnetic field and two spectra were acquired with the field parallel and perpendicular to the nematic director. The result is similar to the results found for the polymers in Chapter 3: only one triplet component is detected with the magnetic field parallel to the nematic director, while the other two are visible in the perpendicular direction. This indicates that the polymer is highly oriented in the nematic phase (S=0.87 from simulation) and reveals that the backbone coincides with the X_{ZFS} axis.

The complete assignment of the tensor was achieved by DFT calculations of the dipolar interaction on the optimized triplet state geometry of the BDT-TS1 dimer, using the B3LYP/EPR-II (def2-TZVPP for S atoms) method (further details are given in the Experimental section). From the calculation, the X_{ZFS} axis, conventionally corresponding to the dipolar principal axis with the middle principal value (absolute value), was predicted to be along the backbone, in agreement with the experiment. The Z_{ZFS} axis instead, was predicted to be perpendicular to the molecular plane (Figure 4.16 B).

The assignment of the dipolar tensor described above was used to extract the information on the kind of orientational order inside the films from the results of the simulations of the triplet spectra (Table 4.3). For both blends the Z_{ZFS} axis was found to be the molecular orienting axis ($\hat{\mathrm{k}}_{\mathrm{mol}}$) laying perpendicular to the film plane with an order parameter S=+0.50, meaning that the prevailing orientation is a *face-on* orientation in both films, with 65% of molecules oriented within ± 40° from the normal to the film plane.

The radical spectra are dominated by the Zeeman interaction, therefore the interpretation of molecular order from them requires the assignment of the g-tensor to the molecular frame. This was achieved using computational methods in accordance with literature examples[19,26]. The B3LYP/6-311G(d) method was applied to the optimized radical cation geometry of the BDT-TS1 dimer (since the spectra were assigned to the PBDT-TS1 radical) and gave the tensor orientation depicted in Figure 4.16 C, with the g_3 axis essentially perpendicular to the molecular aromatic plane and g_2 along the backbone.

From the simulation of the LEPR radical spectra including molecular order, the g_3 axis was found to be preferentially oriented normal to the film plane with quite different order parameters for the two blends, being +0.85 for the P2TPD-BT blend and +0.60 for the P2TPD blend film (Table 4.3). Using the tensor assignment, such order corresponds to a preferred *face-on* orientation (Figure 4.17).

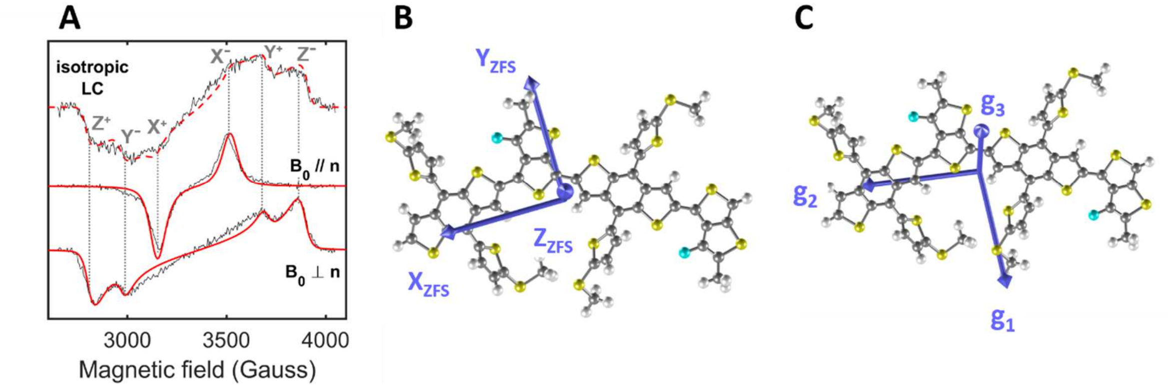

Figure 4.16 A: TR-EPR spectra (130K) of PBDT-TS1 in E7; B: ZFS tensor orientation in the molecular frame as determined from DFT calculations; C: radical cation g tensor orientation in the molecular frame as determined from DFT calculations.

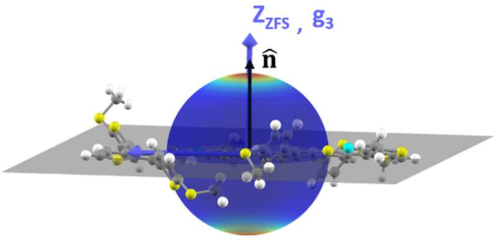

Figure 4.17 Scheme for the face-on molecular orientation. The sphere represents the orientational distribution function (blue: low value, red: high value).

Table 4.3 Results of the simulation of orientational order in the blends spin-coated films.

Blend	Paramagnetic probe	$\hat{\mathbf{k}}_{\mathbf{mol}}$	S
P2TPD-BT-2FT/donor	donor triplet	Z_{ZFS}	+0.50 (±0.05)
	donor radical	g_3	+0.85 (±0.02)
P2TPD-2FT /donor	donor triplet	Z_{ZFS}	+0.50 (±0.05)
	donor radical	g_3	+0.60 (±0.05)

The reported results show that the degree of order detected from the analysis of the EPR spectra of the radical species is higher compared to the order resulting from the analysis of triplet state spectra. This is not surprising considering that the two paramagnetic species are likely formed in different regions of the material since electron transfer and Intersystem Crossing are competing processes. Therefore, the presented EPR investigation allows to probe different areas in the polymer blends.

The radical cation species that we can detect by LEPR are stable species (with lifetimes longer than milliseconds) that are most likely located in donor-rich domains where charge recombination is slowed-down and where the polymer can stack and give rise to more ordered structures compared to the domains where the donor and the acceptor polymers are finely mixed. The triplet states may be instead more homogeneously distributed, probing a lower average order compared to the radicals. However, as expected, the kind of order probed by triplets and radicals is the same, being face-on in both cases.

From the comparison of the order parameters determined for the two blends, it emerges that highly ordered domains of the donor polymer are present in the P2TPD-BT/PBDT-TS1 blend (S=0.80) with respect to the P2TPD/PBDT-TS1 blend. In light of the established importance of molecular order for charge transport in molecular semiconductors[40,41,42,43], we believe that this characteristic contributes to the better performance of the P2TPD-BT blend and explains the higher hole-mobility as observed in ref. [11].

Unfortunately, the lack of detectable paramagnetic species in the acceptor polymer domains, prevented us from probing also the degree of order of this polymer in the blends, that could probably explain the strikingly different electron mobilities measured in ref. [11].

4.4 Conclusions

In this Chapter a new class of organic photovoltaic blends, where conjugated polymers play both the role of electron-donor and electron-acceptor materials, was investigated using EPR spectroscopy.

The study of the single polymers provided a characterization of their pristine paramagnetic species. The PBDT-TS1 donor polymer was found to be easily oxidized in air and its g-tensor was determined. On the contrary, the TPD-2[FT]-based acceptor polymers were essentially stable with respect to air oxidation due to their higher oxidation potential, related to lower HOMO level.

By laser photoexcitation the first excited triplet state of the polymers was generated and the Zero-field splitting parameters were determined from TR-EPR spectra. The D value of the triplets reflected the monomer dimension. Indeed, the P2TPD polymer, having the smallest monomeric unit and thus the most localized triplet, has the largest triplet D value, while PBDT-TS1 and P2TPD-BT have smaller and very close D.

The use of magnetophotoselection experiments for the measurement of the triplet EPR spectra of the polymers showed that photoselection actually affects the measurements on polymer films evaporated in the EPR tubes ('bulk films'), and therefore it should be taken into account when analyzing the spectra to avoid misinterpretations. In this respect, literature records are known in which molecular ordering was claimed for films of similar polymers processed in the same way, where measurements were likely affected by magnetophotoselection[17]. From our analysis the polymer films deposited on the EPR tube walls appear to be disordered systems, like polymers frozen solutions, that therefore can be used to characterize the polymers triplet in the solid state, without molecular ordering effects.

From the study of the donor/acceptor bulk films we verified that photoinduced electron-transfer between the two polymers occurs with formation of radicals in both polymers. Despite the spectral superposition of positive and negative radicals, an effort was made to determine the g-tensors of the radical anions, either by using P3HT as alternative donor, or by relaxation-filtering techniques. The resulting g-tensors have high g_{iso} and are highly anisotropic compared to common conjugated polymers positive radicals, which, by the aid of DFT calculations, was attributed to the high spin-density on S atoms. To the best of our knowledge, this is the first report of g-tensors of negative polarons in conjugated polymers.

The EPR investigation of the spin-coated thin films of the donor/acceptor blends revealed a much slower non-geminate recombination regime in the blend containing the P2TPD-BT acceptor with respect to the one with P2TPD. Furthermore, from the analysis of molecular order in the films, revealing preferred *face-on* orientation for the donor polymer in both blends, it emerged that highly ordered regions are present in the donor phase in the blend with the P2TPD-BT acceptor, which may contribute to determine the higher mobility and the better photovoltaic performance of the blend.

TR-EPR experiments showed that donor triplet state species are formed upon photoexcitation of both samples, while the formation of the acceptor triplet is prevented by quenching of the excitation upon electron transfer and energy transfer to the donor. This shows that there are no acceptor domains behaving like isolated polymer domains (otherwise the triplet would form by ISC like in the acceptor-only film), meaning that these acceptor polymers provide good electronic contact with the donor polymer domains. The detected donor triplet EPR spectra provided also another information, namely the absence of charge recombination to the triplet state in the blends, a process that has been known for long as a cause of energy loss in photovoltaic blends. We also showed that the same donor polymer with the common PCBM acceptor is affected by charge recombination to the fullerene triplet state. Thus, the newly introduced TPD-2[FT]-based acceptor polymers appear as promising substitutes of fullerene acceptors.

4.5 Experimental

4.5.1 Materials

P2TPD-BT-[2F]T and P2TPD-[2F]T were synthesized in KAUST (King Abdullah University of Science and Technology) following the procedure described in ref. [11]. PBDT-TS1 (Mn 36 kDa, PDI 2) was purchased from Solarmer. P3HT (regioregularity>98%, Mn 71 kDa, PDI 1.7) and PCBM were purchased from Sigma-Aldrich and used without further purifications.

4.5.2 Samples preparation

Polymers solutions were prepared at a concentration of 1mg/ml in oDCB. They were put inside EPR quartz tubes and degassed by few freeze-pump-thaw cycles. Finally, they were sealed under vacuum (10^{-3} Torr).

The evaporated films (bulk films) of the single polymers were prepared from 1mg/ml solutions, that were put inside the EPR tube before letting the solvent evaporate under vacuum (10^{-3} Torr). The same procedure was used for the bulk films of the blends, starting from a 1:2 donor/acceptor weight ratio solution in ODCB, with a total concentration of 3 mg/ml. The EPR tubes were then sealed under vacuum.

The evaporated films of the acceptor polymers with P3HT, and the film of the donor polymer with PCBM, were prepared in the same way from 1:1 weight ratio solutions.

The spin-coated samples were prepared in KAUST starting from 1:2 donor/acceptor weight ratio solutions with an overall concentration of 10 mg/ml. The solutions were spin-cast on PET substrates in a glove box at 2000 rpm for 30 sec, using a programmable spin coater from Specialty Coating Systems (Model G3P-8). The films were then cut into slices and put into the EPR quartz tubes, that were sealed under N_2 atmosphere using an epoxy glue.

4.5.3 EPR

EPR experiments were performed on a X-band ELEXSYS E580 Bruker spectrometer, equipped with a dielectric resonator inside an Oxford CF900 cryostat. For spin-coated samples, the sample orientation inside the spectrometer was aided by the use of a goniometer.

In Light-induced EPR experiments photoexcitation of the samples was obtained using the white light from a 300 W Xe lamp, that was IR filtered and focused into a quartz optical fiber bringing the light to the sample inside the resonator. Typical microwave power attenuation in LEPR experiments was 30dB (source power 149 mW) to avoid saturation effects.

In TR-EPR experiments the signal was directly detected by a LeCroy oscilloscope, without field modulation. The background signal was eliminated using off-resonance signals, that were subtracted from the on-resonance ones at each time point. The photoexcitation was obtained from Nd:YAG pulsed lasers (Quantel Brilliant, λ = 532 nm, pulse length = 5 ns; E/pulse = ca. 5 mJ; repetition rate 10Hz). The spectra were acquired at 25 dB microwave power attenuation, with 256 field points and typically 250 averages per point.

The spectral simulations without molecular order were carried out using Easyspin[44], while an home-made program implemented in Matlab was used to simulate systems including molecular orientational order.

4.5.4 DFT

Geometry optimizations were carried out in Gaussian[45] using the B3LYP/6-31G DFT method. The aliphatic side chains were always approximated with methyl groups.

For the calculations of g-tensors of the radicals, the B3LYP/6-311G(d) DFT method in Gaussian was used. DFT calculations with ORCA[46], using the B3LYP functional with the def2-TZVPP basis set for S atoms and EPR-II for first row atoms, were also performed but gave g-values that were less close to the experimental ones. For this reason, Gaussian results were preferred.

The calculations of the ZFS tensor were carried out with two methods. In both cases the geometry of the triplet state was optimized in Gaussian at the B3LYP/6-31G DFT level.

The first method was highly approximated since it involved the calculation of the ZFS-tensor based on the point-dipole approximation[47], using the Mulliken spin-populations calculated in Gaussian with the B3LYP/6-311G DFT method. The ZFS tensor values predicted by this method deviated from the experimental ones for nearly one order of magnitude (D_{calc}= 2700 G, E_{calc}=577 G).

The second method was implemented in ORCA, that offers the possibility of calculating the ZFS tensor with DFT methods. It was used in literature to successfully predict zero-field splitting values and the tensor orientation in porphyrin systems[33]. The triplet wavefunction in this case was calculated in ORCA using the B3LYP functional with the EPR-II basis set for H-C-N-O and the def2-TZVPP basis set for S. Then the ZFS tensor was calculated by the software using UNO (spin-unrestricted natural orbitals) determinants as described in ref. [48]. The ZFS tensor values predicted by this method were much closer to the experimental ones (D_{calc}= 282 G, E_{calc}=31 G), as expected considering the higher accuracy of the calculation.

Despite the fundamental differences between the two methods, both of them predicted the same orientation of the Z axis i.e. perpendicular to the molecular plane. However, the second method could also approximately predict the experimentally verified correspondence of the X axis with the polymer backbone (as shown in Figure 4.16).

Although also the second method could be improved by improving the accuracy of the calculation of the triplet wavefunction, for the scope of our analysis i.e. the determination of the ZFS tensor orientation in the molecular frame to help identifying molecular order, we can rely on the results since at least one of the predicted directions coincides with the experiment and also considering that the Z direction was predicted to be normal to the plane by two methods.

4.6 References

(1) Chen, W.; Zhang, Q. Recent Progress in Non-Fullerene Small Molecule Acceptors in Organic Solar Cells (OSCs). *J. Mater. Chem. C* **2017**, *5*, 1275–1302.

(2) Baran, D.; Ashraf, R. S.; Hanifi, D. A.; Abdelsamie, M.; Gasparini, N.; Röhr, J. A.; Holliday, S.; Wadsworth, A.; Lockett, S.; Neophytou, M.; et al. Reducing the Efficiency–stability–cost Gap of Organic Photovoltaics with Highly Efficient and Stable Small Molecule Acceptor Ternary Solar Cells. *Nat. Mater.* **2017**, *16*, 363–370.

(3) Holliday, S.; Ashraf, R. S.; Wadsworth, A.; Baran, D.; Yousaf, S. A.; Nielsen, C. B.; Tan, C.; Dimitrov, S. D.; Shang, Z.; Gasparini, N.; et al. High-Efficiency and Air-Stable P3HT-Based Polymer Solar Cells with a New Non-Fullerene Acceptor. *Nat. Commun.* **2016**, *7*, 11585.

(4) Nielsen, C. B.; Holliday, S.; Chen, H.; Cryer, S. J.; McCulloch, I. Non-Fullerene Electron Acceptors for Use in Organic Solar Cells. *Acc. Chem. Res.* **2015**, *48*, 2803–2812.

(5) Hou, J.; Inganäs, O.; Friend, R. H.; Gao, F. Organic Solar Cells Based on Non-Fullerene Acceptors. *Nat. Mater.* **2018**, *17*, 119–128.

(6) Kim, T.; Kim, J.; Kang, T. E.; Lee, C.; Kang, H.; Shin, M.; Wang, C.; Ma, B.; Jeong, U.; Kim, T.; et al. Flexible, Highly Efficient All-Polymer Solar Cells. *Nat. Commun.* **2015**, *6*, 8547.

(7) Facchetti, A. Polymer Donor – Polymer Acceptor (all-Polymer) Solar Cells. *Mater. Today* **2013**, *16*, 123–132.

(8) Andersson, M. R.; Janssen, R. A. J.; Wang, E. High Performance All-Polymer Solar Cells by Synergistic Effects of Fine-Tuned Crystallinity and Solvent Annealing. *J. Am. Chem. Soc.* **2016**, *138*, 10935–10944.

(9) Cheng, P.; Ye, L.; Zhao, X.; Hou, J.; Yongfang, L.; Zhan, X. Binary Additives Synergistically Boost the Efficiency of All-Polymer Solar Cells up to 3.45%. *Energy Environ. Sci.* **2014**, *7*, 1351–1356.

(10) Liu, S.; Kan, Z.; Thomas, S.; Cruciani, F.; Brédas, J. B.; Beaujuge, P. M. Thieno[3,4-C]pyrrole-4,6-Dione-3,4-Difluorothiophene Polymer Acceptors for Efficient All-Polymer Bulk Heterojunction Solar Cells. *Angew. Chemie Int. Ed.* **2016**, *128*, 13190–13194.

(11) Liu, S.; Song, X.; Thomas, S.; Kan, Z.; Cruciani, F.; Laquai, F.; Bredas, J.; Beaujuge, P. M. Thieno [3,4-c] Pyrrole-4,6-Dione-Based Polymer Acceptors for High Open-Circuit Voltage All-Polymer Solar Cells. *Adv. Energy Mater.* **2017**, 160274/1–12.

(12) Liao, S.; Jhuo, H.; Cheng, Y.; Chen, S. Fullerene Derivative-Doped Zinc Oxide Nanofilm as the Cathode of Inverted Polymer Solar Cells with Low-Bandgap Polymer (PTB7-Th) for High Performance. *Adv. Mater.* **2013**, *25*, 4766–4771.

(13) Ye, L.; Zhang, S.; Zhao, W.; Yao, H.; Hou, J. Highly Efficient 2D-Conjugated Benzodithiophene-Based Photovoltaic Polymer with Linear Alkylthio Side Chain. *Chem. Mater.* **2014**, *26*, 3603–3605.

(14) He, Z.; Xiao, B.; Liu, F.; Wu, H.; Yang, Y.; Xiao, S.; Wang, C.; Russell, T. P.; Cao, Y. Single-Junction Polymer Solar Cells with High Efficiency and Photovoltage. *Nat. Photonics* **2015**, *9*, 174–179.

(15) Abdou, M. S. A.; Orfino, F. P.; Son, Y.; Holdcroft, S.; Va, C.; December, R. V. Interaction of Oxygen with Conjugated Polymers: Charge Transfer Complex Formation with Poly(3-Alkylthiophenes). *J. Am. Chem. Soc.* **1997**, *119*, 4518–4524.

(16) Susarova, D. K.; Piven, N. P.; Akkuratov, A. V; Frolova, L. A.; Polinskaya, M. S.; Ponomarenko, S. A.; Babenko, S. D.; Troshin, P. A. ESR Spectroscopy as a Powerful Tool for Probing the Quality of Conjugated Polymers Designed for Photovoltaic Applications. *Chem. Commun.* **2015**, *51*, 2239–2241.

(17) Biskup, T.; Sommer, M.; Rein, S.; Meyer, D. L.; Kohlstädt, M.; Würfel, U.; Weber, S. Ordering of PCDTBT Revealed by Time-Resolved Electron Paramagnetic Resonance Spectroscopy of Its Triplet Excitons. *Angew. Chemie Int. Ed.* **2015**, *54*, 7707–7710.

(18) El-Sayed, M. A.; Siegel, S. Method of "Magnetophotoselection" of the Lowest Excited Triplet State of Aromatic Molecules. *J. Chem. Phys.* **1966**, *44*, 1416–1423.

(19) Niklas, J.; Mardis, K. L.; Banks, B. P.; Grooms, G. M.; Sperlich, A.; Dyakonov, V.; Beaupré, S.; Leclerc, M.; Xu, T.; Yu, L.; et al. Highly-Efficient Charge Separation and Polaron Delocalization in Polymer-Fullerene Bulk-Heterojunctions: A Comparative Multi-Frequency EPR and DFT Study. *Phys. Chem. Chem. Phys.* **2013**, *15*, 9562–9574.

(20) Steyrleuthner, R.; Zhang, Y.; Zhang, L.; Kraffert, F.; Behrends, J. Impact of Morphology on Polaron Delocalization in a Semicrystalline Conjugated Polymer. *Phys. Chem. Chem. Phys.* **2017**, *19*, 3627–3639.

(21) Nevil, N.; Ling, Y.; Mierloo, S. Van; Kesters, J.; Piersimoni, F.; Adriaensens, P.; Lutsen, L.; Vanderzande, D.; Manca, J.; Maes, W.; et al. Charge Transfer in the Weak Driving Force Limit in Blends of MDMO-PPV and Dithienylthiazolo [5,4-D] Thiazoles towards Organic Photovoltaics with High V_{OC}. *Phys. Chem. Chem. Phys.* **2012**, *14*, 15774–15784.

(22) Van Landeghem, M.; Maes, W.; Goovaerts, E.; Van Doorslaer, S. Disentangling Overlapping High-Field EPR Spectra of Organic Radicals: Identification of Light-Induced Polarons in the Record Fullerene-Free Solar Cell Blend PBDB-T:ITIC. *J. Magn. Reson.* **2018**, *288*, 1–10.

(23) Aguirre, A.; Gast, P.; Orlinskii, S.; Akimoto, I.; Groenen, E. J. J.; El Mkami, H.; Goovaerts, E.; Van Doorslaer, S. Multifrequency EPR Analysis of the Positive Polaron in I2-Doped poly(3-Hexylthiophene) and in poly[2-Methoxy-5-(3,7-Dimethyloctyloxy)]-1,4-Phenylenevinylene. *Phys. Chem. Chem. Phys.* **2008**, *10*, 7129–7138.

(24) Niklas, J.; Poluektov, O. G. Charge Transfer Processes in OPV Materials as Revealed by EPR Spectroscopy. *Adv. Energy Mater.* **2017**, 1602226.

(25) Gerson, F.; Gleiter, R.; Ohya-Nishiguchi, H. Isomerization of the Radical Anions of 6a-Thiathiophthenes. *Helv. Chim. Acta* **1977**, *60*, 1220–1225.

(26) Ling, Y.; Mierloo, S. Van; Schnegg, A.; Fehr, M.; Adriaensens, P.; Lutsen, L.; Vanderzande, D.; Maes, W.; Goovaerts, E.; Van Doorslaer, S. Electronic Structure of Positive and Negative Polarons in Functionalized Dithienylthiazolo-[5,4-D]thiazoles: a Combined EPR and DFT Study. *Phys. Chem. Chem. Phys.* **2014**, *16*, 10032–10040.

(27) Coropceanu, V.; Cornil, J.; A. da Silva Filho, D.; Olivier, Y.; Silbey, R.; Brédas, J.-L. Charge Transport in Organic Semiconductors. *Chem. Rev.* **2007**, *107*, 926–952.

(28) Holst, J. J. M. Van Der; Oost, F. W. A. Van; Coehoorn, R.; Bobbert, P. A. Electron-Hole Recombination in Disordered Organic Semiconductors: Validity of the Langevin Formula. *Phys. Rev. B* **2009**, *80*, 235202/1–8.

(29) Wagenpfahl, A. Mobility Dependent Recombination Models for Organic Solar Cells. *J. Phys. Condens. Matter* **2017**, *29*, 373001.

(30) Adriaenssens, G. J.; Arkhipov, V. I. Non-Langevin Recombination in Disordered Materials with Random Potential Distributions. *Solid State Commun.* **1997**, *103*, 541–543.

(31) Clarke, T. M.; Lungenschmied, C.; Peet, J.; Drolet, N.; Mozer, A. J. Tuning Non-Langevin Recombination in an Organic Photovoltaic Blend Using a Processing Additive. *J. Phys. Chem. C* **2015**, *119*, 7016–7021.

(32) Privikas, A.; Sariciftci, N. S.; Juska, G.; Osterbacka, R. A Review of Charge Transport and Recombination in Polymer/Fullerene Organic Solar Cells. *Prog. Photovoltaics Res. Appl.* **2007**, *15*, 677–696.

(33) Tait, C. E.; Neuhaus, P.; Anderson, H. L.; Timmel, C. R. Triplet State Delocalization in a Conjugated Porphyrin Dimer Probed by Transient Electron Paramagnetic Resonance Techniques. *J. Am. Chem. Soc.* **2015**, *137*, 6670–6679.

(34) Franco, L.; Toffoletti, A.; Ruzzi, M.; Montanari, L.; Carati, C.; Bonoldi, L.; Po', R. Time-Resolved EPR of Photoinduced Excited States in a Semiconducting polymer/PCBM Blend. *J. Phys. Chem. C* **2013**, *117*, 1554–1560.

(35) Righetto, M.; Privitera, A.; Carraro, F.; Bolzonello, L.; Ferrante, C.; Franco, L.; Bozio, R. Engineering Interactions in QDs-PCBM Blends: A Surface Chemistry Approach. *Nanoscale* **2018**, *10*, 11913–11922.

(36) Schlenker, C. W.; Li, C.; Yip, H.; Jen, A. K.; Rao, A.; Chow, P. C. Y.; Ge, S.; Ginger, D. S.; Friend, R. H. The Role of Spin in the Kinetic Control of Recombination in Organic Photovoltaics. *Nature* **2013**, *500*, 435–440.

(37) Kraffert, F.; Steyrleuthner, R.; Albrecht, S.; Neher, D.; Scharber, M. C.; Bittl, R.; Behrends, J. Charge Separation in PCPDTBT:PCBM Blends from an EPR Perspective. *J. Phys. Chem. C* **2014**, *118*, 28482–28493.

(38) Janssen, R. A. J.; Veldman, D.; Meskers, S. C. J. The Energy of Charge-Transfer States in Electron Donor – Acceptor Blends : Insight into the Energy Losses in Organic Solar Cells. *Adv. Funct. Mater.* **2009**, *19*, 1939–1948.

(39) Ohkita, H.; Cook, S.; Astuti, Y.; Duffy, W.; Heeney, M.; Tierney, S.; Mcculloch, I.; Bradley, D. C.; Durrant, J. R. Radical Ion Pair Mediated Triplet Formation in Polymer – Fullerene Blend Films. **2006**, *100*, 3939–3941.

(40) Sirringhaus, H.; Brown, P. J.; Friend, R. H.; Nielsen, M. M.; Bechgaard, K.; Langeveld-Voss, B. M. W.; Spiering, a. J. H.; Janssen, R. a. J.; Meijer, E. W.; Herwig, P.; et al. Two-Dimensional Charge

Transport in Self-Organized, High-Mobility Conjugated Polymers. *Nature* **1999**, *401*, 685–688.

(41) Steyrleuthner, R.; Pietro, R. Di; Collins, B. A.; Polzer, F.; Himmelberger, S.; Schubert, M.; Chen, Z.; Zhang, S.; Salleo, A.; Ade, H.; et al. The Role of Regioregularity, Crystallinity, and Chain Orientation on Electron Transport in a High-Mobility N-Type Copolymer. *JACS* **2014**, *136*, 4245–4256.

(42) Vohra, V.; Kawashima, K.; Kakara, T.; Koganezawa, T.; Osaka, I.; Takimiya, K.; Murata, H. Efficient Inverted Polymer Solar Cells Employing Favourable Molecular Orientation. *Nat. Photonics* **2015**, *9*, 1–5.

(43) Nelson, J.; Kwiatkowski, J. O. E. J.; Kirkpatrick, J.; Frost, J. M. Modeling Charge Transport in Organic Photovoltaic Materials Introduction. *Acc. Chem. Res.* **2009**, *42*, 1768–1778.

(44) Stoll, S.; Schweiger, A. EasySpin , a Comprehensive Software Package for Spectral Simulation and Analysis in EPR. *J. Magn. Reson.* **2006**, *178*, 42–55.

(45) Frisch, M. J.; Trucks, G. W.; Schlegel, H. B.; Scuseria, G. E.; Robb, M. A.; Cheeseman, J. R.; Scalmani, G.; Barone, V.; Mennucci, B.; Petersson, G. A.; et al. Gaussian 09, Revision B.01. *Gaussian 09, Revision B.01, Gaussian, Inc., Wallingford CT.* 2009.

(46) Neese, F. The ORCA Program System. *WIREs Comput Mol Sci* **2012**, *2*, 73–78.

(47) Visser, J.; Groenen, E. J. J. The Fine-Structure in the Lowest Triplet State of C_{60} and C_{70}. *Chem. Phys. Lett.* **2002**, *356*, 43–48.

(48) Sinnecker, S.; Neese, F. Spin - Spin Contributions to the Zero-Field Splitting Tensor in Organic Triplets, Carbenes and Biradicals: A Density Functional and Ab Initio Study. *J. Phys. Chem. A* **2006**, *110*, 12267–12275.

CHAPTER 5. DYE-rGO SENSITIZER FOR TiO_2

Dye-sensitized solar cells (DSSC) are based on photosensitization of TiO_2 by small molecular chromophores, that absorb light and inject electrons in the conduction band of the semiconductor (see Chapter 1). This technology reached certified power-conversion efficiencies around 12% and thus it is on the same level of bulk heterojunction solar cells based on polymeric materials[1,2].

Triphenylamine-based dyes (TPAs) are the most important organic chromophores that have been employed as sensitizers in the so-called *metal-free* DSSCs, where they are used as alternative to Ru complexes that were originally developed as outstanding sensitizers for TiO_2[3,4]. The reasons for TPAs success are related to their strong electron-donating ability, due to the low ionization potential, the good hole-transport, and the non-planar structure, that hampers dye-aggregation, which is known to worsen DSSCs performances by virtue of intermolecular excited state quenching[5]. These characteristics encouraged the use of TPAs as donor moieties in D-π-A dyes, where a conjugated bridge links the TPA to an acceptor group that also acts as anchoring group for the TiO_2 surface[6].

Graphene emerged in the 2000s as a 2D-material with fascinating properties[7]. Several features make it attractive for the application in energy-conversion devices: the excellent electron mobility (approaching 10^4 cm^2 V^{-1} s^{-1} at room temperature[8]), the chemical stability, the large surface area, the flexibility and the broad absorption range[9]. Unfortunately, it is not so easy to produce graphene on a large scale. Therefore, graphene-related materials are more widely used[10]. Among these, reduced graphene oxide (rGO) stands out as a good compromise between graphene electronic properties and ease of production, being obtained by chemical reduction of graphene oxide derived from graphite[11]. Reduction of graphene oxide resulting in rGO is incomplete, leading to the presence of hydroxy and carboxy substituents in the resulting material. So far, rGO has been employed in DSSC electrodes as a good alternative to ITO and FTO transparent electrodes as well as to the Pt counter electrode[12] and it was used in blend with TiO_2 to improve its conductivity[13]. Several examples of the use of rGO in photoactive materials, rather than in electrodes, can be found in the field of Bulk-Heterojunction Solar Cells (BHJSC), where it was mainly used as electron acceptor in blends with conjugated donor polymers[14,15]. A covalent rGO-metallopolymer hybrid was developed by Fang et al.[16] exhibiting enhanced PCE when blended with PCBM compared to the ungrafted polymer. More generally, the concept of a hybrid material, in which an organic dye is covalently bound to rGO sheets, has been explored in the last few years, showing positive effects from the presence of rGO, such as the enhanced conductivity and the greater stability of the hybrid material[17,18].

Moved by these premises, the group of Prof. Menna at this University synthesized a TPA-based dye-rGO hybrid to be used as sensitizer for TiO_2 in DSSCs, in which the dye is covalently linked to rGO (see Figure 5.1). This covalent dyad was intended to be a model system representative of a new kind of hybrid dye materials that could provide improved conductivity and stability in the dye-sensitized solar cell. To probe the properties of this new kind of material we performed a spectroscopic study based mainly on EPR spectroscopy.

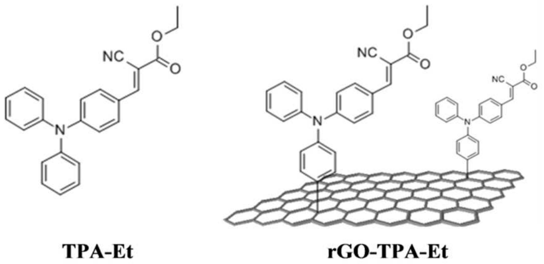

Figure 5.1 Chemical structures of the dye (TPA-Et) and the hybrid material (rGO-TPA-Et).

The dye is an ethyl cyanoacrylate-functionalized triphenylamine, and it is the first triphenylamine-based molecule introduced as sensitizer for the application in DSSCs[19]. The cyano-acrylic group plays both the role of anchoring group and electron-acceptor moiety, providing efficient electron injection into the TiO_2 semiconductor[3]. Although the anchoring group is usually used in the carboxylic acid form, the ethyl ester derivative was chosen for our study due to its easier processability, in particular the possibility of obtaining dispersions of the corresponding hybrid in organic solvents, making the spectroscopic characterization more accessible. The results that we obtained indeed demonstrate that even the ester group enables a strong interaction with the inorganic semiconductor.

The degree of functionalization of the rGO with TPA-Et molecules was determined from a thermogravimetric (TGA) analysis and it is approximately 1/62, meaning that one TPA-Et residue is present on average for every 62 carbon atoms of the rGO backbone.

In this Chapter the results of the EPR and optical spectroscopy experiments will be presented. The characterization of the TPA-Et dye radical cation will be presented first, followed by the investigation of the rGO-TPAEt hybrid, either alone or adsorbed on TiO_2.

5.1 TPA-Et radical cation characterization

The radical cation of the TPA-Et dye was studied before moving to the investigation of the dye-rGO hybrid, in order to obtain the EPR spectrum of the cation that we expected to form in the photoexcited hybrid/TiO_2 blend and to analyze its spin distribution.

The radical was obtained by chemical oxidation using the hypervalent iodine oxidant [bis(trifluoroacetoxy)iodo]benzene (PIFA), which is known to efficiently oxidize aromatic compounds via single-electron transfer[20] (Figure 5.2).

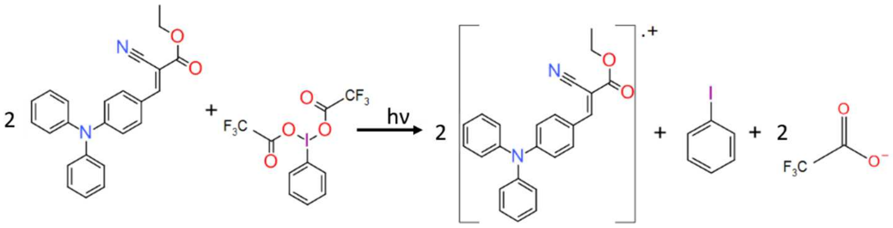

Figure 5.2 Reaction scheme for the oxidation of TPA-Et using PIFA

The radical cation generation was efficiently enhanced by continuous visible light illumination of the solution. In these conditions, a strong CW-EPR spectrum was recorded both at ambient temperature and in the frozen solution at 130 K (Figure 5.3). Both spectra are broadly structured into three lines centered at g=2.0028, stemming from the hyperfine interaction between the electron spin and a ^{14}N nucleus (having nuclear spin $I = 1$). The spectral fitting of the frozen solution spectrum (Figure 5.3 A) was obtained by considering the interaction with this nucleus and including the hyperfine anisotropy, resulting in a tensor with principal values A_x = 0.7 G, A_y = 5 G, A_z = 21.5 G. Further smaller couplings with other nuclei are unresolved in the frozen solution due to inhomogeneous broadening. However, they are recovered in the spectrum recorded at ambient temperature (Figure 5.3 B), since the linewidth is reduced as all anisotropies are averaged out in the liquid solution phase. Indeed, the EPR spectrum of the solution shows a finer structure in addition to the three-line pattern, that is attributable to the hyperfine coupling with the hydrogen nuclei and the cyano-group nitrogen. The unresolved superposition of many lines makes it difficult to extract the hyperfine constants of all the coupled nuclei. However, a reasonable estimate of the isotopic hyperfine constants of the aromatic hydrogens, assuming an almost symmetrical spin density distribution among the three aromatic rings, could be achieved (see Table 5.1), leading to the spectral simulation reported in Figure 5.3 B.

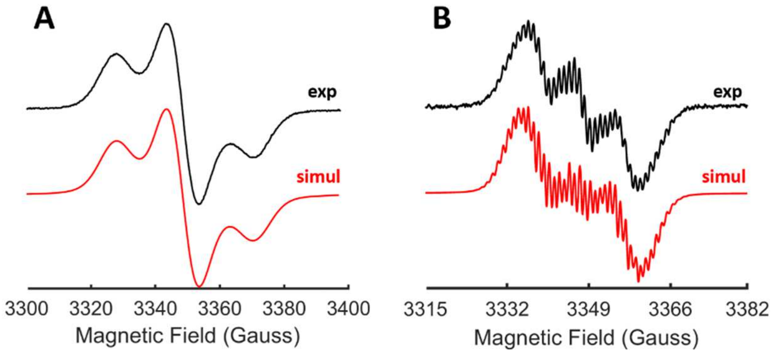

Figure 5.3 Black lines: experimental CW-EPR spectra of the TPA-Et radical cation in toluene. (A) frozen toluene solution, T=130 K; (B) liquid toluene solution, T= 298 K. Red lines: simulated spectra using the parameters listed in Table 5.1.

DFT calculations on the TPA-Et radical cation were performed to support the experimental hyperfine data and to correlate them to the spin-density distribution inside the molecule. The B3LYP/6-31G(d) method was used both for the geometry optimization and for the single-point energy calculation, following a published computational study showing that this method provides better prediction of the EPR parameters of N-containing aromatic radicals compared to higher levels of theory[21]. The results showed excellent agreement with the experimental a_{iso} values (see Table 5.1) and predicted that the 90.5% of the spin-density of the TPA-Et$^{\cdot+}$ radical is located on the TPA portion, as shown in the spin-density isosurface plot reported in Figure 5.5. Thus, the nitrogen atom with the largest hyperfine coupling coincides with the aminic nitrogen. The methine proton and the cyano ^{14}N have consistently lower a_{iso} values, due to the scarce electron delocalization over this portion of the molecule.

Such a spin-density distribution is expected to be beneficial for the efficiency of electron-injection, since the anchoring group provides spatial separation between the spin and the TiO_2 surface, hindering the back-electron transfer from the semiconductor to the oxidized sensitizer.

An analogous calculation was performed to calculate the spin-density in the radical cation of the rGO-TPA-Et hybrid. For this purpose, the rGO-TPA-Et was modeled as a TPA-Et moiety bearing a methyl group with three vinyl substituents, in *para*-position of one phenyl ring, mimicking the interaction with rGO sp^2 carbon atoms. This model was already employed in another study on a similar dye-rGO hybrid and it was shown to be consistent enough to rule out the contribution of the carbon nanostructure to the molecular orbitals and energy levels of the covalently bound chromophore[22,23].

Table 5.1 Experimental isotropic g factor and hyperfine coupling constants derived from the simulation of the TPA-Et radical cation EPR spectrum in solution and calculated hyperfine constants for both the TPA-Et and the rGO-TPA-Et radicals. The experimental values are given with an estimated error of about ±0.05 Gauss.

		g_{iso}	**$\lvert a_{iso} \rvert$ (Gauss)**				
			^{14}N amine	^{14}N cyano	^{1}H *para*	^{1}H *ortho*	^{1}H *meta*
TPA-Et$^{\bullet+}$	Exp	2.0028	8.5	1.0	2.89	2.19	1.26
TPA-Et$^{\bullet+}$	Calc	2.0031	7.74	0.50	2.83^{a}, 2.79^{a}	1.82^{a}, 1.77^{a} 2.12^{b}, 2.22^{b}	1.05^{a}, 1.06^{a} 1.34^{b}, 1.24^{b}
rGO-TPA-Et$^{\bullet+}$	Calc	2.0031	7.56	0.43	2.55	1.67^{a}, 2.03^{b} 2.21^{c}, 1.61^{c}	1.05^{a}, 1.29^{b} 1.05^{c}, 0.94^{c}

[a] Hydrogens in the unsubstituted aromatic rings; [b] Hydrogens in the phenyl ring linked to the cyanoacrylic group; [c] Hydrogens in the aromatic ring attached to rGO.

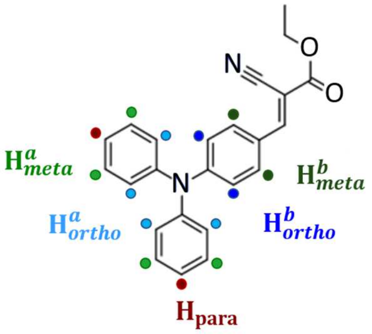

Figure 5.4 TPA-Et molecule with labeled protons.

The calculation of the spin-density on the radical cation of the model rGO-TPA-Et system revealed no major variations of the spin-density distribution with respect to the TPA-Et$^{\bullet+}$ radical, since only little spin-delocalization on the vinyl groups occurs (Figure 5.5 B). This is highlighted by the calculated isotropic hyperfine couplings that are only slightly reduced compared to the dye radical. Therefore, we expect the EPR signal of the oxidized rGO-TPA-Et hybrid to have essentially the same shape of the TPA-Et$^{\bullet+}$ spectrum characterized above.

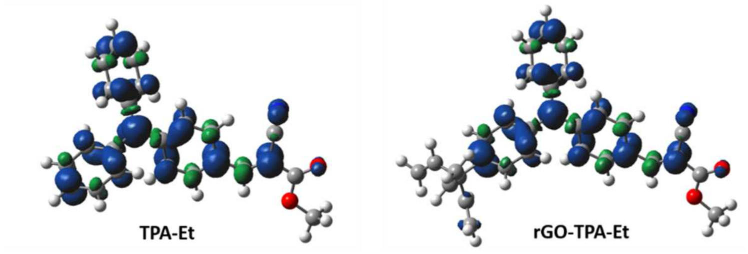

Figure 5.5 Spin density isosurface plot of TPA-Et$^{\cdot+}$ and rGO-TPA-Et$^{\cdot+}$ (isodensity value of 0.002 $e^{-}a_0^{-3}$).

In order to get more information on the hyperfine couplings in the TPA-Et$^{\cdot+}$ radical, we applied HYSCORE spectroscopy, a high resolution two-dimensional technique (see Chapter 2).

The HYSCORE spectra of the TPA-Et solution with PIFA were acquired at three τ values and then summed to avoid blind-spot effects. The magnetic field was set at the value of maximum intensity of the EDEPR spectrum of the radical. The resulting HYSCORE spectrum is reported in Figure 5.6.

The cross-peaks in the (-,+) quadrant, arising from nuclei with a strong hyperfine coupling, are separated by 4.2 MHz, which corresponds to 4 times the nuclear frequency of the ^{14}N nucleus at the magnetic field of the experiment (3450 Gauss). Therefore, these peaks can be identified as correlation peaks between the two double-quantum transitions in the α and β electron spin manifolds. Considering that the aminic nitrogen was shown above to have a huge hyperfine coupling (A_z = 21.5 G, corresponding to 60 MHz), it cannot give rise to HYSCORE signals in the explored frequency region. As a result, the detected ^{14}N peaks likely arise from the cyano-group nitrogen. A precise determination of hyperfine constants from the spectral simulation is however hampered by the high number of parameters, namely the isotropic coupling constant a_{iso}, the dipolar tensor A_{dip}, the nuclear quadrupolar tensor and their mutual orientation.

In the (+,+) quadrant two sets of cross peaks are present, belonging to weakly coupled nuclei. The first is centered at 3.8 MHz, corresponding to the nuclear frequency of ^{13}C, and the second at 14.7 MHz, which is the nuclear frequency of ^{1}H. The ^{13}C cross peaks, very weak because of the low natural abundance of the isotope, are separated by 4.2 MHz (1.5 G), meaning that there are carbon nuclei with this hyperfine coupling constant. Proton cross peaks are elongated ridges due to the presence of a high number of ^{1}H nuclei with different hyperfine tensors, as highlighted by the CW-EPR analysis. The diagonal peak at 13.8 MHz is due to very weakly coupled ^{19}F nuclei, belonging to the trifluoroacetate molecules produced after PIFA reduction, that likely act as counterions for the TPA-Et$^{\cdot+}$ radical cation.

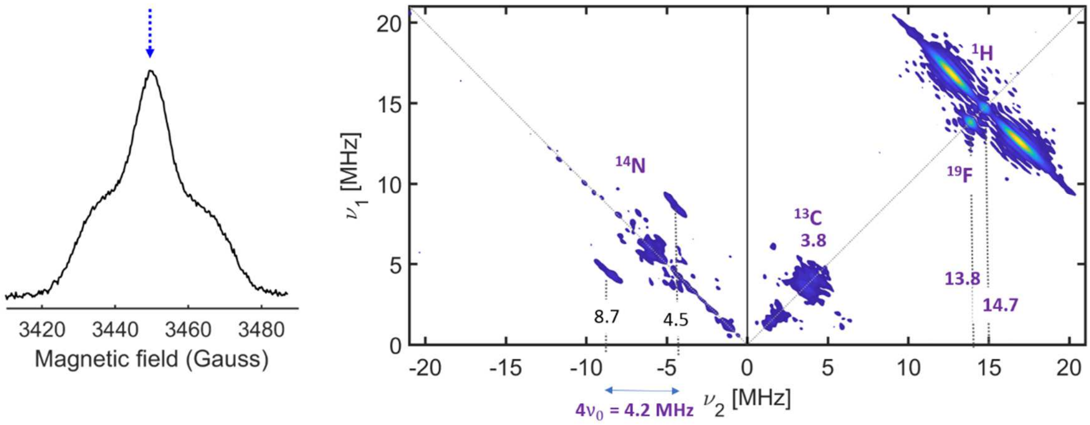

Figure 5.6 EDEPR (left) and HYSCORE spectra (right) of the TPA-Et$^{\cdot+}$ radical in toluene solution (T= 40 K), obtained by oxidation of TPA-Et with PIFA.

The spectra of the TPA-Et$^{\cdot+}$ radical reported in Figure 5.3 were obtained from a 1 mM solution using an excess of PIFA. In more concentrated solutions the CW-EPR spectrum shown in Figure 5.7 was detected. It is composed of 5 lines that can be explained as effect of the hyperfine coupling of the unpaired electron with two equivalent ^{14}N nuclei, sharing the spin density in an almost symmetrical structure i.e. a dimeric radical. This hypothesis is supported by the value of the isotropic ^{14}N coupling constant measured from the spectrum, that is 4.1 G, which is almost exactly half the value in the monomer, indicating a distribution of the unpaired electron into an orbital which is extended over two TPA units. Further confirmation of the formation of a dimer is given by old EPR data reported in literature, regarding the oxidized unsubstituted triphenylamine, showing a very similar dimeric spectrum and a similar ^{14}N hyperfine constant, that were attributed to the N,N,N',N'-tetraphenyl benzidine radical cation, originating from the reaction between two triphenylamine radicals forming the tetraphenyl benzidine that is subsequently easily oxidized[24]. Following this report, we assigned our signal to the analogous dimeric radical of the TPA-Et (see Figure 5.7).

Considering such a tendency of TPAs radicals to dimerize, we suggest that the grafting of the dye on rGO can be beneficial for device performance as the immobilization of TPA-Et may prevent the self-dimerization and therefore the aging of the dye under operating conditions in photovoltaic devices. Moreover, the covalent bonding of TPA-Et on rGO avoids the formation of aggregates of the dye that might decrease the photovoltaic performances.

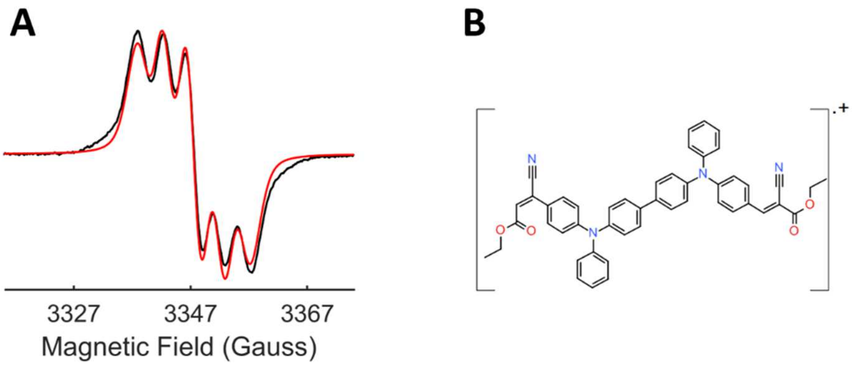

Figure 5.7 A: CW-EPR spectrum of the dimeric radical of TPA-Et at T=298K (black line) with the simulation (red line); B: proposed structure for the radical.

5.2 rGO-TPA-Et characterization

The spectroscopic characterization of rGO-TPA-Et included optical spectroscopy measurements, that were performed by Prof. M. Loi group at the University of Groningen, and Light-induced EPR spectroscopy experiments.

The results of UV-Vis absorption, steady state photoluminescence (ST-PL) and time-resolved photoluminescence experiments (TR-PL) are reported in Figure 5.8, and compared to the results on the model TPA-Et dye.

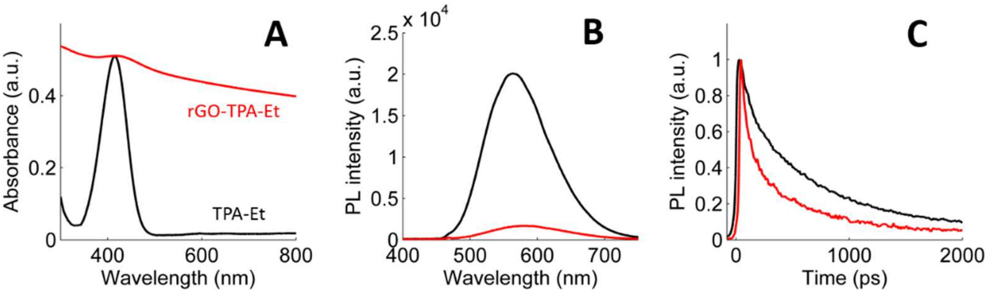

Figure 5.8 A: UV-Vis absorption spectra of the pristine TPA-Et dye (black) and of the rGO-TPA-Et covalent dyad (red); B: steady state photoluminescence spectra of the iso-absorbing solutions of the free dye (black) and of the rGO-TPA-Et (red); C: corresponding time-resolved photoluminescence spectra.

The absorption features of the covalent dyad are composed of two contributions: a continuous band spreading from the UV to the NIR range due to rGO absorption and a band emerging in the visible range corresponding to the absorption by the TPA-Et dye. The dyad has a maximum at 409 nm, whereas the free dye shows a maximum at 406 nm. This 3 nm red shift of the dye absorption in the hybrid is a clear proof of the covalent binding of the molecule to the carbon nanostructure, as was demonstrated in previous studies[22,25]. The ST-PL of the iso-absorbing solutions of the hybrid and the free dye was measured at 400 nm photoexcitation and shows a pronounced quenching of the photoluminescence of TPA-Et when bound covalently to rGO. This behavior indicates that processes of energy or electron transfer might take place from the dye to the reduced graphene oxide upon photoexcitation. The TR-PL further confirms this observation with a faster PL decay from the functionalized rGO sample compared to the pristine TPA-Et dye (Figure 5.8 C). The PL decay was fit with a biexponential decay function: $y(t) = A_1 \exp(t/\tau_1) + A_2 \exp(t/\tau_2)$ where the lifetimes are represented by τ_n and their corresponding weights are represented by A_n. The pristine dye exhibits photoluminescence decay with lifetimes of 158 ps/1012 ps respectively. When it is attached to rGO, the photoluminescence lifetime is reduced to 83 ps/831 ps.

The toluene dispersion of rGO-TPA-Et was studied by CW-EPR under white light illumination in the attempt to clarify the nature of the observed photoluminescence quenching. Indeed, both energy-transfer or electron-transfer are plausible processes and both of them were already identified in other chromophore/graphene systems[17]. However, no light-induced EPR signals could be detected for the hybrid either at ambient temperature or at T=130 K. This result can be explained with either a very low efficiency of photoinduced electron transfer from TPA-Et to rGO or by an electron transfer followed by a fast charge recombination, extinguishing the radical species in a period of time which is far below the time resolution of LEPR, making them undetectable. Recently, by means of picosecond transient absorption spectroscopy, Majima et al. showed that electron transfer occurs on a picosecond time-scale in a dye-GO hybrid, and also demonstrated that the back electron transfer occurs within 200 ps[25]. These data seem to suggest that also in our system electron transfer from TPA-Et to rGO likely occurs, but it is followed by rapid recombination. Such an hypothesis is consistent with the energy levels arrangement of the two components as the LUMO of the dye is higher in energy than the rGO workfunction: the rGO workfunction is estimated to be around -4.4 eV[10], while the dye LUMO is close to -2.18 eV according to a DFT calculation on the TPA-Et molecule[26].

5.3 rGO-TPA-Et/TiO_2 characterization

The photophysics of the rGO-TPA-Et hybrid adsorbed on TiO_2 was probed by Light-induced EPR spectroscopy and compared to the blend of the TPA-Et dye with TiO_2.

Before proceeding to show these results, it is necessary to make a digression on the photophysical properties of the TiO_2 nanopowder that was used.

Pure TiO_2 does not absorb light in the visible range due to its large bandgap of 3.2 eV, corresponding to an absorption edge of approximately 390 nm. On the other hand, doped TiO_2 can display visible absorption thanks to intrabandgap localized states, from which electrons can be promoted to the conduction band of the oxide. This is the case of Nitrogen-doped TiO_2, a material that was developed for photocatalytic applications and occasionally employed in DSSCs[27], that was used in our study.

A series of paramagnetic defects are known to be present in N-doped TiO_2 nanopowders, and some of them were very well characterized through the combination of EPR and computational methods by the groups of Giamello and Di Valentin[28,29,30]. Among these defects, there is a subset consisting in single-nitrogen atom impurities, with still unknown precise chemical nature, that are located in the bulk of the material (hereafter labelled as $N_b^{\cdot}$ following ref. [28,29,30]). These impurities were shown by DFT to introduce localized states a few tenths of eV above the valence band of the semiconductor, and EPR spectroscopy proved that they are involved in the visible sensitization of the material. The authors proposed the presence of both $N_b^{\cdot}$ paramagnetic impurities and doubly occupied N_b^{-} diamagnetic centers inside the solid, both capable of promoting an electron in the conduction band upon photoexcitation in the visible range, forming N_b^{+} and $N_b^{\cdot}$ species respectively:

$$\dot{N_b} \xrightarrow{h\nu} N_b^{+} + e^{-}(CB) \tag{1}$$

$$N_b^{-} \xrightarrow{h\nu} \dot{N_b} + e^{-}(CB) \tag{2}$$

The N_b^{-} defects are more abundant in the solid, due to their higher stability predicted by computational methods[28]. This makes reaction 2 preferred, resulting in an increasing concentration of $N_b^{\cdot}$ centers under irradiation. This explained the light-induced EPR signal of $N_b^{\cdot}$ centers.

By performing LEPR experiments on our N-doped TiO_2 we detected the same signal of $N_b^{\cdot}$ reported in the cited studies (see Figure 5.9), and observed its increase under illumination attributable to reaction 2.

The spin-hamiltonian parameters of $N_b^{\cdot}$ were determined from the simulation (see Table 5.2) and they are very close to the ones reported in literature.

Table 5.2 Spin-Hamiltonian parameters of $N_b^{\cdot}$.

g_1	**g_2**	**g_3**	**A_1 (G)**	**A_2 (G)**	**A_3 (G)**
2.0051	2.0042	2.0027	2	3.6	32

As will be shown in the following, the use of N-doped TiO_2 offered the possibility to have a spectroscopic signature of the direction of the electron transfer, and since the amount of doping is in the ppb scale (see the Experimental section for details on the materials), we believe it does not affect significantly the photophysics of the material. Thus, we are confident that our results are valid for pure TiO_2 as well, which is commonly used in DSSCs.

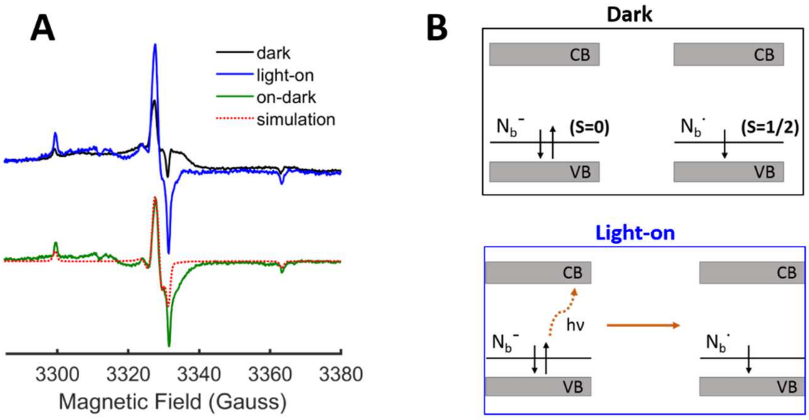

Figure 5.9 A: CW-EPR spectra of the N-doped TiO_2 nanopowder (T = 130 K); B: schematic representation of the nitrogen impurities in the solid, adapted from ref[28].

The rGO-TPA-Et/TiO_2 sample was studied in parallel to TPA-Et/TiO_2, taken as a reference system. The light-induced EPR spectra of these samples are reported in Figure 5.10 A. The spectra are substantially different from the photoinduced spectrum of the N-doped TiO_2 (see Figure 5.9). In the case of the TPA-Et/TiO_2 sample, the signal clearly resembles the one of the TPA-Et$^{\cdot+}$ radical produced in solution by chemical oxidation (see Figure 5.3 A), differing from it for the less pronounced outer lines. For the rGO-TPA-Et/TiO_2 sample, the outer lines of the photoinduced signal are even broader. However, the assignment of the signal to the radical cation of the TPA-Et residue follows from the evaluation of the g-factor, which corresponds to the one of the TPA-Et$^{\cdot+}$ radical. Thus, we deduced that efficient electron transfer with formation of a stable dye radical cation occurs in both the TPA-Et/TiO_2 and the rGO-TPA-Et/TiO_2 systems.

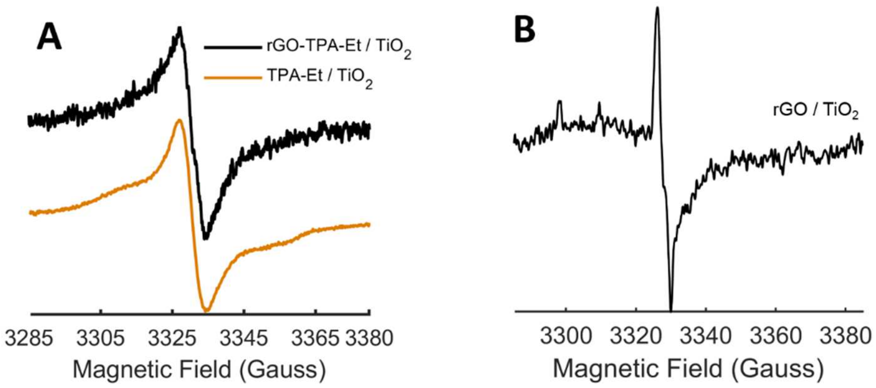

Figure 5.10 A: Light-induced EPR spectra (T = 130 K) of rGO-TPA-Et/TiO_2 and TPA-Et/TiO_2 (normalized); B: Light-induced EPR spectrum of rGO/TiO_2.

As a control experiment, we performed Light-induced EPR on a rGO/TiO_2 sample and obtained the spectrum shown in Figure 5.10 B, that coincides with the photoinduced signal of the $N_b^{\cdot}$ centers in the titanium dioxide (see Figure 5.9). This confirms that the signal detected for rGO-TPA-Et/TiO_2 originates from the photoactivity of the dye molecule and not from that of bare rGO.

The different lineshape between the TPA-$Et^{\cdot+}$ radical signal observed in the dye/TiO_2 systems and in the solution of the free dye can be rationalized according to either a static or a dynamic phenomenon. In the case of the TPA-Et/TiO_2 sample some degree of dye aggregation can be inferred, probably leading to a distribution in the hyperfine splittings due to the presence of radicals with a different degree of spin delocalization. This causes the broadening of the EPR spectral lines. Furthermore, the delocalization of the spin density over more than one TPA molecules in the aggregates causes the collapse of the spectrum towards the central line, due to the reduction of the hyperfine splittings.

Dye aggregation can be excluded for the rGO-TPA-Et/TiO_2 sample, since the TPA-Et residues are well separated over the graphene network, as demonstrated by the 1/62 functionalization degree determined from TGA. One possible explanation for the EPR lineshape, characterized by the small contribution of the outer lines, may be the reduction of the hyperfine interaction with the amine nitrogen, due to partial delocalization of the spin-density over the graphene network. However, we can exclude this hypothesis on the basis of our DFT calculation on the model rGO-TPA-Et radical cation (see section 5.1), predicting that the extent of spin delocalization over the carbon nanostructure is small, causing only minor reduction of the hyperfine constants. Therefore, we think that, in the case of the hybrid adsorbed on TiO_2, the lineshape variations with respect to the free TPA-Et radical might be related to dynamical processes. Although no direct hopping of the unpaired electron between dyes in the hybrid is expected, due to the distance between adjacent dyes, a charge transfer mechanism mediated by the π orbitals of graphene could be active, that can effectively transfer the charge between different grafted dyes. The electron jump between different TPA-Et residues tends to average out both isotropic and dipolar hyperfine interactions. The first because of the random spin state of the nuclei in the sites among which the electron jumps, the second because of the different orientation of the molecules[31].

The intensity of the LEPR spectrum of the hybrid adsorbed on TiO_2 is lower compared to the intensity found for the dye molecule in the same system (as can be seen from Figure 5.11). We attributed this to the difficulty of obtaining fine dispersions of the hybrid, limiting the dye loading of the TiO_2 semiconductor. As pointed out in a previous study on a similar system[22], this drawback may be eliminated by using rGO with smaller dimensions, that should lead to more easily dispersible hybrids, interacting more efficiently with TiO_2.

From inspection of the light-induced spectra reported in Figure 5.10 A, it is evident, in the stained TiO_2 samples, the absence of photoinduced signal due to the photogeneration of $N_b^{\cdot}$ paramagnetic centers. The EPR spectra of the stained and pristine TiO_2 (reported in Figure 5.11) have comparable intensities, therefore, if the signal of pristine TiO_2 due to the $N_b^{\cdot}$ centers was present in the stained-TiO_2, it should be visible in the spectra.

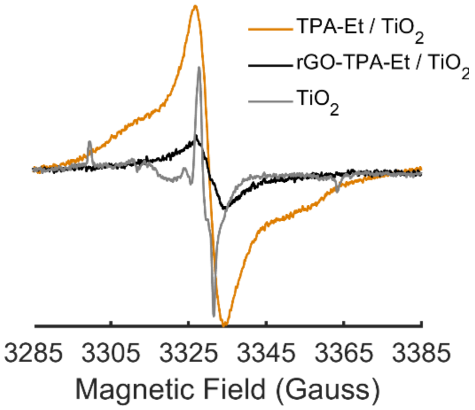

Figure 5.11 Superposition of the LEPR spectra of pristine and stained TiO_2 (true intensities).

These considerations lead to deduce that the light-induced signal of $N_b^{\cdot}$ defects, that is normally observed in N-doped TiO_2, vanishes when the semiconductor nanopowder is stained with the dye molecules. We explain this result by noting that the localized $N_b^{\cdot}$ defects can act as traps for the electrons injected into the TiO_2 conduction band by the photoexcited dye. In this way they become diamagnetic and therefore EPR silent (reaction 3).

$$N_b^{\cdot} + e^- \rightarrow N_b^- \qquad (3)$$

This provides us with the indication that the acceptor for the electrons transferred from the TPA-Et dye, either free or grafted onto rGO, is the TiO_2 semiconductor.

As pointed out in section 5.2, the electron-transfer from the dye towards rGO is difficult to be observed by EPR, due to the fast recombination rate, therefore we cannot rule it out. However, the EPR results show that the interaction of the hybrid with titanium dioxide is strong enough to efficiently compete with the tendency of the reduced graphene oxide to quench the excited state of the dye, leading to the photoinduced injection of electrons from the dye to the conduction band of the semiconductor. This directional, efficient electron transfer from the dye to the TiO_2 is the desired effect for the application of dye-rGO systems in dye-sensitized solar cells.

In analogy to the characterization presented in section 5.1 on the dye radical cation obtained by chemical oxidation, we performed HYSCORE experiments on the TPA-Et$^{\cdot+}$ radical formed in the TPA-Et/TiO_2 system under photoexcitation, in order to study its spin-density distribution. The same could not be done for rGO-TPA-Et/TiO_2 due to the low intensity of the radical signal in this case.

The HYSCORE spectrum, reported in Figure 5.12, was acquired at the central field of the EDEPR spectrum of the radical, and results from the sum of three HYSCORE spectra acquired at different τ values. The (-,+) quadrant is populated by the peaks attributed to the cyano-group nitrogen, having the same position and shape observed for the TPA-Et$^{\cdot+}$ radical in frozen solution. This reveals that the spin-density distribution over the acceptor group remains unaltered when the dye molecule is anchored to TiO_2. Considering that DFT calculations on the free TPA-Et$^{\cdot+}$ radical showed that only minor spin delocalization on the cyano group occurs, this conclusion seems to be valid also for the dye adsorbed on TiO_2 on the basis of the HYSCORE results. Therefore, this result provides evidence that the anchoring group indeed acts as spacer between the semiconductor and the TPA portion of the dye, where the spin (and hence the positive charge) is located.

The same behavior is shown by the ^1H cross-peaks in the (+,+) quadrant, that are nearly identical to the peaks observed in the dye frozen solution. These peaks are a superposition of signals belonging to the numerous hydrogen nuclei in the molecule, with a major contribution of the aromatic protons since the spin density over the cyanoacetic group is much smaller.

Considering the hypothesized dye aggregation, causing a distribution of hyperfine interactions in the radical formed in the TPA-Et/TiO_2 sample, that could explain the CW-EPR spectral shape deviating from the shape of the radical in solution, we expected to observe an effect in the HYSCORE spectrum. This was especially expected for the aromatic nuclei, since aggregation is predicted to involve mainly this part of the molecule (as the anchoring group is closer to the TiO_2 surface and therefore more hindered). However, the hyperfine distribution owing to aggregation is likely incorporated into the broadened lineshape of the proton HYSCORE peaks due to the unresolved superposition of signals. Unfortunately, the aminic N cannot be probed by HYSCORE due to its huge hyperfine coupling, though its HYSCORE signals would be useful to confirm the hypothesis of dye aggregation.

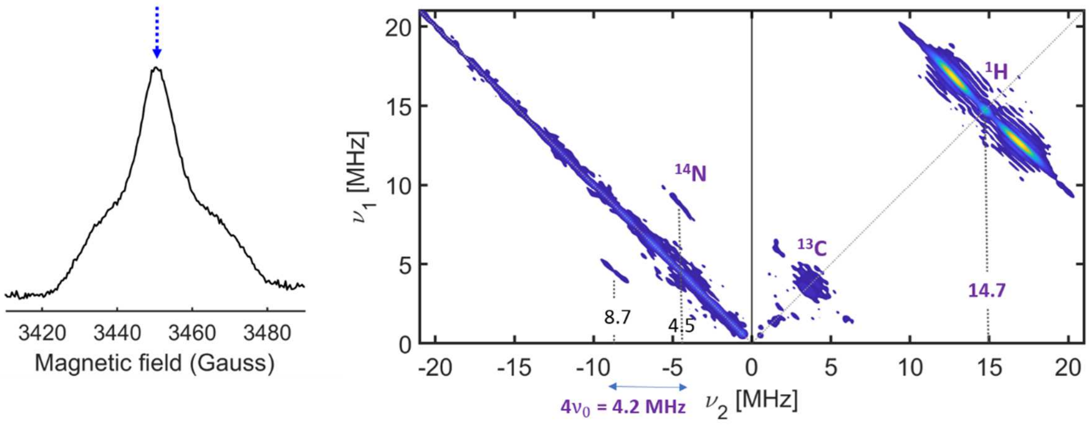

Figure 5.12 EDEPR (left) and HYSCORE spectra (right) of the TPA-Et$^{\bullet+}$ radical formed upon illumination of TPAEt/TiO_2 (T=40K).

5.4 Conclusions

This Chapter presented the spectroscopic investigation of a new kind of photosensitizer for TiO_2, based on the small TPA-Et dye molecule covalently bound to rGO sheets.

The characterization of the dye radical cation obtained through chemical oxidation of the molecule in solution was reported first. The primary aim of this analysis was the identification of the EPR spectrum of the cation in order to allow for recognition of its formation in the rGO-TPA-Et hybrid adsorbed on TiO_2. This was achieved *via* Light-induced CW-EPR on the frozen solution, showing a signal dominated by the hyperfine interaction of the unpaired spin with the amine nitrogen atom. Liquid solution CW-EPR, DFT calculations and HYSCORE experiments were then used to gain knowledge about the spin-density distribution inside the radical, that was found to be concentrated in the amine region of the molecule. This was confirmed by HYSCORE experiments performed on the photoinduced radical formed in the TPA-Et/TiO_2 sample upon electron transfer from the dye to the semiconductor, demonstrating that the anchoring group provides physical separation between the unpaired electron and the TiO_2 surface, helping reducing recombination.

The rGO-TPA-Et dispersion was studied with both EPR and fluorescence spectroscopy, from which a quenching of the excited state of the dye was found for the molecule grafted on rGO. EPR could not find any signature of electron transfer, but, based on previous studies performed with ultrafast optical techniques, we hypothesized that an electron transfer from the dye to rGO may occur, followed by a very fast recombination that is far below LEPR detection times.

For the sample in which rGO-TPA-Et was adsorbed on TiO_2, EPR could demonstrate that a photoinduced electron transfer from the dye moiety towards the semiconductor occurs. For this scope N-doped TiO_2 was used, that provided the spectroscopic evidence of the direction of the electron transfer, thanks to the presence of paramagnetic nitrogen defects that act as traps for the electrons injected into TiO_2, becoming diamagnetic and therefore EPR silent. This showed that the interaction with TiO_2, resulting in electron injection into the oxide, efficiently competes with the dye excitation quenching by rGO.

In conclusion, our results demonstrate that the rGO-dye architecture is applicable to dye-sensitized solar cells as the main requirement for TiO_2 sensitization, i.e. electron injection in the semiconductor conduction band, is fulfilled. The presence of rGO in the sensitizer is expected to be beneficial due its high conductivity. Furthermore, rGO can be expected to be useful to aid the regeneration of the neutral state of the dye since its work-function lays above the energy of the dye HOMO. The application of a very similar dye to DSSCs was already tested[22], showing promising performances. However, the limitation in dye loading related to the difficulty in obtaining fine dispersions of the hybrid material, was identified as a cause of poorer performance compared to the common TPA-based dyes. To improve the performance of the system and fully exploit its potentialities as photosensitizer for TiO_2, we think that hybrids with a smaller dimension of the rGO sheet should be explored, as they would provide a more efficient interaction with the TiO_2 nanopowder.

5.5 Experimental

The synthesis of TPA-Et and rGO-TPA-Et was done in the group of Prof. Menna, by Dr. Teresa Gatti and Nicolò Canever, who also carried out the characterization of the material by TGA and DLS.

Absorption and photoluminescence spectroscopy experiments were carried out in the group of Prof. Loi at University of Gottingen – The Netherlands.

5.5.1 Materials

All reagents and solvents were purchased from Sigma-Aldrich and used as received. Reduced graphene oxide was purchased from ACS Material, LLC (product no: GnP1L-0.5g) and used as received. The production method, as reported by the supplier, consists in reducing graphene oxide obtained from graphite *via* the Hummer's method, by thermal exfoliation reduction and further hydrogen reduction. Transmission electron microscopy on the reduced graphene oxide flakes showed that they have lateral dimensions between 1 and 2 μm (see ref. [22]).

Titanium dioxide anatase nanopowder (d<25 nm) was purchased by Sigma Aldrich (product no: 637254). The supplier declares a 99.7% purity. In the Certificate of Analysis of the product, a number of elements are listed even with sub-ppm concentration, but there is no mention of the presence of nitrogen. We argue that the concentration of nitrogen may be very low, perhaps in the ppb scale, but enough to be detected by EPR. The producer did not release any detail about the doping procedure.

5.5.2 Synthesis of rGO-TPA-Et

The synthesis of the TPA-Et dye was adapted from a literature procedure[6]. The covalent anchoring of the dye to the surface of rGO was achieved via the diazotization reaction. The diazonium salt derivative of TPA-Et, namely the tetrafluoroborate BF_4^--N_2^+-TPA-Et, was used. The salt was added to a suspension of rGO in 1-cyclohexyl-2-pyrrolidone (CHP), the best solvent to disperse rGO flakes. The mixture was stirred at room temperature for 15', after which methanol was added to precipitate the product. Repeated washings of the resulting material with DMF and methanol ensured the elimination of non-covalently bound TPA-Et molecules.

The effective amount of TPA-Et functionalities covalently attached to rGO was determined *via* a thermogravimetric analysis (TGA), following the procedure described in ref [22]. A Q5000IR TGA (TA instruments) was used under nitrogen, with an isotherm at 100 °C for 10 min followed by heating at 10°C/min rate up to 1000 °C. The resulting functionalization degree is 1/62. The thermogram is reported in the article SI[26].

The average dimension of the rGO-TPA-Et hybrid was determined through Dynamic Light Scattering (DLS) measurements of the dyad dispersed in air-equilibrated DMF, performed with a Zetasizer Nano

S (Malvern Instruments) at 20° C. The analysis furnished a single solvodynamic diameter distribution centered at 460 nm.

5.5.3 Optical spectroscopy

Absorption spectra were registered with a Varian Cary 5000 spectrometer. Steady-state photoluminescence spectra were collected via a spectrometer with a grating of 50 lines per mm and recorded with a Hamamatsu EM-CCD camera sensitive in Vis region. For time-resolved measurements, spectra were collected on a Hamamtsu streak camera working in synchroscan mode (time resolution ~2 ps) with a cathode also sensitive in the Vis region. All spectra were corrected for the response of the setup using a calibrated lamp.

The PL measurements were carried out in quartz cuvettes with 2 mm path length. The rGO-TPA-Et was dispersed in DMF through sonication at low power for few minutes. The excitation source was the second harmonic (approximately 400 nm) of a mode-locked Ti:sapphire laser, delivering 150 fs pulses at a repetition rate of 76 MHz.

5.5.4 EPR spectroscopy

5.5.4.1 Sample preparation

All the samples were studied in EPR quartz tubes (3 mm ID, 4 mm OD). The oxidation of TPA-Et in toluene solution (1 mM) was carried out using an excess of the oxidant (PIFA, Aldrich, used as received). The TPA-Et/TiO_2 sample was prepared by dispersing 100 mg of TiO_2 powder in 3 mL of a TPA-Et solution (1 mM in toluene : MeOH 1:1) and sonicating for two hours. The dispersion was then decanted and the supernatant was removed. The powder was dried under a nitrogen flux and put in the EPR tube that was sealed under vacuum. The same procedure was used for the preparation of the rGO-TPA-Et sample. However, the concentration of the hybrid dispersion was limited by the possibility to obtain a fine and stable dispersion. The resulting concentration of hybrid was approximately 0.2 mg/mL, corresponding to a 0.066 mg/mL (0.18 mM) concentration of the TPA-Et residue. The rGO-TPA-Et/TiO_2 powder was obtained by dispersing 100 mg of TiO_2 powder in 3 mL of the rGO-TPA-Et dispersion.

5.5.4.2 CW-EPR

Light-induced EPR measurements were performed on an X-band Bruker ER200D spectrometer. The photoexcitation of the samples was obtained using the white light from a 300 W Xe lamp, IR filtered and focused into a quartz optical fiber. The resulting irradiation spectral range extends from about

350 nm up to 900 nm, with an intensity of about 50 mW cm^{-2}. EPR spectral simulations were performed using Easyspin[32].

5.5.4.3 Pulse-EPR

Pulse-EPR experiments were performed on a X-band ELEXSYS E580 Bruker spectrometer, equipped with a dielectric resonator inside an Oxford CF900 cryostat. The samples were studied under continuous illumination from the same lamp described above for CW-EPR experiments.

HYSCORE experiments were performed using the pulse sequence $\pi/2–\tau–\pi/2–t_1–\pi–t_2-\pi/2–\tau–$echo with pulse lengths $t_{\pi/2}$=16ns and t_π=32ns. τ values were 168, 200 and 268 ns, t_1 and t_2 were incremented by dt=20 ns leading to a 128×128 data matrix. A four-step phase cycle was used.
The time domain HYSCORE data were processed in Matlab. The baseline was corrected by a 3rd order polynomial and the resulting time traces were apodized using a Hamming window function. The matrix was then zero-filled with 1024 points in both dimensions. The 2D-Fourier transform was applied and the absolute-value spectrum was calculated.

5.6 References

(1) National Renewable energy Laboratory - Efficiency Chart 2018 - https://www.nrel.gov/pv/.

(2) Gong, J.; Sumathy, K.; Qiao, Q.; Zhou, Z. Review on Dye-Sensitized Solar Cells (DSSCs): Advanced Techniques and Research Trends. *Renew. Sustain. Energy Rev.* **2017**, *68*, 234–246.

(3) Wang, J.; Liu, K.; Ma, L.; Zhan, X. Triarylamine: Versatile Platform for Organic, Dye-Sensitized, and Perovskite Solar Cells. *Chem. Rev.* **2016**, *116*, 14675–14725.

(4) O'Regan, B.; Gratzel, M. A Low-Cost, High-Efficiency Solar Cell Based on Dye-Sesitized Colloidal TiO_2 Films. *Nature* **1991**, *353*, 737–739.

(5) Kim, S.; Lee, J. K.; Kang, S. O.; Ko, J.; Yum, J.; Fantacci, S.; Angelis, F. De; Censo, D. Di; Nazeeruddin, K.; Gra, M.; et al. Molecular Engineering of Organic Sensitizers for Solar Cell Applications. *J. Am. Chem. Soc.* **2006**, *128*, 16701–16707.

(6) Hagberg, D. P.; Marinado, T.; Karlsson, K. M.; Nonomura, K.; Qin, P.; Boschloo, G.; Brinck, T.; Hagfeldt, A.; Sun, L. Tuning the HOMO and LUMO Energy Levels of Organic Chromophores for Dye Sensitized Solar Cells. *J. Org. Chem.* **2007**, *72*, 9550–9556.

(7) Geim, A. K.; Novoselov, K. S. The Rise of Graphene. *Nat. Mater.* **2007**, *6*, 183–191.

(8) Novoselov, K. S.; Geim, A. K.; Morozov, S. V.; Jiang, D.; Zhang, Y.; Dubonos, S. V.; Grigorieva, I. V.; Firsov, A. A. Electric Field Effect in Atomically Thin Carbon Films. *Science* **2004**, *306*, 666–669.

(9) Nair, R. R.; Blake, P.; Grigorenko, A. N.; Novoselov, K. S.; Booth, T. J.; Stauber, T.; Peres, N. M. R.; Geim, A. K. Fine Structure Constant Defines Visual Transparency of Graphene. *Science* **2008**, *320*, 1308.

(10) Singh, V.; Joung, D.; Zhai, L.; Das, S. Graphene Based Materials: Past, Present and Future. *Prog. Mater. Sci.* **2011**, *56*, 1178–1271.

(11) Abdolhosseinzadeh, S.; Asgharzadeh, H.; Kim, H. S. Fast and Fully-Scalable Synthesis of Reduced Graphene Oxide. *Sci. Rep.* **2015**, *5*, 10160.

(12) Bonaccorso, F.; Colombo, L.; Yu, G.; Stoller, M.; Tozzini, V.; Ferrari, a C.; Ruoff, R. S.; Pellegrini, V. Graphene, Related Two-Dimensional Crystals, and Hybrid Systems for Energy Conversion and Storage. *Science* **2015**, *347*, 1246501–1246501.

(13) Tang, Y.; Lee, C.-S.; Xu, J.; Liu, Z.; Chen, Z.-H.; He, Z.; Cao, Y.; Yuan, G.; Song, H.; Chen, L.; et al. Incorporation of Graphenes in Nanostructured TiO_2 Films via Molecular Grafting for Dye-Sensitized Solar Cell Application. *ACS Nano* **2010**, *4*, 3482–3488.

(14) Liu, Z.; Liu, Q.; Huang, Y.; Ma, Y.; Yin, S.; Zhang, X.; Sun, W.; Chen, Y. Organic Photovoltaic Devices Based on a Novel Acceptor Material: Graphene. *Adv. Mater.* **2008**, *20*, 3924–3930.

(15) Wang, Y.; Kurunthu, D.; Scott, G. W.; Bardeen, C. J. Fluorescence Quenching in Conjugated Polymers Blended with Reduced Graphitic Oxide. *J. Phys. Chem. C* **2010**, *114*, 4153–4159.

(16) Fang, Z.; Ito, A.; Stuart, A. C.; Luo, H.; Chen, Z.; Vinodgopal, K.; You, W.; Meyer, T. J.; Taylor, D. K. Soluble Reduced Graphene Oxide Sheets Grafted with Polystyrene Brushes as Light Harvesting Antenna for Photovoltaic Applications. *ACS Nano* **2013**, *7*, 7992–8002.

(17) Wang, H. X.; Wang, Q.; Zhou, K. G.; Zhang, H. L. Graphene in Light: Design, Synthesis and Applications of Photo-Active Graphene and Graphene-like Materials. *Small* **2013**, *9*, 1266–1283.

(18) Xu, Y.; Liu, Z.; Zhang, X.; Wang, Y.; Tian, J.; Huang, Y.; Ma, Y.; Zhang, X.; Chen, Y. A Graphene Hybrid Material Covalently Functionalized with Porphyrin: Synthesis and Optical Limiting Property. *Adv. Mater.* **2009**, *21*, 1275–1279.

(19) Kitamura, T.; Ikeda, M.; Shigaki, K.; Inoue, T.; Anderson, N. A.; Ai, X.; Lian, T.; Yanagida, S. Phenyl-Conjugated Oligoene Sensitizers for TiO_2 Solar Cells. *Chem. Mater.* **2004**, *16*, 1806–1812.

(20) Wirth, T. *Hypervalent Iodine Chemistry: Modern Developments in Organic Synthesis* Springer, 2003.

(21) Hermosilla, L.; Calle, P.; García de la Vega, J. M. Modeling EPR Parameters of Nitrogen Containing Conjugated Radical Cations. *RSC Adv.* **2015**, *5*, 62551–62562.

(22) Gatti, T.; Manfredi, N.; Boldrini, C.; Lamberti, F.; Abbotto, A.; Menna, E. A D-π-A Organic Dye – Reduced Graphene Oxide Covalent Dyad as a New Concept Photosensitizer for Light Harvesting Applications. *Carbon N. Y.* **2017**, *115*, 746–753.

(23) Salice, P.; Sartorio, C.; Burlini, A.; Improta, R.; Pignataro, B.; Menna, E. On the Trade-off between Processability and Opto-Electronic Properties of Single Wall Carbon Nanotube Derivatives in Thin Film Heterojunctions. *J. Mater. Chem. C* **2015**, *3*, 303–312.

(24) Bruning, W. H.; Nelson, R. F.; Marcoux, L. S.; Adams, R. N. The Structure of the Iodine-Triphenylamine Charge-Transfer Complex. *J. Phys. Chem.* **1967**, *71*, 3055–3057.

(25) Tachikawa, T.; Cui, S.-C.; Fujitsuka, M.; Majima, T. Interfacial Electron Transfer Dynamics in Dye-Modified Graphene Oxide Nanosheets Studied by Single-Molecule Fluorescence Spectroscopy. *Phys. Chem. Chem. Phys.* **2012**, *14*, 4244.

(26) Guarracino, P.; Gatti, T.; Canever, N.; Abdu-aguye, M.; Loi, M. A.; Menna, E.; Franco, L. Probing Photoinduced Electron-Transfer in Graphene – Dye Hybrid Materials for DSSC. *Phys. Chem. Chem. Phys.* **2017**, *19*, 27716–27724.

(27) Ma, T.; Akiyama, M.; Abe, E.; Imai, I. High-Efficiency Dye-Sensitized Solar Cell Based on a Nitrogen-Doped Nanostructured Titania Electrode. *Nano Lett.* **2005**, *5*, 2543–2547.

(28) Livraghi, S.; Paganini, M. C.; Giamello, E.; Selloni, A.; Di Valentin, C.; Pacchioni, G. Origin of Photoactivity of Nitrogen-Doped Titanium Dioxide under Visible Light. *J. Am. Chem. Soc.* **2006**, *128*, 15666–15671.

(29) Di Valentin, C.; Finazzi, E.; Pacchioni, G.; Selloni, A.; Livraghi, S.; Paganini, M. C.; Giamello, E. N-Doped TiO_2: Theory and Experiment. *Chem. Phys.* **2007**, *339*, 44–56.

(30) Livraghi, S.; Chierotti, M. R.; Giamello, E.; Magnacca, G.; Paganini, M. C.; Cappelletti, G.; Bianchi, C. L. Nitrogen-Doped Titanium Dioxide Active in Photocatalytic Reactions with Visible Light: A Multi-Technique Characterization of Differently Prepared Materials. *J. Phys. Chem. C* **2008**, *112* , 17244–17252.

(31) Carrington, A.; McLachlan, A. D. *Introduction to Magnetic Resonance*; Chapman and Hall: London, 1979.

(32) Stoll, S.; Schweiger, A. EasySpin, a Comprehensive Software Package for Spectral Simulation and Analysis in EPR. *J. Magn. Reson.* **2006**, *178*, 42–55.

CHAPTER 6. DONOR-ACCEPTOR CHARGE-TRANSFER GEL

The field of organic semiconductors is not only limited to π-conjugated polymers since covalent bonds between monomers do not represent a unique strategy for achieving electronic transport in organic systems. Supramolecular interactions between small molecules are also being explored and research in this field demonstrated the feasibility of the idea of *supramolecular electronics*[1].

Non-covalent interactions can be exploited for the self-assembling of small molecules into supramolecular stacks forming functional nanofibers that were shown to be able to transport charge carriers[2]. Hydrogen-bonding, π-stacking, and charge-transfer (CT) interactions between donor and acceptor molecules were successfully used for this scope[3,4], resulting in materials for which photovoltaic properties were demonstrated[5–9].

The interest in such materials is animated by their many attractive properties. The ease of preparation is among the most interesting features, since the supramolecular materials are in most cases prepared from combination of existing molecules by exploitation of their self-assembling abilities and thus avoiding time-consuming synthetic procedures. Furthermore, their optoelectronic properties can be easily tuned by chemical modifications or replacement of the small aromatic components.

The charge-transfer interaction between donor and acceptor molecules is particularly important since it favors charge generation. Self-assembled structures of charge-transfer complexes allow to obtain molecular-scale p-n junctions that can be precisely designed by tuning the intermolecular interactions[4].

In most cases the studied supramolecular materials were in the form of single crystals. However, the last decade has witnessed an increasing interest in the so-called *soft-materials* based on weak intermolecular interactions between small molecules[10,11]. In particular, gel phases[12,13,14] gained increasing attention. They are formed upon self-organization of molecules into one-dimensional arrays forming elongated fibrous structures. Entanglement between fibers then forms a three-dimensional network that traps the solvent. Photocurrent generation was demonstrated for a number of gels obtained by combination of donor and acceptor molecules[15,16,17]. The most appealing feature of supramolecular gels is their straightforward preparation, requiring simple mixing of the small molecular components and heating and cooling. Moreover, they offer peculiar mechanical properties such as flexibility, adaptability to fill any volume of space and the self-recovery ability.

The group of Prof. Miriam Mba at the Department of Chemical Sciences – University of Padova is active in the field of designing supramolecular functional gels. They prepared a gel based on the self-assembling of naphthalene diimide (NDI) and pyrene (Py) molecules, exploiting three kinds of interactions, namely π-stacking, hydrogen bonding and charge-transfer interactions. The Py and NDI molecules were chosen on the basis of their high association constant[18] related to their opposite electron-donating/accepting character, with NDI being a strong electron acceptor and Py a good electron donor. Both molecules were functionalized with the diphenylalanine peptide as source of hydrogen-bonding sites (see Figure 6.1).

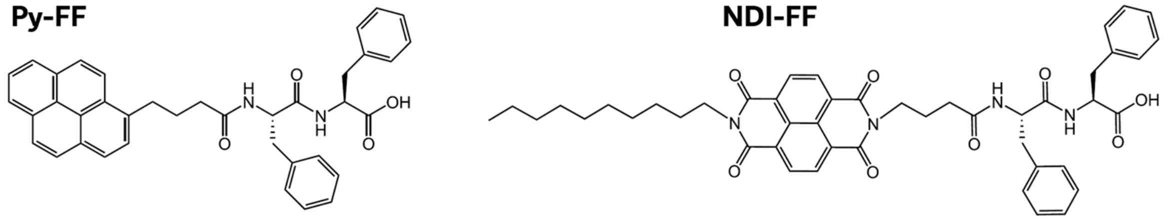

Figure 6.1 Chemical structures of the diphenylalanine-substituted pyrene and naphthalenediimide, labeled as Py-FF and NDI-FF respectively.

Hydrogen bonding was shown to be essential for gelation, leading to the formation of supramolecular fibers, that also displayed charge-transfer character.

The charge-transfer character of the gel is expected to be associated with the photogeneration of charges while the presence of supramolecular fibers likely underpins semiconducting properties. The investigation of such properties was the aim of the EPR study that will be presented in this Chapter.

The Chapter will begin with a brief description of the gel preparation and characterization, that was carried out by Prof. Mba group, followed by the presentation of the EPR investigation.

6.1 Gel preparation and characterization

The gel was obtained by dissolving NDI-FF and Py-FF (see Figure 6.1) in ODCB in a 1:1 molar ratio at 7mM concentration in each component.

The solution was heated to favor solubilization and it was subsequently cooled to room temperature. Upon cooling, the solution became red due to the formation of the CT complex and gelation occurred (Figure 6.2). Consistently, the UV-Vis spectrum of the gel showed the emergence of a new band centered at around 520 nm that can be interpreted as a CT-band (Figure 6.3 A).

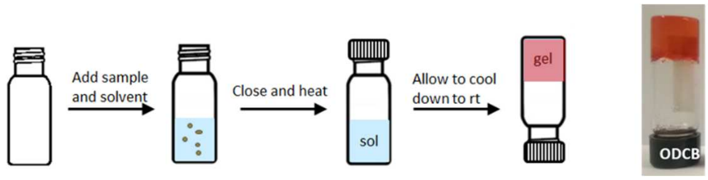

Figure 6.2 Scheme for the gel preparation.

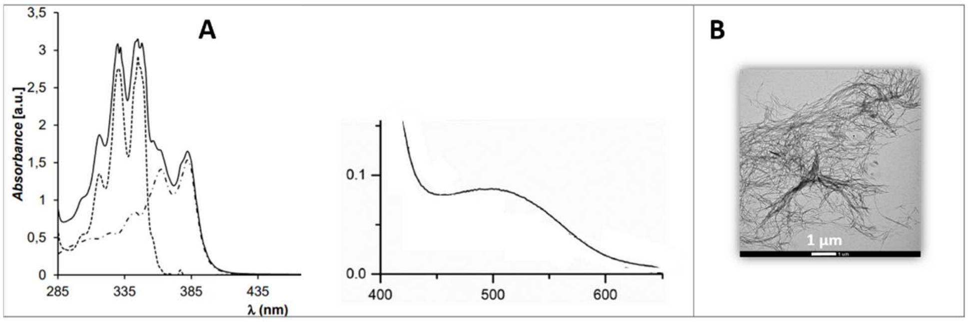

Figure 6.3 A: UV-Vis spectra of the gel (solid lines), NDI-FF and Py-FF region (left) with NDI-FF spectrum (dashdotted line) and Py-FF spectrum (dashed line), CT-band region (right); B: TEM image.

A morphological analysis on the gel was carried out with transmission electron microscopy (TEM). The TEM image of the gel is reported in Figure 6.3B, showing the formation of an entangled network of fibers up to several µm in length. These structures are responsible for solvent immobilization leading to the formation of the gel matrix.

Considering the complementarity of the charge-transfer interaction between Py-FF and NDI-FF, the molecular packing leading to the formation of fibers is most likely of the D/A type, i.e. alternate stacking between donor and acceptor molecules. This is in line with findings from XRD investigations on crystals obtained from similar Py and NDI derivates[18]. However, the non-complementarity of the hydrogen bonding interaction does not exclude the presence of homo-molecular stacks, which however are believed to be of minor importance[18].

The existence of interdigitation between Py-FF and NDI-FF molecules was confirmed by variable temperature ^{1}H-NMR experiments. Indeed, by cooling the hot mixed ODCB solution of the two components up to the formation of the gel, a consistent shift of the amide protons was observed due to hydrogen bonding (see Figure 6.4), which was far less pronounced in the solutions of the individual components (not shown).

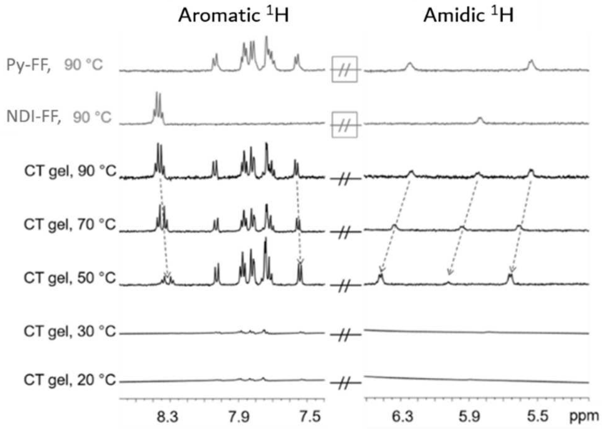

Figure 6.4 Variable-temperature NMR spectra (300MHz, d_4ODCB) performed on the CT gel.

Only one proton amide signal of NDI-FF could be monitored, as the other was partially overlapped with the solvent signal, and it moved from 5.84 ppm to 6.03 ppm upon gelation. Analogously, the two amide protons in the Py-FF at 6.24 and 5.54 ppm were shifted by 0.18 and 0.12 ppm respectively. Such downfield shifts prove the formation of hydrogen-bonds upon gelation, and their higher value compared to the solutions of the single components reveals the importance of the cooperation between the hydrogen-bonding and the CT interaction in determining the overall strength of the intermolecular interactions.

The charge-transfer interaction also showed up in the NMR study, being the main responsible for the shifts of the aromatic protons signals. The NDI-FF aromatic multiplet was shifted upfield by 0.05 ppm which can be attributed to the shielding effect due to both the π-stacking and the electron-withdrawing character of the NDI in the CT complex. For Py-FF the shift was less pronounced because of the opposite effects of π-stacking and electron-donation.

The formation of the hydrogen bonding seen by NMR was further supported by FTIR spectra of the gel, that showed two diagnostic bands of hydrogen-bonded amides, namely a band at 3271cm^{-1}, from the NH stretching, and a peak at 1640 cm^{-1}, which is attributed to carbonyl stretching in H-bonded amide groups. This latter peak is also diagnostic of β-sheet conformation[19].

Hydrogen bonding was found to be fundamental for the gel formation. Indeed, the removal of the peptide moieties prevented the formation of the gel. Furthermore, the use of H-bond competing solvents, like DMSO, strongly hampered the self-assembling resulting in no gel formation and in a yellow color of the solution, revealing that much weaker CT interactions take place, due to the improved solvation ability of the solvent. These evidences highlight that hydrogen-bonding has a critical role in stabilizing the donor-acceptor complex leading to the formation of the stacked structures assembling into fibers.

In Figure 6.5 a model for the packing between Py-FF and NDI-FF molecules is proposed on the basis of the above observations.

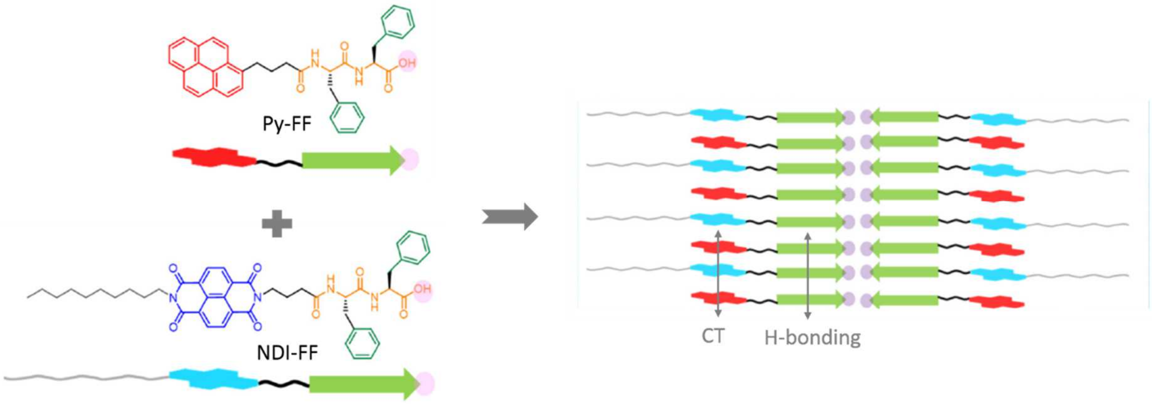

Figure 6.5 Proposed packing-model of Py-FF and NDI-FF molecules in the fibers.

6.2 EPR spectroscopy

EPR spectroscopy was used to assess the photophysical properties of the NDI-FF/Py-FF gel system.

The study presented here was carried out using several EPR techniques, each one capable to probe different characteristics of the system. TR-EPR was used to study photoexcited molecular triplet states while Light-induced CW-EPR gave information on charge photogeneration. Finally, Pulse-EPR methods provided insight into the hyperfine interaction of the photogenerated radicals.

In order to highlight properties related to the formation of extended stacked structures, the investigation of the gel was accompanied by the study of the solution phase in DMSO, where the self-assembling of stacked structures is prevented due to the reduced efficiency of hydrogen bonding formation in this solvent, as described above. In the following, the two samples will be referred to according to the solvent in which they were obtained i.e. ODCB for the gel and DMSO for the solution-phase sample.

6.2.1 TR-EPR: insight into the triplet state of the NDI-FF/Py-FF CT complex

Time-resolved EPR with visible or UV laser pulse photoexcitation was extensively used in the past to investigate the charge-transfer character of the triplet state of many CT crystals[20,21,22,23]. We applied it to our NDI-FF/Py-FF CT system in the attempt of gaining similar insight into the triplet state characteristics.

In Figure 6.6 TR-EPR spectra of the gel and DMSO samples, together with the spectra of the single components solutions, are reported. The spectra were acquired at 130K due to the small lifetime and fast spin relaxation of triplet states at higher temperatures. The samples were inserted in the cooled resonator to provide fast freezing in order to limit rearrangements. The gel stability in these conditions was verified upon inspection of the sample after fast freezing, which showed no relevant modification in all properties.

The TR-EPR spectra of the ODCB solutions of NDI-FF and Py-FF were acquired using the lowest photoexcitation wavelength achievable in our set-up, namely the Nd/YAG laser third harmonic i.e. 355 nm, since the molecules have no absorption in the Visible range (see Figure 6.3). The triplet spectrum of Py-FF was hardly visible in these conditions, since the absorption is still low at the 355 nm wavelength. The NDI-FF gave a better result, allowing to extract the dipolar tensor parameters from the spectral simulation (Table 6.1).

The TR-EPR spectra detected in the ODCB and DMSO NDI-FF/Py-FF samples were obtained by photoexcitation in the CT band (532 nm). Considering that the single components have no absorption at this wavelength, the excited triplet states are necessarily formed upon excitation of the NDI-FF/Py-FF complex. Therefore, they can be in interpreted as the triplet state of the CT complex.

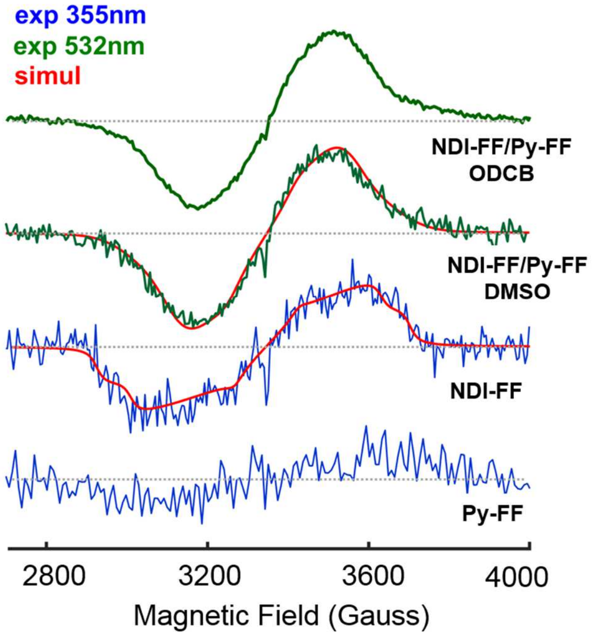

Figure 6.6 TR-EPR spectra (130K) of Py-FF and NDI-FF in ODCB, and of the NDI-FF/Py-FF couple in ODCB (gel) and in DMSO.

The spectral shape of the NDI-FF/Py-FF samples is unusual as the turning-points corresponding to the canonical EPR transitions for the triplet are not clearly visible. There are two main phenomena that can explain such an appearance of the spectrum. The first is that the triplet excitation may be mobile. Indeed, if a triplet exciton moves between sites in a disordered material, the dipolar interaction tends to be averaged out since at each site the D-tensor has a different orientation with respect to the magnetic field. The extent of this motional averaging is determined by the hopping rate: as the hopping rate increases, the spectrum gradually coalesces to a single lorentzian line. Mobile triplet states were observed in CT crystals, in which the motion only causes motional narrowing of the lines since the molecules are all oriented in the same way[24].

Hopping is thermally activated and consequently it can be investigated by acquiring the spectra at different temperatures. By cooling down the NDI-FF/Py-FF samples to 80K we observed the same spectrum (not shown), however, this temperature may be insufficiently low to immobilize the triplet if the hopping activation energy is small. So, we cannot exclude this mechanism.

The second phenomenon that may be responsible of the structureless lineshape is static and it is related to the inhomogeneity in the sample, leading to a distribution of dipolar parameters of the triplet wavefunction (“D-strain”), which causes line-broadening. This hypothesis seems quite realistic since we are not dealing with isolated molecules but likely various kinds of stacks are formed that may induce small differences in the triplet wavefunction.

According to the latter hypothesis the spectra of both NDI-FF/Py-FF samples could be simulated using the ZFS parameters listed in Table 6.1, including a 50 Gauss (FWHM) line-broadening due to a distribution of the D parameter values (D-strain).

Table 6.1 Triplet state parameters of NDI-FF in ODCB and of the NDI-FF/Py-FF couple in ODCB (gel) and DMSO.

Sample	D (Gauss)	E (Gauss)	Px:Py:Pz
NDI-FF	320±10	50±10	0.38 : 0.48 : 0.14
NDI-FF/Py-FF	395±5	78±5	0.42 : 0.53 : 0.05

The triplet state of weak CT complexes can be described as a superposition of three wavefunctions[20], namely a neutral triplet state localized on the donor molecule, an ionic triplet wavefunction in which one electron is localized on the donor (which becomes a radical cation) and the other on the acceptor (the radical anion), and the neutral triplet state localized on the acceptor molecule:

$$\psi_{T,CT} = c_1 \cdot \varphi_T(D^* A^0) + c_2 \cdot \varphi_T(D^+ A^-) + c_3 \cdot \varphi_T(D^0 A^*) \qquad \text{Eq. 6.1}$$

In numerous studies the above relation was used to derive the charge-transfer character of the lowest triplet state in crystals of weak CT complexes[20,21,23]. As proposed by Haarer, this could be done by comparing the experimentally measured elements of the ZFS tensor of the complex with the ones measured for the localized triplet states of the donor and the acceptor, and the elements calculated for an ionic triplet wavefunction. Very often one of the localized triplets could be excluded from Eq. 6.1 because of its higher energy compared to the other states. As a result, the c_2 coefficient could be easily obtained from the equation, representing the CT character of the observed triplet.

In our system the same analysis is prevented by the uncertainty on the determination of the ZFS principal values due to the structureless shape of the spectrum, since we are not dealing with a crystal but with a disordered and likely inhomogeneous system. However, a few qualitative considerations can be done. It can be seen from the cited studies that a considerable charge transfer character is associated with a sharp decrease in the D parameter, clearly because the triplet wavefunction is more delocalized if there is a consistent charge transfer degree. By comparing the D value for the NDI-FF/Py-FF complex with the D value of the NDI-FF we can infer that the observed triplet of the complex is essentially neutral, since D is only slightly smaller with respect to the triplet localized on the naphthalene diimide. In other words, the CT complex triplet state can be described as a superposition of states with a small contribution of the ionic state (small c_2 coefficient in Eq. 6.1). Most likely both the NDI-FF and the Py-FF triplet wavefunctions contribute to the wavefunction of the complex since they are very similar in energy (2.04 eV and 2.09 eV are the lowest triplet state energies of the NDI and Py molecules according to phosphorescence measurements[25,26]). Since the triplet state reflects the characteristics of the singlet state from which it is populated by ISC, we can conclude that also the singlet state that is excited by irradiation inside the CT band has weak charge-transfer character.

The analogous results for the samples in the two solvents (ODCB gel and DMSO solution) show that CT complexes are also formed in the DMSO solvent, despite the donor-acceptor interaction here is weaker due to the less effective hydrogen bonding, which prevents the self-assembling of fibers. This was expected from the high association constant of the NDI-Py couple[18].

6.2.2 Light-induced CW-EPR: charge photogeneration

Light-induced EPR was used to probe the photoactivity of the NDI-FF/Py-FF system in terms of generation of stable charges.

The results of the Light-induced CW-EPR experiments on the ODCB and DMSO NDI-FF/Py-FF samples are reported in Figure 6.7. The spectra were acquired both at room temperature and at 130 K.

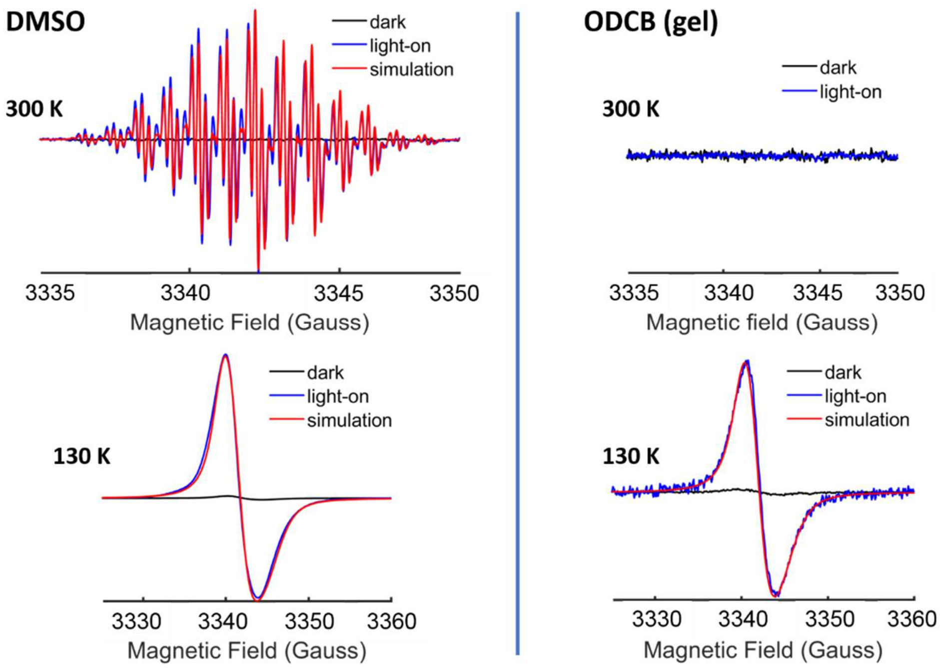

Figure 6.7 CW-EPR spectra of the NDI-FF/Py-FF samples.

For the DMSO solution investigated at 300 K no signal was detected in dark, but a sharp and structured signal arose upon illumination. The signal is centered at g=2.0025 and it is composed of 13 multiplets, each of which is split into 5 lines of about 0.2 Gauss linewidth. The simulation could be obtained assuming a spin ½ species interacting with 2 equivalent ^{14}N atoms and two groups of 4 equivalent protons each. The isotropic hyperfine coupling (a_{iso}) with ^{14}N (2.64 MHz) is exactly half the coupling with the first group of protons (5.28 MHz), giving rise to 13 lines, that are spilt into 5 due to the smaller interaction with the second group of protons (0.59 MHz) (Table 6.2).

Table 6.2 Isotropic hyperfine couplings in NDI-FF$^{\bullet-}$.

Nuclei	n	a_{iso} (MHz)
^{14}N	2	2.64
$^{1}H_a$	4	5.28
$^{1}H_b$	4	0.59

This pattern is consistent with a radical having the NDI structure, leading to the assignment of the signal to the NDI-FF radical anion, in which the strongly coupled ^{1}H and ^{14}N belong to the central ring, while the weakly coupled protons correspond to the CH_2 protons attached to the diimide nitrogens (Figure 6.8).

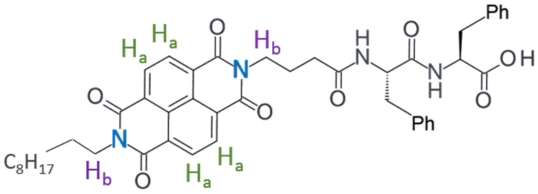

Figure 6.8 NDI-FF structure with highlighted coupled nuclei.

Hyperfine couplings with other nuclei of the side-chains were not detected, i.e. they must be included in the 0.2 Gauss linewidth, revealing that negligible spin-density is localized over the peptide chains. Our assignment is supported by literature on chemically reduced alkyl-substituted NDIs, for which very similar patterns and a_{iso} values were found[27], also confirming that the majority of the spin-density in NDIs radicals is localized on the NDI ring, with small influence of the side-chains.
By freezing the DMSO solution, the photoinduced spectrum lost the hyperfine structure due to line-broadening associated to A and g anisotropy, leading to an unresolved line of 4 Gauss peak-to-peak linewidth, centered at the same g-factor of 2.0025. The identification with the NDI-FF$^{\bullet-}$ radical in this case was provided by hyperfine spectroscopy, highlighting a strong interaction with ^{14}N nuclei, as will be discussed in the next section.

For the ODCB gel sample no photogeneration of radicals could be observed at room temperature. However, the system photoactivity was proved at low T, where a light-induced signal was detected. The linewidth of the signal is 3.1 Gauss and it is centered at 2.0025 Gauss like the NDI-FF$^{\bullet-}$ radical in the DMSO sample. Also in this case the assignment was confirmed by the hyperfine coupling with ^{14}N nuclei, revealed by hyperfine spectroscopy methods.

Clearly, if the photogeneration of radicals occurs at low T, there is no reason why it should not occur at room temperature. However, the absence of signal at high T can be explained considering that the lifetime of the radicals may be drastically reduced by thermally-activated recombination, causing a steady-state concentration of radicals below the spectrometer sensitivity.

In both solvents, the absence of EPR signal in dark indicates that the ground state of the donor/acceptor system is neutral, i.e. with no charge separation. This is in line with the findings presented in the previous section on the charge-transfer character of the excited triplet state, which was proposed to be almost neutral, suggesting the same for the first excited singlet state. Both these evidences point to the weak character of the charge-transfer complex in the examined systems. Nevertheless, electron-transfer between the two molecules is promoted by light-illumination, leading to complete charge separation, as demonstrated by the EPR signature of non-interacting NDI-FF$^{\bullet-}$ radicals. Although there is no evidence of the formation of Py-FF$^{\bullet+}$ radicals from LEPR, the role of Py-FF as electron-donor is confirmed by observing that NDI-FF alone in the same solvents does not produce photoinduced radicals (spectra not shown).

In the attempt to clarify the reason for the absence of EPR signals by Py-FF radicals we oxidized Py-FF in an ODCB solution using PIFA (phenyl-iodine bis(trifluoroacetate)). The resulting signal of Py-FF$^{\bullet+}$ consists of a line with 10 Gauss peak-to-peak linewidth centered at g=2.0025 (Figure 6.9 A). This is consistent with old EPR studies on the radical cation of pyrene, reporting a 2.00253 g-factor and large proton hyperfine couplings (four ^{1}H with 5.38 G a_{iso}, four ^{1}H with 2.12 G a_{iso} and two ^{1}H with 1.18 G a_{iso})[28], that are compatible with the 10 G linewidth that we observed in the frozen solution of Py-FF.

Considering the g-factor of Py-FF$^{\bullet+}$ coincides with the g-factor of NDI-FF$^{\bullet-}$, their signals should be superimposed. However, the line we detected in the NDI-FF/Py-FF samples at 130 K is only 4 G large, thus, any contribution by Py-FF$^{\bullet+}$ must be very small. The same holds for the signal observed at room temperature in the DMSO solution, where the hyperfine pattern unambiguously stems from the NDI-FF$^{\bullet-}$ radical.

Two main explanations can be provided for the absence of a Py-FF$^{\bullet+}$ signal in the detected spectra. The first refers to the formation of diamagnetic species of the oxidized donor molecule, for example pyrene dications[29]. The second explanation is related to spin relaxation times, that may prevent the signal detection. We have no possibility to test the first hypothesis with EPR, while the second one can be evaluated by saturation experiments i.e. by variation of the microwave power in CW-EPR. From saturation experiments on the NDI-FF/Py-FF samples under illumination we found that a large signal arose at high MW power, that is compatible with the pyrene radical signal (Figure 6.9 B). This points to the existence of Py-FF radicals with fast spin-relaxation, giving rise to a signal only at high MW power. Therefore, we think that this hypothesis is the most probable.

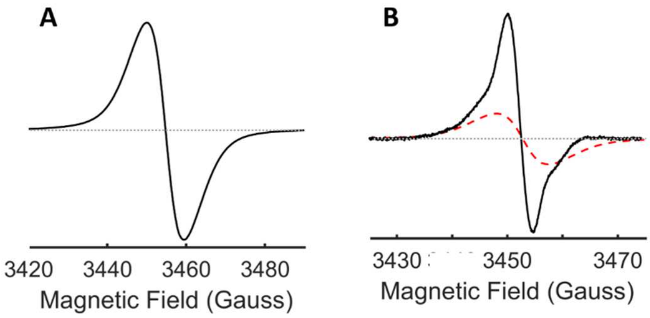

Figure 6.9 A: CW-EPR spectrum (80K) of the Py-FF$^{\cdot+}$ radical in ODCB solution, obtained by oxidation with PIFA in dark; B: Light-on CW-EPR spectrum (130K) of the NDI-FF/Py-FF ODCB gel recorded at high microwave power (20 mW, black line), scaled spectrum of the Py-FF$^{\cdot+}$ radical in ODCB solution (red dashed line).

The LEPR measurements presented so far (Figure 6.7) highlighted a fundamental difference between the gel sample and the solution sample, namely the lifetime of photogenerated charges. Indeed, the absence of photoinduced signal in the gel at 300 K can be explained as an effect of fast recombination. Furthermore, a comparison of the intensities of the gel and solution signals at 130 K reveals that the gel signal is one order of magnitude less intense, in line with the existence of faster charge-loss processes in the gel.

This hypothesis was confirmed by the decay kinetics of the photoinduced EPR signals at 130 K measured after switching off the illumination (Figure 6.10). The contrast between the two systems here is striking, with radicals stable within many hours in the DMSO frozen solution and decay times in the order of minutes in the ODCB gel. The decay of the LEPR intensity is associated to charge-recombination[30], therefore the different kinetics reveal the two systems consistently differ in terms of charge recombination rate.

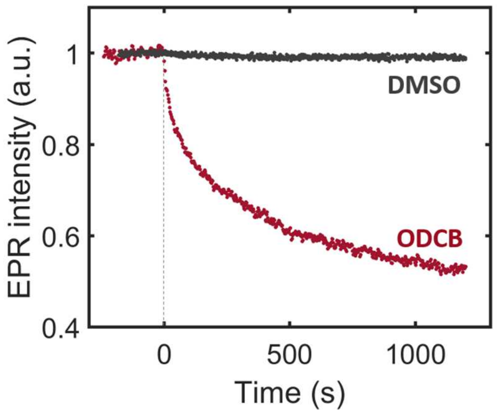

Figure 6.10 EPR signal decay (130K) upon switching-off illumination at t=0 in the NDI-FF/Py-FF samples.

Geminate recombination, i.e. recombination between nascent radical pairs, is expected to occur in submicrosecond timescales after electron transfer, as observed in other organic semiconductors[31]. Its effect is to reduce the amount of radicals that can be detected by LEPR, i.e. stable radicals with lifetimes in the range of milliseconds or more, and consequently to reduce the signal intensity. However, geminate recombination does not contribute to the signal decay when light is switched off because it is not effective anymore in the time scale of LEPR. This means that the reported decay is mainly associated with non-geminate back-electron transfer phenomena, i.e. recombination between separated charges. Non-geminate recombination in organic disordered semiconductors is known to be limited by the hopping rate of charges inside the material[32], as this determines the probability of collisions and back electron transfer. Therefore, we can infer that the faster recombination rate in the gel sample is an indication of the more efficient hopping of charges, suggesting a more efficient charge transport. On the other hand, in the DMSO solvent charges are highly stabilized, and recombination is slowed down.

This behavior can be related to the strong D/A interactions in the ODCB solvent, leading to the formation of the extended stacked structures of the gel, that allow charge diffusion along the stacks. Conversely, DMSO efficiently interacts with the solute molecules by hydrogen bonding, preventing the formation of stacks and providing stabilization for charges.

These results point to the potentialities of the supramolecular structures in the NDI-FF/Py-FF system as semiconducting architectures, by highlighting the differences with the analogous system where fibers are not formed.

6.2.3 Hyperfine spectroscopy

As described in Chapter 2, Pulse EPR methods have been developed allowing for indirect detection of nuclear spin transitions belonging to nuclei that are coupled with the electronic spin through the hyperfine interaction. Hyperfine couplings that are often unresolved in CW-EPR spectra can be readily extracted from nuclear transitions frequencies. Two-dimensional techniques are particularly relevant to the problem of determining hyperfine interactions, as they provide the highest resolution. For this reason, HYSCORE is preferred to ESEEM techniques[33,34,35].

The interest in the determination of hyperfine couplings is related to their intimate connection with the spin-density distribution inside the molecule. Furthermore, they are affected by the dynamics of the spin, providing indications in this respect.

From CW-EPR experiments described above we could only determine the isotropic hyperfine couplings of the NDI-FF radical anion photogenerated in the NDI-FF/Py-FF DMSO solution, as in the gel system only the low temperature spectrum was detectable, where the couplings are unresolved.

In order to fully exploit the information content of hyperfine coupling constants, we performed HYSCORE experiments on the NDI-FF/Py-FF gel sample and on the DMSO solution as reference system.

The HYSCORE spectra were acquired at three τ values and then summed to avoid blind-spot effects. The magnetic field was kept fixed at the value of maximum intensity of the NDI-FF$^{\cdot-}$ radical EDEPR spectrum, since orientation selection was avoided by the use of strong pulses (see the Experimental section for further details on the experiment). Intense low frequency modulations by ^{14}N nuclei dominated the HYSCORE time trace, leading to intense peaks in the Fourier-transformed spectrum. Couplings with ^{1}H nuclei were barely visible in the spectra, which can be attributed to the presence of the strong modulating ^{14}N nuclei, that were shown to cause suppression of weaker modulating contributions by Stoll et al.[36]. For this reason, the discussion will be limited to the ^{14}N frequency region.

The HYSCORE spectrum of the DMSO sample is shown in Figure 6.11 A. It shows peaks in both the (-,+) and the (+,+) quadrant. The two peaks in the (-,+) quadrant indicate a strong-coupling regime. They are centered at 2.6 MHz and are separated by 4.2 MHz, which is exactly four times the nuclear frequency of ^{14}N at the magnetic field of the experiment (ν_{14N}=1.05 MHz at 3446 G). Therefore, they are readily identified as correlation peaks between the double-quantum transitions ($A \pm 2\nu_{14N}$) in the two electron spin manifolds. The elongated shape of the peaks reflects the anisotropy of the hyperfine interaction.

The assignment of the signals in the (+,+) quadrant is not as much straightforward. However, it is known from literature that double quantum transitions are the most intense in systems with ^{14}N nuclei, due to the strong quadrupolar interaction that consistently broadens single quantum cross-peaks[35]. Hence, we attribute the ridge in the (+,+) quadrant to double quantum transitions due to weaker hyperfine couplings associated with different molecular orientations. The small diagonal peak at 2.2 MHz corresponds to the nuclear frequency of ^{2}H belonging to the deuterated DMSO solvent that was used, revealing a weak interaction of the NDI-FF$^{\cdot-}$ spin with the solvent molecules.

The HYSCORE spectrum of the ODCB gel sample is quite different (Figure 6.11 B). The cross peaks in the (-,+) quadrant disappeared, indicating a shift from the strong coupling regime to the weak coupling regime. The peaks in the (+,+) quadrant are most likely due to double-quantum transitions also in this case, but their assignment is not as immediate as in the strong-coupling case, due to the similar value of the hyperfine and quadrupolar interaction. The round shape of the peaks indicates a smaller hyperfine anisotropy compared to the previous sample.

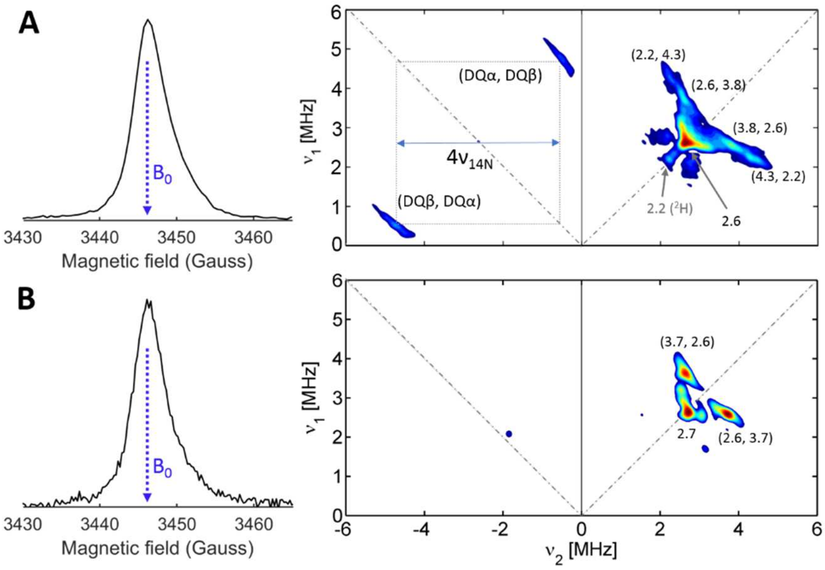

Figure 6.11 A: EDEPR spectrum, showing the field position used for HYSCORE acquisition, and HYSCORE spectrum (80K) of the NDI-FF$^{\cdot-}$ radical in the DMSO sample; B: EDEPR and HYSCORE spectra (80K) of the NDI-FF$^{\cdot-}$ radical in the ODCB gel sample.

Spectral simulations were performed using Easyspin to derive ^{14}N hyperfine and quadrupolar parameters of the systems. The simulations are shown in Figure 6.12 and the corresponding parameters are reported in Table 6.3. Although not perfect, they reproduce the main spectral features. The a_{iso} value resulting from the simulation of the DMSO sample spectrum (a_{iso} =2.3 MHz) is close to the one that was determined from CW-EPR with high accuracy thanks to the absence of anisotropies in the solution at room temperature (a_{iso} =2.64 MHz, see previous section).

DFT calculations were performed in order to support the interpretation of the spectra. The B3LYP/EPR-II method was used to calculate the quadrupolar and hyperfine interactions of the central ring nitrogens in the NDI-FF$^{\cdot-}$ radical. The resulting quadrupolar constant and asymmetry parameter, as well as the a_{iso} value, are close to the ones determined from the simulation of the NDI-FF$^{\cdot-}$ signals in the DMSO sample, confirming the validity of the simulation (see Table 6.3). The difference with the a_{iso} determined for the radical in the ODCB gel sample arises because the radical in this system is not isolated like it is in both the DMSO sample and in the calculation.

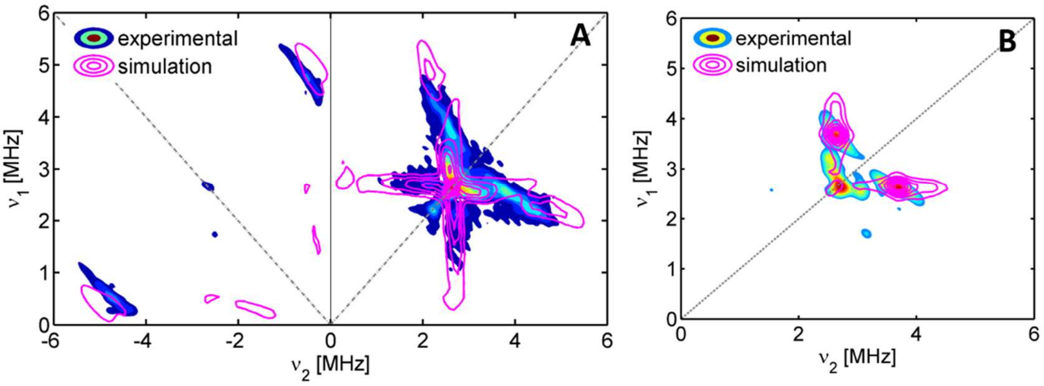

Figure 6.12 Superposition between HYSCORE spectra and their simulations.

Table 6.3 ^{14}N hyperfine and quadrupolar parameters derived from HYSCORE simulations and from DFT calculations.

	a_{iso} (MHz)	**A_{dip} (MHz)**			**e^2Qq/h (MHz)**	**η**
		A_x	**A_y**	**A_z**		
ODCB	1	-0.34	-0.16	0.50	3.1	0
DMSO	2.3	-0.7	-0.25	0.95	3.1	0
Calc	2.93	-1.13	-1.07	2.20	3.74	0.05

It is evident from the above data that the hyperfine coupling with the ^{14}N atoms is reduced by approximately a factor 2 in the radical generated in the gel compared to the radical that forms in the DMSO solution. This can be interpreted as an indication of two possible phenomena, namely charge hopping or charge delocalization.

The hopping of the electron between different molecules tends to average out the isotropic hyperfine interaction, since the nuclear spin of the new molecule where the electron jumps has random probability of being in the α or β spin state[37]. Consequently, if the hopping frequency is higher than the difference between the α and β hyperfine frequencies, the isotropic interaction is averaged out. The dipolar contribution to the hyperfine interaction is anisotropic and thus it tends to be cancelled upon hopping in disordered systems because the molecules at different hopping sites have different orientations. Our data can be interpreted in the frame of partial averaging of the hyperfine interaction due to hopping rates that are comparable to the frequency separation between the hyperfine transitions. The occurrence of this phenomenon in the gel sample can again be related to the presence of fibers, i.e. supramolecular stacks of molecules, that are expected to favor charge transport. This is in line with the results from CW-EPR described in the previous section, where the efficient charge transport was inferred from the enhanced non-geminate charge recombination rate.

The spin delocalization makes the hyperfine interaction weaker because the spin density is distributed over a larger number of atoms. This may as well explain the measured difference in the entity of the hyperfine interaction in the NDI-FF$^{\cdot -}$ radical between the gel and the solution sample, stemming from the larger delocalization of the anion provided by the stacking of molecules in the fibers of the gel.

Although spin delocalization is not a direct observation of charge transport as hopping is, it is closely related to it. Indeed, it was recently demonstrated that the delocalization of charges is critical for long-range charge separation in organic semiconductors, as it increases the average electron-hole separation, enhancing the dissociation probability[38,39].

Therefore, the results from hyperfine EPR spectroscopy suggest enhanced charge transport capabilities of the gel NDI-FF/Py-FF system, driven by the extended supramolecular structures of stacked molecules.

6.3 Conclusions

In this Chapter EPR spectroscopic techniques were applied to the study of the charge-transfer gel based on the peptide-substituted naphthalene diimide/pyrene couple. The experiments on the gel sample were performed in parallel to experiments on the solution of the two components in DMSO, a gel-disrupting solvent, in order to highlight peculiar photophysical properties induced by the presence of stacked structures forming the gel fibers.

TR-EPR spectroscopy unraveled the formation of triplet states of the CT complex upon photoexcitation. The comparison of the triplet EPR spectrum of the complex with the spectrum of the

single components showed that the charge-transfer character of the state is small, being essentially a neutral triplet state. This likely indicates a small CT character also in the excited singlet state from which the triplet is formed.
The findings on the CT character of the triplet are in line with the results from CW-EPR experiments, where the absence of EPR signals without photoexcitation revealed a neutral ground state for the complex. Therefore, the NDI-FF/Py-FF couple clearly forms a weak charge-transfer complex.

Light-induced CW-EPR showed that the photoactivity of the NDI-FF/Py-FF system is not limited to the formation of the excited triplet state, as also complete electron transfer occurs upon illumination, leading to the formation of separated charges. Indeed, the LEPR signal of the radical anion of the NDI-FF was detected in both the gel and in the DMSO solution. Light-induced EPR also allowed to disclose the different lifetime of photoinduced charges in the two systems, being smaller in the gel sample. This was confirmed by the light-off kinetics that showed an increased non-geminate recombination rate for the gel sample, attributable to the enhanced charge transport provided by the extensive stacking of molecules.

A detailed analysis of the hyperfine interaction inside the NDI-FF$^{\cdot -}$ radical was used to further probe functional properties of the gel. HYSCORE spectra highlighted a decrease in the hyperfine interaction between the electron spin and the ^{14}N nuclei of the NDI-FF ring inside the gel. The explanation for such a decrease is either electron hopping among molecules or increased spin delocalization due to stacking of molecules. Both phenomena are associated with improved charge transport in the system.

In conclusion, the presented EPR investigation, aimed at probing the potentialities of the NDI-FF/Py-FF self-assembled fibers as organic semiconductors, provided indications of encouraging properties of the system, namely charge photogeneration and transport. For this reason, it encourages future work oriented to the development of devices for the electrical characterization of the semiconducting properties of the material. A strong improvement in the charge transport ability could be reached by developing a strategy to achieve an average orientation of the fibers, leading to supramolecular wires capable of directional charge transport.

6.4 Experimental

Synthetic procedures, UV-Vis spectroscopy, TEM and NMR experiments were carried out by Dr. Silvia Bartocci from Prof. Mba group.

6.4.1 Materials

Solvents were of analytical reagent grade and used as received. NDI-FF was synthesized from commercial 1,4,5,8-naphthalene-tetracarboxylic-dianhydride as described in the article[40]. Py-FF was synthesized from commercial pyreneacetic acid as reported in ref. [41].

The gel was prepared from a ODCB solution of NDI-FF and Py-FF in a 1:1 molar ratio at 7mM concentration each, adopting the procedure described in the text (see section 6.1).

The DMSO solution had the same concentration of NDI-FF and Py-FF of the gel.

6.4.2 Samples preparation

To prepare the EPR tube (3 mm ID, 4 mm OD) with the ODCB gel, a vial with the gel was shaken to temporarily disrupt the gel. Then 250 µl of the resulting solution were withdrawn and put inside the quartz EPR tube. The solution inside the tube was degassed by bubbling N_2 for few minutes and the tube was then sealed using a blowtorch. The gel was formed again by heating and then cooling the EPR tube.

The EPR tube with the DMSO solution was prepared by putting 250 µL of the solution inside the tube, that was then extensively degassed by bubbling N_2. The tube was then sealed with the blowtorch.

6.4.3 UV-Vis spectroscopy

UV-Vis absorption spectra were acquired with a Varian Cary 100 spectrometer. A cell with detachable windows with a 0.2 mm path was used to measure the absorption of the gel. The gel was pre-formed in a vial and then transferred to the cell.

6.4.4 TEM

Transmission electron microscopy images were recorded with a Jeol 300PX instrument. The gel sample for TEM was prepared by dropping a small amount of gel into a glow discharged carbon coated grid and removing excess of gel with #50 hardened Whatman filter paper.

6.4.5 NMR

^{1}H NMR spectra were recorded on a Bruker Avance 300 spectrometer. A suspension of NDI-FF and Py-FF in d4-ODCB was introduced in a screw-cap NMR tube. The mixture was heated in order to get a clear solution and then allowed to cool to room temperature to obtain the gel. The temperature of the sample was increased with 10° steps to record the variable-temperature spectra.

6.4.6 EPR

6.4.6.1 CW-EPR and TR-EPR

Continuous wave EPR was performed with an X-band ER200D Bruker spectrometer, equipped with a nitrogen-flow variable-temperature system (Bruker BVT200), for sample temperatures control from 130K to 300K. Continuous illumination in LEPR experiments was provided by a 300W Xe lamp, providing approximately 50mW power inside the dielectric TE_{011} cavity, through a quartz optical fiber. In TR-EPR experiments the photoexcitation was obtained from a Nd:YAG pulsed laser (Quantel Brilliant, pulse length = 5 ns; E/pulse = ca. 5 mJ; repetition rate 50Hz). The laser wavelength was 532 or 355nm depending on the order of the harmonic-generator module. The spectra were acquired at 25 dB microwave power attenuation, with 256 field points and typically 500 averages per point.

6.4.6.2 Pulse-EPR and HYSCORE

Pulse-EPR experiments were performed on a X-band ELEXSYS E580 Bruker spectrometer, equipped with a dielectric resonator inside an Oxford CF900 cryostat. The samples were studied under continuous illumination from a 300 W Xe lamp, that was IR filtered and focused into a quartz optical fiber bringing the light to the sample inside the resonator.

HYSCORE experiments were performed using the pulse sequence $\pi/2–\tau–\pi/2–t_1–\pi–t_2-\pi/2–\tau$–echo with pulse lengths $t_{\pi/2}$=16ns and t_π=16ns. τ values were 140, 168 and 200 ns, t_1 and t_2 were incremented by dt=28ns leading to a 128×128 data matrix. A four-step phase cycle was used.

The time domain HYSCORE data were processed in Matlab. The baseline was corrected by a 3rd order polynomial and the resulting time traces were apodized using a Hamming window function. The matrix was then zero-filled with 1024 points in both dimensions. The 2D-Fourier transform was applied and the absolute-value spectrum was calculated.

6.4.7 DFT

The geometry optimization of the NDI-FF radical anion was carried out in Gaussian09[42] using the B3LYP/6-311G method. The side chains were truncated and replaced by methyl groups.

The calculation of the hyperfine and nuclear quadrupolar tensors was done with ORCA[43] using the B3LYP functional and the EPR-II basis set.

6.5 References

(1) Aida, T.; Meijer, E. W.; Stupp, S. I. Functional Supramolecular Polymers. *Science* **2012**, *335*, 813–817.

(2) Schenning, A. P. H. J.; Meijer, E. W. Supramolecular Electronics ; Nanowires from Self-Assembled p-Conjugated Systems. *Chem. Commun.* **2005**, *0*, 3245–3258.

(3) Das, A.; Ghosh, S. H-Bonding Directed Programmed Supramolecular Assembly of Naphthalene-Diimide (NDI) Derivatives. *Chem. Commun.* **2016**, *52*, 6860–6872.

(4) Zhang, J.; Xu, W.; Sheng, P.; Zhao, G.; Zhu, D. Organic Donor – Acceptor Complexes as Novel Organic Semiconductors. *Acc. Chem. Res.* **2017**, *50*, 1654–1662.

(5) Schenning, A. P. H. J.; Herrikhuyzen, J.; Jonkheijm, P.; Chen, Z.; Wu, F.; Meijer, E. W. Photoinduced Electron Transfer in Hydrogen-Bonded Oligo(P-Phenylene Vinylene) - Perylene Bisimide Chiral Assemblies. *JACS* **2002**, *124*, 10252–10253.

(6) Tsutsumi, J.; Toshikazu, Y.; Hiroyuki, M.; Haas, S.; Hasegawa, T. Competition between Charge-Transfer Exciton Dissociation and Direct Photocarrier Generation in Molecular Donor-Acceptor Compounds. *Phys. Rev. Lett.* **2010**, *105*, 226601.

(7) Tsutsumi, J.; Matsui, H.; Yamada, T.; Kumai, R.; Hasegawa, T. Generation and Diffusion of Photocarriers in Molecular Donor–Acceptor Systems: Dependence on Charge-Transfer Gap Energy. *J. Phys. Chem. C* **2012**, *116*, 23957–23964.

(8) Yamamoto, Y.; Fukushima, T.; Suna, Y.; Ishii, N.; Saeki, A.; Seki, S.; Tagawa, S.; Taniguchi, M.; Kawai, T.; Aida, T. Photoconductive Coaxial Nanotubes of Molecularly Connected Electron Donor and Acceptor Layers. *Science* **2006**, *314*, 1761–1765.

(9) Zhang, W.; Jin, W.; Fukushima, T.; Saeki, A.; Seki, S.; Aida, T. Supramolecular Linear Heterojunction Composed of Graphite-Like Semiconducting Nanotubular Segments. *Science* **2011**, *334*, 340–343.

(10) Puigmartí-luis, J.; Laukhin, V.; Vidal-gancedo, J.; Rovira, C.; Laukhina, E.; Amabilino, D. B. Supramolecular Conducting Nanowires from Organogels. *Angew. Chemie* **2007**, *119*, 242–245.

(11) Ajayaghosh, A.; Praveen, V. K.; Vijayakumar, C. Organogels as Scaffolds for Excitation Energy Transfer and Light Harvesting. *Chem. Soc. Rev.* **2008**, *37*, 109–122.

(12) Babu, S. S.; Prasanthkumar, S.; Ajayaghosh, A. Self-Assembled Gelators for Organic Electronics. *Angew. Chemie Int. Ed.* **2012**, *51*, 1766–1776.

(13) Babu, S. S.; Praveen, V. K.; Ajayaghosh, A. Functional π - Gelators and Their Applications. *Chem. Rev.* **2014**, *114*, 1973-2129.

(14) Johnson, E. K.; Adams, J.; Cameron, P. J. Peptide Based Low Molecular Weight Gelators. *J. Mater. Chem.* **2011**, *21*, 2024–2027.

(15) Yang, X.; Zhang, G.; Zhang, D. A New Ex-TTF-Based Organogelator: Formation of Organogels and Tuning with Fullerene. *Langmuir* **2010**, *26*, 11720–11725.

(16) Xue, P.; Lu, R.; Zhao, L.; Xu, D.; Zhang, X.; Li, K.; Song, Z.; Yang, X.; Takafuji, M.; Ihara, H. Hybrid Self-Assembly of a π Gelator and Fullerene Derivative with Photoinduced Electron Transfer for Photocurrent Generation. *Langmuir* **2010**, *26*, 6669–6675.

(17) Sugiyasu, K.; Kawano, S.; Fujita, N.; Shinkai, S. Self-Sorting Organogels with P-N Heterojunction Points. *Chem. Mater.* **2008**, *20*, 2863–2865.

(18) Sikder, A.; Ghosh, B.; Chakraborty, S.; Paul, A.; Ghosh, S. Rational Design for Complementary Donor–Acceptor Recognition Pairs Using Self-Complementary Hydrogen Bonds. *Chem. - A Eur. J.* **2016**, *22*, 1908–1913.

(19) Marchesan, S.; Styan, K. E.; Easton, C. D.; Waddington, L.; Vargiu, A. V. Higher and Lower Supramolecular Orders for the Design of Self-Assembled Heterochiral Tripeptide Hydrogel Biomaterials. *J. Mater. Chem. B* **2015**, *3*, 8123–8132.

(20) Keijzers, C. P.; Haarer, D. EPR Spectroscopy of Delocalized and Localized Charge-Transfer Excitons in Phenanthrene-PMDA Single Crystals. *J. Chem. Phys.* **1977**, *67*, 925–932.

(21) Gundel, D.; Frick, J.; Krzystek, J.; Sixl, H.; Von Schutz, J. U.; Wolf, H. C. A quasi-neutral triplet state of TCNQ in phenazine/TCNQ and fluorene/TCNQ CT crystals. *Chem. Phys.* **1989**, *132*, 363–372.

(22) Pasimeni, L.; Guella, G.; Corvaja, C.; Clemente, D. A.; Pasimeni, L.; Guella, G.; Corvaja, C.; Clemente, D. A.; Vicentini, M. Crystal Structure of Biphenyl-Tetracyanobenzene 1:1 CT Complex and EPR Investigation of Photoexcited Triplet Excitons. *Mol. Cryst. Liq. Cryst.* **1983**, *91*, 25–38.

(23) Agostini, G.; Corvaja, C.; Giacqmetti, G.; Pasimeni, L. ESR and DF ODMR Studies of Photoexcited Triplets in Single Crystals of T-Stilbene-1,2,4,5-Tetracyanobenzene 1:2 Complex. *Chem. Phys.* **1984**, *85*, 421–429.

(24) Mohwald, H.; Sackman, E. Mobile Charge-Transfer Triplet Excitons in Biphenyl-Tetracyanobenzene Single Crystals. *Chem. Phys. Lett.* **1973**, *21*, 43–48.

(25) Gijzeman, L. J.; Kaufman, F.; Porter, G. Oxygen Quenching of Aromatic Triplet States in Solution. *J. Chem. Soc. Faraday Trans. 2* **1973**, *69*, 708–720.

(26) Rogers, J. E.; Kelly, L. A. Nucleic Acid Oxidation Mediated by Naphthalene and Benzophenone Imide and Diimide Derivatives: Consequences for DNA Redox Chemistry. *J. Am. Chem. Soc.* **1999**, *121*, 3854–3861.

(27) Andric, G.; Boas, J. F.; Bond, A. M.; Fallon, G. D.; Ghiggino, K. P.; Hogan, C. F.; Hutchison, A. A.; Lee, M. A.-P.; Langford, S. J.; Pilbrow, J. R.; et al. Spectroscopy of Naphthalene Diimides and Their Anion Radicals. *Aust. J. Chem.* **2004**, *57*, 1011–1019.

(28) Howarth, O. W.; Fraenkel, G. K. Electron Spin Resonance Spectra of Monomeric and Dimeric Cation Radicals. *J. Chem. Phys.* **1970**, *52*, 6258–6267.

(29) Forsyth, D. A.; Olah, G. A. Oxidation of Polycyclic Arenes in SbF5/ SO2ClF . Formation of Arene Dications and Observation of Electron Exchange with Radical Cations Based on ^{13}C Nuclear Magnetic Resonance Studies. *J. Am. Chem. Soc.* **1976**, *98*, 4086–4090.

(30) Niklas, J.; Poluektov, O. G. Charge Transfer Processes in OPV Materials as Revealed by EPR Spectroscopy. *Adv. Energy Mater.* **2017**, 1602226.

(31) Shuttle, C. G.; Regan, B. O.; Ballantyne, A. M.; Nelson, J.; Bradley, D. D. C.; Durrant, J. R. Bimolecular Recombination Losses in Polythiophene:fullerene Solar Cells. *Phys. Rev. B* **2008**, *78*, 113201.

(32) Wong, W. S.; Salleo, A. *Flexible Electronics: Materials and Applications*; Springer: New York, 2009.

(33) Hofer, P.; Grupp, A.; Nebenfuhr, H.; Mehring, M. Hyperfine Sublevel Correlation (HYSCORE) Spectroscopy: A 2D ESR Investigation of the Squaric Acid Radical. *Chem. Phys. Lett.* **1986**, *132*, 279–282.

(34) Van Doorslaer, S. Hyperfine Sublevel Correlation Spectroscopy. *EPR Newsl.* **2008**, *17*, 9–12.

(35) Harmer, J.; Mitrikas, G.; Schweigher, A. Advanced Pulse EPR Methods for the Characterization of Metalloproteins. In *High Resolution EPR*; Springer Science: New York, 2009; pp 13–61.

(36) Stoll, S.; Calle, C.; Mitrikas, G.; Schweiger, A. Peak Suppression in ESEEM Spectra of Multinuclear Spin Systems. *J. Magn. Reson.* **2005**, *177*, 93–101.

(37) Carrington, A.; McLachlan, A. D. *Introduction to Magnetic Resonance*; Chapman and Hall: London, 1979.

(38) Bakulin, A. A.; Rao, A.; Pavelyev, V. . G.; van Loosdrecht, P. H. M.; Pshenichnikov, M. S.; Niedzialek, D.; Cornil, J.; Beljonne, D.; Friend, R. H. The Role of Driving Energy and Delocalized States for Charge Separation in Organic Semiconductors. *Science* **2012**, *335*, 1340–1344.

(39) Schlenker, C. W.; Li, C.; Yip, H.; Jen, A. K.; Rao, A.; Chow, P. C. Y.; Ge, S.; Ginger, D. S.; Friend, R. H. The Role of Spin in the Kinetic Control of Recombination in Organic Photovoltaics. *Nature* **2013**, *500*, 435–440.

(40) Bartocci, S.; Berrocal, J. A.; Guarracino, P.; Grillaud, M.; Franco, L.; Mba, M. Peptide-Driven Charge-Transfer Organogels Built from Synergetic Hydrogen Bonding and Pyrene – Naphthalenediimide Donor – Acceptor Interactions. *Chem. - A Eur. J.* **2018**, *24*, 2920–2928.

(41) Bartocci, S.; Morbioli, I.; Maggini, M.; Mba, M. Solvent-Tunable Morphology and Emission of Pyrene-Dipeptide Organogels. *Pept. Sci.* **2015**, *2015*, 871–878.

(42) M. J. Frisch, G. W. Trucks, H. B. Schlegel, G. E. Scuseria, M. A. Robb, J. R. Cheeseman, G. Scalmani, V. Barone, B. Mennucci, G. A. P. et al. Gaussian 09 Revision B.01. Gaussian, Inc, Wallingford, CT, USA 2009.

(43) Neese, F. The ORCA Program System. *WIREs Comput Mol Sci* **2012**, *2*, 73–78.

Abbreviations

BHJSC	Bulk Heterojunction Solar Cell
CS	Charge-separated state
CT	Charge-transfer state
DSSC	Dye-sensitized Solar Cell
EDEPR	Echo-detected EPR
HYSCORE	Hyperfine Sublevel Correlation Spectroscopy
ISC	Intersystem Crossing
LEPR	Light-induced EPR
ODCB	ortho-dichlorobenzene
PCE	Power Conversion Efficiency
REC	Recombination
rGO	Reduced Graphene Oxide
SCRP	Spin-Correlated Radical Pair
S/N	Signal-to-noise ratio
TREPR	Time-Resolved EPR
ZFS	Zero-Field Splitting

Publications and Conference contributions

Papers

- '*Probing photoinduced electron-transfer in graphene-dye hybrid materials for DSSC*'
  Paola Guarracino, Teresa Gatti, Nicolò Canever, Mustapha Abdu-Aguye, Maria Antonietta Loi, Enzo Menna, Lorenzo Franco *PCCP*, **2017**, 19, 27716-27724.

- '*Peptide-driven charge transfer organogels built from synergetic hydrogen bonding and pyrene-naphthalenediimide donor-acceptor interactions*'
  Silvia Bartocci, José Augusto Berrocal, Paola Guarracino, Maxime Grillaud, Lorenzo Franco, Miriam Mba *Chem. Eur. J.*, **2018**, 24, 2920-2928.

Conference contributions

- '*Triplet states and paramagnetic defects as probes of molecular orientation in polymer films studied by EPR*'
  The International Conference on Hybrid and Organic Photovoltaics - HOPV16, Swansea, UK (2016)
  The 10th Conference of the European Federation of EPR groups - EFEPR, Torino (2016)
- '*CW-EPR, TR-EPR and HYSCORE investigation of peptide-functionalized supramolecular donor-acceptor gels* '
  The 50th Annual International Meeting of the ESR Spectroscopy Group of the Royal Society of Chemistry, Oxford, UK (2017)
- '*EPR spectroscopy for the investigation of photophysical and morphological properties of polymeric thin films*'
  European Magnetic Resonance Meeting - EUROMAR 2018, Nantes, FR (2018)